Computer Simulations of Y_2O_3 Nanoclusters: the Impact Nanoclusters have on the Irradiation Resistance and the Strength of Oxide Dispersion-Strengthened Steels

by

Michael P. Higgins

A dissertation submitted in partial fulfillment
of the requirements for the degree of
Doctor of Philosophy
(Nuclear Engineering and Radiological Sciences)
in The University of Michigan
2019

Doctoral Committee:
  Professor Fei Gao, Chair
  Dr. Ram Devanathan, Pacific Northwest National Laboratory
  Assistant Professor Liang Qi
  Professor Lumin Wang

Michael P. Higgins

mphigs@umich.edu

ORCID iD: 0000-0003-4056-7637

Dedications

This thesis is dedicated to my dog Benji, may his pants stay fancy and to my mom, Suzan. Thank you Benji for the cuddles, and thank you to my mom for all the support throughout my life.

Acknowledgements

My advisor, Dr. Fei Gao, deserves considerable appreciation for the numerous hours of guidance, support, and available nodes on the flux that made it possible to complete this work. The experience I have gained as a member of his research group has helped shape the scientist that I am today, and will help push me to bigger and greater things in the future. I would also like to thank the members of my dissertation committee, Dr. Lumin Wang, Dr. Liang Qi, and Dr. Ram Devanathan for their assistance and insight.

I would like to thank my friend Sebastien, The Ph.D. process has been filled with many highs and lows and I want to thank him for always being there for hour long conversations on the phone. If it wasn't for you I wouldn't be here today defending my thesis.

I would also like to thank my fellow compatriots in the Dr. Gao research group for their helpful encouragement, assistance, and discussion through the many years that I have spent at the University of Michigan: Nanjun Chen, Dr. Qing Peng, and Dr. Alexander Barashev. I would also like to give thanks to the rest of the nuclear material students at the University of Michigan, I have learned so much from you all and I appreciate all of the conversations on the future of the nuclear industry, to our game nights: Stephen Raiman, Elizabeth Getto, Anthony Monterrosa, Tai Ni Yang, Stephen Taller, Drew Johnson, David Woodley, Gerrit Vancoevering, Rigel Hanbury, Justin Hesterberg, Samara Levine, and Katey Thomas, thank you all for helping me relax and not think about my dissertation 24/7.

I would like to give a special shout out to two individuals for helping me through my Ph.D. process, Dr. Qing Peng and Chaoming Yang. Thanks to Dr. Peng I was able to use many more processors to run my simulations, and he was very helpful in improving my manuscripts for publication. Chaoming Yang, you spend countless hours going over my dislocation research and teaching me the key basics to run these simulations. Without either of you I would not be here today. I am eternally grateful to you two.

Support for this project was provided by funding from the Nuclear Energy University Programs (project number DE-NE0008297). This research was supported in part through computational resources and services provided by Advanced Research Computing at the University of Michigan, Ann Arbor.

Table of Contents

List of Tables

List of Figures

Abstract

Next generation reactors are going to push structural materials to higher temperatures and displacements per atom; in order to combat these conditions, structural materials need to be designed to withstand these extreme operating conditions. One of the proposed materials, for new reactor types is oxide-dispersion strengthened (ODS) steel. ODS steel is a proposed structural material due to its high strength, and high irradiation resistance. ODS steel gains the increased strength from the introduction of Y-O based nanoclusters (NCs) to the bcc iron matrix. The improved properties of ODS steels make them a favored structural material for next generation reactors; however, much still needs to be fundamentally understood, before ODS steels can be used in these reactor designs.

Molecular dynamics (MD) is used to model ODS steels, to better understand the fundamental effect NCs have on the irradiation resistance and base strength of these alloys. MD is used to understand the structure of NCs within the matrix; via MD simulations, the NCs form a core-shell structure. The core-shell structure consists of Y_2O_3 cubic structure and a shell of disordered atoms.

The primary damage state of a cascade near and within the NC is investigated with MD. Three temperatures for the cascade are investigated: 100 K, 300 K, and 600 K. In the three cases the results are very similar. In the Fe matrix, a net decrease of interstitials is seen within the iron matrix with the NC acting as a site for interstitials to migrate to during the primary damage state of a cascade. Along with decreasing the number of point defects in the Fe matrix, the NC begins to form a sink structure during the relaxing process of the cascade. The incoherent boundary, between the iron matrix and the NC, causes the formation of the sink during the cascade simulation. Within the NC, the structure of the NC is lost during a cascade, as the NC becomes entirely amorphous, and loses the core-shell structure. The results of the primary damage state of the cascade showed that ballistic dissolution plays a key role in the short term development of a NC in an irradiation environment.

Dislocation interactions with NCs play a key role in the improved strength of ODS steels. Edge and screw dislocations are simulated with MD and the depinning mechanism is investigated for NCs. In the case of edge dislocations, NCs are able to break away from the NC via a combination of the Orowan and climbing mechanism. In the case of the edge dislocation the obstacle strength is independent of NC radii at higher temperatures. In the case of the screw dislocation, the screw frees itself only by the Orowan mechanism and in the process, creates a dislocation loop along the NC. Screw dislocations tended to be more encumbered by the NC, having a higher obstacle strength that is independent of temperature. The obstacle strength of the NC is independent of NC radii for the edge dislocation.

The two key studies, the primary damage state and dislocation interaction, of NCs as part of this dissertation show that a critical size exists for NCs such that the NCs are able to maintain a high level of irradiation resistance, while also pinning dislocations, and hence increasing the strength of the base Fe matrix.

Chapter 1 - Introduction

Nuclear energy is a major electricity contributor in the United States, accounting for roughly 19% (807 TWh in 2017) of United States domestic electricity[1]. Currently the nuclear fleet is entirely based on technology from the 1950s, light water reactors (LWRs)[1]. Nuclear power in general has many benefits compared to the other standard large-scale electricity contributors: a high density of energy production, safety, and carbon-free emissions. The last reactor that started construction and finished was in the 1970s. Over time LWRs have been shutting down and the nation is at a point where the power generation from nuclear is going to diminish without new plants being built[1]. A new generation of fission reactors and fusion reactors are being designed to provide a source of high density, zero-carbon emission energy[2,3].

The goal of new reactors is to provide a continued source of clean electricity with additional safeguards, such as naturally safer designs; new reactors are also required to have lowered costs. A major aspect of next generation reactors is the increased temperatures and increased amount of displacements per atom (dpa) facing structural materials compared to generation II and generation III reactors. Figure 1.1 shows the temperature and dpa ranges for current LWRs and future reactors, generation IV fission reactors and fusion reactors[4]. From figure 1.1, it is obvious that next generation reactors are going to require a brand new class of structural materials to withstand these higher temperatures and irradiation conditions.

A major area of research into structural materials for next generation reactors has shown a few key characteristics in next generation materials. The first is the benefits of switching to a BCC base steel compared to FCC[5,6]. As BCC materials have shown to have considerably less swelling compared to FCC steels[7]. Two major types of bcc materials have been the key area of focus for next generation reactors reduced activation ferritic/martensitic (RAFM) steels and Oxide Dispersion Strengthened (ODS) steels[8–10]. RAFM steels gain their strength by starting with a very pure base alloy and then during heat treatments and consolidations creating a base metal with a high number density of precipitates, which creates a base material with lots of surfaces for the trapping of defects. RAFM steels end result is a material that has good properties, increased strength and radiation resistance due to the inclusion of precipitate structures and may be used in next generation reactors.

ODS steel is a step further in materials development, and such a much newer technology[8]. Although the manufacturing techniques for ODS steel were first patented in the 1970s, the material became a major area of nuclear research during the late 1990s, when the fine tuning of a base alloy with YO powders started to really take off[11]. Through improvements to the ball milling technique and fine tuning of the following consolidation technique and heat treatments, ODS steels have been shown to also be a very strong material, stronger than the base F/M steel in many ways[11,12].

Although at this point ODS technology is still very much in the ground state as this technology is very new compared to RAFM steels, and such there are still quite a few unanswered questions about this material.

The key benefit of the ODS steel compared to RAFM steels is the introduction of the large nanoclusters (NCs) population via the ODS steel manufacturing steps. However, one of the major concerns of ODS steel for nuclear reactor conditions and one of the focuses of this study is on how irradiation affects the NC population. Many experimental studies have looked at the evolution of NCs during irradiation; by examining the change in average radius, number density, and fraction of bulk material NCs take up. However, a recent review compiling all of the ODS steel ion irradiations showed confounding results, which stated that many of these studies have shown conflicting trends within the ODS steels[13]. These conflicting results are shown to be caused by slight changes in material composition and irradiation conditions[13]. The use of computer simulations may play a key role in furthering the understanding of how irradiation affects the NCs and the surrounding bulk material.

A focus of the dissertation aims at furthering the understanding of two key aspects of how NCs effect ODS steel. The first is looking at the effect NCs have on the evolution of point defects during a cascade. Many studies have looked into the effects of a pure metal system[14–16]. However, few studies have looked into the effects precipitates have on the evolution of damage within the matrix and precipitate. Another key area that the NCs have on the base material is increasing the base strength of the material. As the NCs act as pinning locations for dislocations, the base material's strength is improved with the inclusion of NCs. Studies have shown that the base material is strengthened due to NCs, but the key mechanism behind NC pinning and depinning is not understood.

This dissertation utilizes molecular dynamics (MD) to further the understanding of how the primary damage state of a cascade is affected by the introduction of a NC. By using large-scale atomic/molecular massively parallel simulator (LAMMPS) a cascade is simulated near the shell of a NC and the evolution of damage is tracked within the system[17]. Ovito is a very useful tool in visualizing and analyzing the results of MD results[18]. Ovito combined with python is used to track and monitor the evolution of damage during the primary damage state of a cascade. The effects of temperature and NC diameter are investigated and the effects on the cascade at a NC boundary are compared. MD is also utilized in modelling the effects NCs have on the mobility of screw and edge dislocations. Screw and edge dislocations are introduced into a pure Fe matrix. A shear stress is applied and the dislocations are forced to interact with the NCs. The shear stress required to overcome the NCs along with the mechanisms to pass through the NC are investigated. The mobility of the dislocation is then inputted into a dislocation dynamics code, ParaDis, to understand the strength NCs have on the base material[19].

This dissertation is broken into the following chapters. Chapter 2 looks at key background information in the evolution of irradiation damage, with a focus on simulating the primary damage state of a cascade and edge and screw dislocation movement in a metal matrix. Chapter 3 looks at the structure of a NC based on diameter. Chapter 4 presents the effects a cascade has on the evolution of damage within the primary damage state of a material. Chapter 5 looks at the effects NCs have on the mobility of edge and screw dislocations. Chapter 6 combines the results from Chapters 3 – 5 and discusses the key results on how NCs affect the evolution of the surrounding bulk material and NC, and how a NC affects the strength of a material based on dislocation pinning. Chapter 7 gives the key conclusions of this dissertation and chapter 8 provides some interesting ideas for the continuation of these simulations to further the understanding of the implication of NCs within ODS steels.

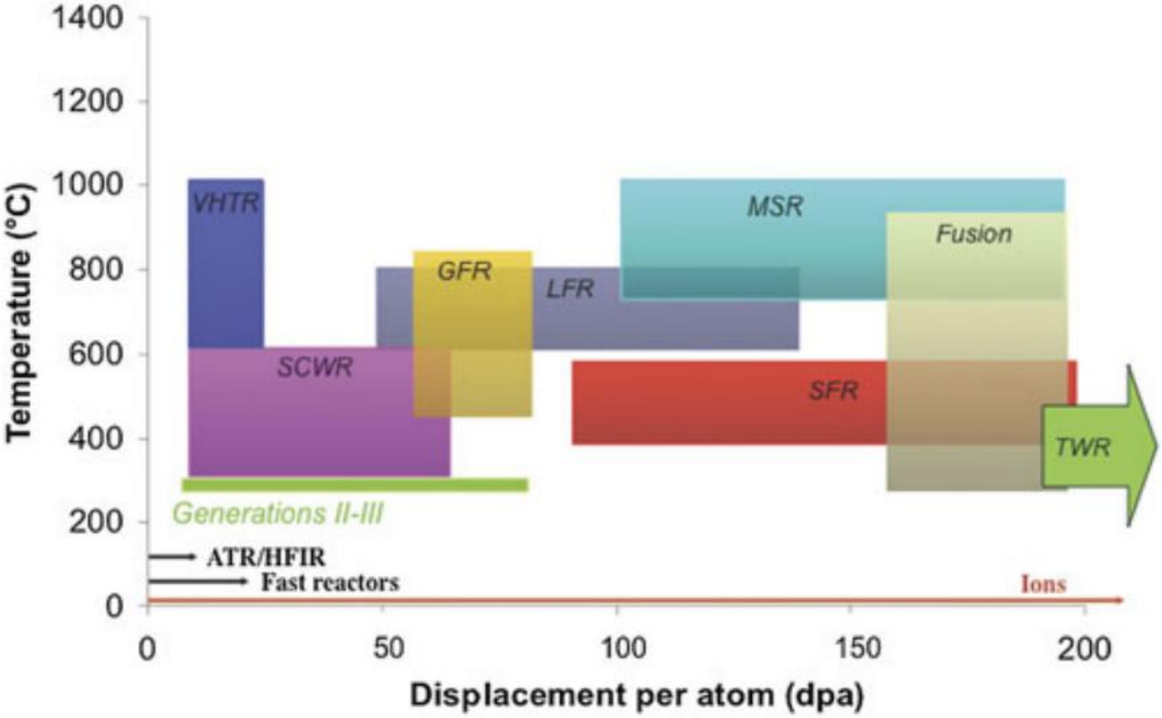

Figure 1.1. The theorized dependence for displacements per atom (dpa) and temperatures are shown for current reactors (Gen II-III), next generation fission reactors(VHTR: Very High Temperature Reactor, SCWR: Super Critical Water Reactor, GFR: Gas Cooled Fast Reactor, LFR: Lead-Cooled Fast Reactor, SFR: Sodium-Cooled Fast Reactor, MSR: Molten Salt Reactor, and TWR: Travelling Wave Reactor), and fusion reactors[4].

Chapter 2 - Background

Oxide dispersion strengthened (ODS) steels are being proposed as a potential structural material in next generation fission and fusion reactors[11,20]. However, as these materials are a relatively new technology they have many unanswered questions that are paramount to their implementation in these reactor designs. One of the key questions and the focus of this dissertation is on ODS steel's ability to mitigate radiation damage. The goal of this dissertation is to further the understanding of how nanoclusters (NCs) impact the overall strength of ODS steels. The background section is broken into two major sections.

First, having a background on how radiation damage interacts with a material on a fundamental level is a prerequisite in understanding the impact ODS steels have in a radiation environment. The first section is going to cover the theory and key simulation studies behind the evolution of radiation damage in materials. Figure 2.1 shows the evolution of radiation damage. All radiation damage starts with the creation of Frenkel pairs during a displacement cascade on the picosecond timescale and nanometer length scale. From there, defects start to form clusters and over much larger time scales and length scales, these tiny interstitial and vacancy clusters start to form precipitates, bubbles, and dislocations that negatively affect the material’s properties. Along with explaining the key theories behind radiation damage evolution, key simulation techniques that are pertinent to this dissertation are highlighted and explanation of techniques and results are analyzed.

The second part of this background section looks at the material properties and key simulations ran for ODS steel. The second section looks at experimental results for both ferritic-martensitic (F/M) and ODS steels. By comparing the advantages and disadvantages of F/M and ODS steels, the two prominent materials for next generation reactors. The niche ODS steels fits in a nuclear world is further understood. The evolution in ODS steel’s development and research on the evolution of nanoclusters (NCs) during irradiation is a primary focus. As NCs are the factor that differentiates ODS steels and F/M steels. These NCs need to be better understood to further the understanding of ODS steels ability to resist irradiation damage.

2.1 Point Defect Production

The evolution of all damage within a metal alloy is due to the scattering of neutrons from the reactor core out to the structural materials. Figure 2.2 shows all the steps for irradiation to cause damage within structural materials. These neutrons are created via neutron scattering and nuclear reaction events and can have energies up to 100s of kilo-electron-volts[21]. These primary recoiling atoms (PRAs) disperse their energy throughout the material and each PRA ends with a cascade[22,23]. These displacement cascades evolve similar to a shockwave. Figure 2.2a shows a standard point defect shockwave. Every shockwave independent of PRA energy primarily consists of two things; a core of vacancies, which is surrounded by a population of interstitials. An interstitial can be broadly defined as an atom no longer on its own lattice site, the most energy efficient position. This usually consists of atoms being knocked off its lattice site on to non-ideal sites within the matrix. In the standard case these atoms may be on tetrahedral or octahedral sites within the lattice. Along with being on those interstitial sites, in more complex metal alloys and systems, the displaced atoms may knock different atom species off their lattice sites and during the cascade relaxation process, atoms may find their new energy preferred location to be on a different atom's lattice site; this type of interstitial is considered to be as antisite. Vacancies are lattice sites that are empty.

After the shockwave forms within the material matrix, the shockwave will quickly implode on itself, with the interstitial shelling migrating to the core vacancy region, filling in many of the vacancies within the core. Depending on PRA energy, the shockwave can occur as low as 10^{-13} s to 10^{-12} s, with the shockwave occurring later with increasing PRA energy. The imploding of the cascade occurs over several picoseconds, with a stable number of surviving Frenkel pairs at the end of each cascade. Since cascades occur over such tiny timescale, computer simulations have played a major factor in understanding and shaping this aspect of irradiation damage.

2.1.1 Computer Simulation of Point Defect Cascades

Molecular dynamics (MD) simulations of cascades have greatly helped in understanding the primary damage state of the cascade. In the late 1990s, there was a major breakthrough in understanding the primary damage state of a cascade using MD[14,23,24]. MD has been used to simulate primary knock-on atoms (PKAs), and tracking how the energy of the PKA is transferred through the metal system. The first major observation was that a cascade exhibits two major phases, shown in Figure 2.3. The first phase is called the ballistic phase. The ballistic phase is on a very small time scale, for just a few tenths of a picosecond, but with increasing PKA energy, the ballistic phase can increase to up to ~ 2 ps for a 100 keV PKA. The ballistic phase, as it sounds, is based on a high amount of ballistic collisions between the atoms within a very tiny region. This creates a liquid-like core, with a crystalline region displaced outwards[25].

Following the ballistic phase is the thermal-spike phase. The thermal-spike phase is defined as the point where the kinetic and potential components of the crystal reach equilibrium. This period consists of heavy amounts of recombination, and the remaining atoms that are unable to regain lattice sites create a final defect state. A key evolution in cascade simulations was the development of embedded atom model (EAM) potentials. EAM potentials greatly improved the ability for potentials to model radiation damage, via more accurately measuring the migration and formation energy of defects[25–27].

A very common method for evaluating the number of Frenkel pairs predicted using MD to those used in experimental calculations is via a formula developed by

Norgett, Robinson, and Torrens (NRT). The NRT model had been adopted as the standard for estimating the dpa in irradiated materials[15,23].

$$N_{NRT} = \frac{0.8E_{PKA}}{2\overline{E_d}} \qquad \text{Eq. 2.1}$$

Where N_{NRT} is the number of Frenkel pairs as a function of the energy of the incoming particles and E_d, the average displacement energy of the material. The NRT model is based on the binary collision approximation and thus does not explain how atoms react in reality. Along with using assumptions to gauge the number of defects, the NRT model is unable to estimate the spatial and clustering aspects of a cascade. Figure 2.4 shows the ratio of Frenkel pairs, obtained for a pure bcc Fe matrix at various PKA energies, to the number of Frenkel pairs predicted by the NRT model at that energy. This shows that the number of Frenkel pairs at the end of an MD simulation is considerable less compared to the NRT model. MD results for number of Frenkel pairs for various materials and PKA energies have been fitted to the power equation.

$$N_{FP} = A(E_{PKA})^m \qquad \text{Eq. 2.2}$$

Where A and m are variables for fitting. As shown in Figure 2.5 the number of Frenkel pairs is shown to have power-law dependence. Again shown up to high PKA energy, the amount of Frenkel pairs suggested by MD is significantly decreased compared to the NRT model. This reduction is believed to be based on the structure of the shockwave, with an inner region of vacancies and the outer region of interstitials. As the interstitials are directly near the vacancies immediately after the shockwave, the interstitials are able to quickly recombine with the nearby vacancies[14]. Experimental data has also corroborated that the number of defects produced in pure metals or alloys during an ion or neutron irradiation was approximately one quarter of the NRT value[28,29].

A key benefit of MD over the standard approximations used is the ability to see how the interstitials and vacancies evolve over the course of the cascade. Interstitials have been shown to preferentially form into clusters almost immediately after/during the shockwave of a cascade. Vacancies on the other hand are shown to be very unstable in clusters, with most vacancies occurring as single defects. The difference in clustering between interstitials and vacancies is due to the stability of the point defects; interstitials have been shown to have much lower migration energies allowing these defects to migrate away from the cascade area and form clusters with other interstitials. In some cases it is possible for the migration of interstitials to interact with nearby structures; such as, grain boundaries or dislocations during the primary cascade timescale[30–32]. Figure 2.6 shows the clustering for vacancies and interstitials at 100 K for HCP Zr and BCC Fe for several PKA energies. These plots show that interstitials are more likely to form clusters and at high energies it is possible for these clusters to become very large [14,23,24].

2.1.2 Spatial Distribution of a Cascade

There are two mechanisms that control the formation of interstitial clustering. The first is during the transition from collision to thermal-spike phase. The second mechanism that controls the growth of interstitial clusters is during the thermal spike by short-range diffusion. Clustering formation occurs when the shockwave displaces the atoms outwards from the center of the cascade. The clusters that are formed within this process are unable to escape; the relatively longer term clustering is a result of the reorganization driven by the large elastic interactions between neighboring interstitials. The probability and size of the largest clusters tend to increase with increasing PKA energy. Another effect of the larger and increased number of interstitial clusters is an increase in the number of vacancies clusters formed by the clustering of the interstitials. In comparing the BCC and HCP structures for clustering in Figure 2.6, the structure of the material is shown to have some effect on the number of vacancy and interstitial clusters[14].

Along with the size of the clusters, the fraction of interstitials that are clustered versus single interstitials is very important. Once a critical energy is passed, where the system goes from a single displacement to true cascade phenomena, the fraction is metal dependent. It has been shown that the structure of the metal plays a key role in the formation of clusters. With the key controlling factor being the type of metal matrix, which controls the fraction of clustered to single interstitials, being the ability for the interstitials to reorient within the metal matrix and migrate easily during the thermal spike.

2.1.3 Temperature Dependence of a Cascade

Prior to this section, all of the cascade calculations have been done at relatively low temperatures, 10K-100K. Since reactor conditions will occur at much higher temperatures, a look at the temperature dependence of a cascade is paramount to using MD results for understanding the evolution of damage within a material matrix for the primary damage state of a cascade for reactor conditions. Gao looked at low energy cascades, 2 and 5 keV, at various temperatures from 100 K to 900 K to see the effect temperature had on the primary damage state of the cascade[33]. The theoretical definition of temperature defines temperature as a measure of the kinetic energy of the atoms. Within a cascade, specifically the thermal peak period, the temperature of the system can easily increase by a huge margin; with the temperature in the system significantly increasing based on the PKA energy. Due to the increased temperature of the system, interstitials, which have relatively low migration energy, have a higher potential to migrate, whereas vacancies which have significantly higher migration energy are less affected with an increased thermal peak.

A major factor of temperature is the amount of time required to bring the matrix back to the equilibrium temperature of the simulation. With increasing temperature the period of time in which the thermal peak occurs increases. Figure 2.7 shows the effect temperature has on a 20 keV cascade in a Fe matrix, with temperatures ranging from 100 K to 1000 K. This factor, an increased thermal peak with increasing temperature has two major effects in the metal matrix. First, Figure 2.7 shows that at higher energies the number of Frenkel pairs at the peak time is significantly higher. The increase in the number of Frenkel pairs at the peak damage state is an effect of the atoms having significantly lower migration energies at higher temperatures, causing the cascade shockwave volume to significantly increase with increasing temperature. Second, the increased volume causes the amount of time required for the system to disperse the kinetic energy to the equilibrium Frenkel pair damage state increases. This migration period causes two major things to happen in the metal matrix: the first is that there is a slight drop in the number of Frenkel pairs at the end of the primary damage state of the cascade and second, the interstitials that do survive the cascade are more likely to be in clusters at the end of the cascade[15].

2.1.4 Key Aspects of a Point Defect Cascade in BCC Fe

The key matrix for ODS steels for next generation fission and fusion materials has tended to prefer a Fe BCC base alloy, given this structure’s ability to withstand irradiation damage. So understanding the evolution of defects within a standard BCC Fe matrix is imperative to understanding how ODS steels improves on the standard Fe based alloys. Table 2.1 shows some of the standard sizes and PKA energy used in Fe cascade simulations. In evaluating Fe damage some of the common trends at various energies will be discussed starting at lower energies and moving to higher energies.

The direction of the PKA, with respect to the Fe matrix, is very important. A study by Sahi looked at reviewing the effects of PKA energy, and temperature on α-Fe[15]. Table 2.2 shows the number of surviving Frenkel pairs as a function of direction, energy, and temperature. In this table it is shown that in comparing all the potential directions the largest amount of defects showed up along the [112] lattice direction and the lowest number of surviving Frenkel pairs was along the [110] direction. This difference in Frenkel pair evolution is due to the BCC lattice structure. As the [112] plane acts as the principle slip plane in the BCC structure and the [110] plane is the most compact and stable plane in the BCC structure. The other directions investigated included the [111] and the [135] directions. As the [135] is the high-index direction and the [111] direction is the closed pack direction. In comparing the number of Frenkel pairs in each simulated direction, the [111], [135], and [112] planes were fairly equal, with the [110] direction having significantly less Frenkel pairs compared to the three directions.

All large, evolved microstructures formed in structural materials start from these primary cascades. From a cascade the damage forms clusters, understanding the formation of clusters within the Fe matrix is an imperative first step as these clusters form the nuclei for all future microstructural changes. Figure 2.8 shows the clustering fraction for interstitials and vacancies as a function of PKA energy and temperature. For interstitial clustering the fraction of clustering increases much faster compared to vacancies up to 20 keV and then slowing at higher energies. The reason for the slowing, in fraction of interstitials, at higher energies is that at higher energies the cascade breaks down into many smaller cascades and the effect of increased PKA energy is no longer attributed to the energy of the PKA but more so the volume of the primary damage state of the cascade. The dependence on the vacancy clustering with energy is significantly lower compared to interstitials, showing a very small linear growth with increasing PKA energy. These clusters are the precursors to microstructural evolution in materials.

2.1.5 Key Aspects of a Point Defect Cascade in BCC Fe

A key area of growth in recent years has been the relationship between the primary damage cascade and different defect or crystal structures in a material. A major area of development has been of simulating displacement cascades at grain boundaries. Prior to cascade simulations understanding the formation of energy as a function of a defect is very important. A study looked at the formation energy of interstitials and vacancies at and near grain boundaries. The grain boundary is investigated for 50 (110) symmetric tilt grain boundaries in bcc Fe to assess the grain boundary strength. In comparing the stability of the grain boundaries, the low angle grain boundaries tended to have favorable structures[34].

All atoms within 20 Å of the grain boundary are characterized and that equation to calculate the formation energy of a defect is shown as:

$$E_f^v = E_{GB}^v - E_{GB} + E_{coh} \qquad \text{Eq. 2.3}$$

The terms in equation 2.3 are E_f^v stands for the formation energy of the site, E_{GB}^s and E_{GB} are the total energy of the system with and without a vacancy and E_{coh} is the cohesive energy/atom of a perfect bcc lattice. For an interstitial the only thing different in equation 2.3 is that the coherency energy term is subtracted instead of added. This is to reflect the added energy due to the placing of an atom on an interstitial site. Figure 2.9 shows the structure of the grain boundaries in bcc Fe and the formation energy for vacancies and interstitials in the grain boundary[34].

The grain boundary shows several sites that are lower in formation energy compared to the bulk. The lower formation energy suggests that the vacancies would be attracted to the grain boundary sites. In the case of the interstitials within the grain boundary, most of the grain boundary sites are lower in formation energy than the bulk. A majority of the formation energy of the interstitials and vacancies start to change from the bulk within 5-8 Å of the grain boundary. In comparing the vacancy and interstitial formation energies to grain boundary angle, the high angle boundaries tended to have significantly lower interstitial formation energy, with the low angle boundaries being more similar to formation energies near a single dislocation. The binding energy for vacancies and interstitials at grain boundary sites show that grain boundaries heavily prefer interstitials compared to vacancies[34].

A few studies have looked at the effect a primary displacement cascade has had on the grain boundary and the nearby Fe matrix[30,35,36]. Low PKA energy (< 10 keV) are the main focus of published research so far. In looking at a pure Fe system, the focus has been on different misorientation angled grain boundaries and the effect of defect accumulation. Figure 2.10 shows the evolution of a 6 keV PKA near a low angle and high angle grain boundary. The low angle boundary has fewer defects compared to the high angle boundary. Both studies looking at pure Fe grain boundary interactions with a PKA both corroborated this result[35,36]. The results in these studies did not corroborate the early report on formation energy of defects near grain boundaries. This shows that formation energy alone does not tell the whole story. Although the formation energy of high angle boundaries is lower, the low angle grain boundaries are able to significantly decrease the number of defects at the grain boundary.

Along with grain boundaries, precipitates are another important feature in materials that needs to be better understood. Currently there are not that many studies on the effects the primary cascade has on precipitates, especially for bcc Fe; some hcp and fcc studies are added to tell a better picture of the effects of cascade on precipitates[32,37,38]. Each of these studies looks at very different structures: embedded NCs, nanovoids, and an amorphous film. A look at these three studies shows the similarities and differences these structure types have on the evolution of the primary damage state.

As all of these studies are new concepts, a significant amount of time has been spent looking at low energy PKAs. The nanovoids study looked at the effect of the number of nanovoids have on the evolution of damage up to PKA energies of 9 keV. In this study on defects with voids, independent of the number of voids and PKA energy, the inclusion of a surface causes a drop in the number of interstitials within the bulk system. Along with a drop in the defects in the bulk system, the surfaces of the voids form vacancy clusters followed by a layer of adatoms. Adatoms are the opposite of vacancies and can occur at free surfaces forming at the surface. Voids significantly dropped the number of vacancies in the bulk of the system, a unique feature compared to precipitates during the primary damage state[38].

Another study looked at the effect of precipitates in a hcp Zr matrix. The precipitate consisted of a randomly seed 20% Zr-Nb bcc cluster. A 10 keV PKA is placed 10 Å away from the outer shell of the NC. The evolution of the damage in this precipitate showed the Nb entering the nearby hcp Zr matrix as interstitials in the hcp structure. This study primarily showed that the introduction of a displacement cascade effected the precipitate growth and change in composition. Showing the importance of further study into the effect displacement cascades have on precipitate development[32].

In this subsection the brief history of displacement cascades has been covered. With displacement cascades start in modelling the effect in a pure metal system and then moving to more complex structures in modern history. The effects a displacement cascade has on a material from MD vastly differed from the believed models. Along with predicting a much smaller number of Frenkel pairs in the bulk system, MD has shown how clusters form directly after a shockwave. With improvements made in interatomic potentials along with the understanding of how the bulk material is affected by a displacement cascade, the more recent research has looked into the effect of a primary displacement cascade on structures common to materials. This is the area that needs the most improvement, along with going to more temperature and different temperatures; this is the area that has the most unanswered questions in cascade simulations.

2.2 Long Term Diffusion of Point Defects/Clusters

From the creation of point defects and point clusters, which occur on the ps time scale, these defects and clusters have the ability to evolve over much longer timescales. Figure 2.1b-e show some of the potential long term effects for point defects in materials. The first case is long term recombination of point defects. Point defects can recombine following two major mechanisms. The first mechanism is over longer periods of time single point defects may migrate together and recombine. The second mechanism is based on defects recombining at trap locations. A few of the common trap locations in a metal matrix are grain boundary interfaces, cavities, voids, dislocations, and incoherent precipitates.

The individual strengths of sinks are based on solutions to the diffusion equation [add source] For example, for spherical sinks (cavities and incoherent precipitates) the strength of the sink is approximated as $4\pi r_s N_s$, where r_s is the radius of the sink and N_s is the number density. From the sink strength of spherical defects it can be derived that the strength of spherical sinks increases with decreasing radii, as it was derived that the

Z_s is approximately as $3f_s/r_s^2$, where Z_s is the strength of spherical sinks and f_s is the volume fraction of said sinks. Along with spherical sinks another common sink is dislocations. For dislocations the sink strength has been approximated as the density of the dislocations. However, dislocations as sinks are slightly more complicated compared to spherical sinks. As the introduction of a dislocation into the matrix of a material introduces a strain field surrounding the dislocation, which causes the dislocation to have a bias for defects. This bias is dependent on the type of dislocation and the orientation within the matrix.

Assuming a quasi-steady state situation, there exists a condition where the rate of recombination with annihilation versus accumulation at sinks will be balanced to the primary defect generation rate, for metal conditions where the Temperature is less than half of the melting temperature. With these conditions the irradiation-induced vacancy flux consists of the concentration of vacancies minus the loss of vacancies to both interstitials and sinks. The vacancy flux tends to be greater than zero as dislocations have a bias for interstitials. The bias between interstitials and vacancies at sinks plays a key role in the evolution of long term effects in microstructures.

When there is a net gain of vacancies within the system, the vacancies will coalesce together and form voids (figure 2.1e). Radiation-enhanced diffusion (RED) and radiation-enhanced precipitation (REP) occurs as well. The radiation also causes radiation-induced solute segregation (RIS) and radiation-induced precipitation (RIP) of solute-enriched regions that are able to cross phase boundaries (figure 2.1g). The dislocation bias for interstitials causes the formation of growing interstitial dislocation loops, dislocation climb, and an overall evolution in the dislocation structure (figure 2.1c). Loop formation is a key factor in any irradiation condition, and are unaffected by other irradiation effects such as swelling. Understanding the impact dislocations have in the strength of the material, along with dislocations interaction with radiation defects is an imperative step and has been heavily modelled using MD.

2.3 Computational Modelling of Dislocations

After the primary damage state of a cascade, a small amount of Frenkel pairs are added to the metal system. The evolution of the primary damage state summarized in section 2.2 showed one key aspect of the Frenkel pairs at the end of the primary damage state. The key aspect is that that the interstitials are significantly more likely to form in to clusters compared to vacancies. These interstitial clusters created during the primary damage state, on longer timescales, will coalesce becoming larger and larger clusters i.e. (dislocations, stacking fault tetrahedra (SFT), and voids). A key aspect of understanding the movement of defect clusters is correctly modelling the fraction of glissile and sessile clusters of SIAs, along with their stability and mobility.

In α-Fe the most stable configuration for clusters is a set of <111> crowdions. For tiny clusters between 2-10 interstitials, the most stable configuration has been shown to be crowdions along the {110} plane. However, for very small clusters <4 interstitials it has been shown that <110> dumbbells in a {110} plane are also stable. As the cluster grew to a size of 5-7 interstitials, the cluster transforms from a <110> dumbbell to the <111> crowdion via a rotation of the habit plane. From there the cluster is stable, but at a cutoff of 16 interstitials the cluster would then transform into a (1/2) <111> {111} edge dislocation loop. The stability of clusters has been shown to be highly effected based on the MD techniques used in modelling these structures. A key aspect of bcc clusters is that the all of the clusters are glissile because of the behavior of their relationship to the burgers vector[39].

In the case of a fcc material such as copper. The tiniest cluster that is stable is is two <110> dumbbells. However, with larger sizes there are two stable clusters: the first is a set of <100> dumbbells and the second is <110> crowdions. Both of these clusters are along the {111} habit planes. As these clusters grow they form two larger structures. The <100> clusters transform into Frank faulted loops (1/3) <111> {111} and the <110> crowdions transform into perfect loops (1/2) <110> {110}. The stability of both loops is similar with the perfect loop and the crowdions having a slight preference at larger sizes. The structure of these clusters is also affected by the shape as certain shapes will form perfect edge dislocations, whereas certain shapes will form dislocations they will dissociate on their glide prism into Shockley partial dislocations. So a major difference of FCC compared to BCC is that in the case of FCC the material has both a glissile cluster of <110> crowdions forming perfect loops and sessile clusters <100> forming faulted Frank loops[39].

In comparing the glissile properties of interstitial clusters in both structure types, the results are very similar. The tiny clusters (less than 4 interstitials) move in three dimensions, with temperature increasing the change in motion. For the larger clusters the movement is very temperature dependent and the larger cluster are only able to move along one direction. However, as the clusters form into loops there becomes a noticeable difference between the <111> {111} edge dislocation in the bcc materials and the <110> {110} perfect loop in the fcc structure. As loops grow in the fcc structure, over 100 interstitials caused the loops to become immobile. However in the bcc structure, there is no mechanism that prevents the thermally activated one-dimensional transport of isolated loops. This major difference is a factor in the lower concentration of clusters within the Fe matrix compared to Cu, as the clusters are more mobile they are more likely to be absorbed at sinks such as dislocations and grain boundaries[39].

2.3.1 Edge Dislocations in BCC Structure

There are two major types of edge dislocations in the BCC structure. In BCC Fe, slip is shown to occur on mainly the {110} and the {112} planes[40,41]. Activation on either of the planes is based on a few properties: the loading direction, critical glide stress, and the kink formation energy in each of the planes. In the past, it has been assumed that all edge dislocations in the bcc system were of the type ½ <111> {110} as their motion is fast and nuclear of kinks is athermal. This is the case for quite a few different BCC metals[42–44]. However in the early 2010s it was shown that the mobility of ½ <111> {112} edges in bcc Fe require a nonzero critical stress to move and the motion is based on a double-kink formation. This section will review some of the major differences in motion of the {110} and {112} plane edge dislocation.

In setting up a dislocation in MD, Osetsky created a standard set up that consisted of the following rules[44]

1. Reproduction of the correct configuration of the dislocation core structure and quantitative description of the properties
2. The possibility of moving a dislocation over long distance under applied stress or strain
3. Independent application and quantification of important external effects such as applied stress or strain, and calculation of the resultant response
4. A simple procedure for analyzing dislocation motion and dislocation-obstacle interactions
5. A relatively fast computing speed
6. Simulation at either zero or non-zero temperature
7. The possibility of simulation a realistic dislocation density and spacing between obstacles

A standard unrelaxed setup for an edge dislocation in the bcc structure is shown in figure 2.11. A standard edge dislocation is set up such that the direction of motion (the Burgers vector) and the plane on which the dislocation sits have periodic boundary conditions, whereas the y direction in figure 2.11 case would be fixed. In figure 2.11 the half planes along the y-z are set to have two different lattice constants and via relaxation a perfect edge dislocation is setup in the center of the system.

2.3.2 ½ <111> {110} Edge Dislocation

The ½ <111> {110} consists of six nonequivalent (112) planes which are perpendicular to the edge dislocation line. In an investigation in how this edge dislocation moves, the center of the edge dislocation is moved the distance of the two nearest Peierls valley, $\frac{\sqrt{3}}{2}a_o$, where a_o is the lattice constant of the material. The system is then relaxed and minimized at this distance. The ½ <111> {011} edge dislocation has two kinks. Figure 2.12 shows the potential kinks for both the 1/2 <111> {011} edge dislocation and ½ <111> {112} edge dislocation. The ½ <111> {011} edge dislocation has two possible kink locations. The formation energy of the kink is 0.05 eV with a width of 6.02b, where b is the Burger's vector[45]. The small formation energy for {110} plane edge locations indicates that the mobility of these dislocations is not limited by kinks except at very low temperatures[46].

In a study by Queyreau the effect of stress on the system and temperature were used to calculate the mobility of edge dislocations and the result is shown in figure 2.13. Figure 2.14 suggests that there isn't a threshold stress for the dislocation to move at as it has a velocity at 1 MPa at 100 K. The mobility of the edge dislocation is linear with applied stress and inversely proportional to temperature, which is evidence that phonon drag dynamics play a key role in the movement of {110} edge dislocations. From this study an equation for the mobility of {110} edge dislocations in Fe are obtained and are shown as equation 2.3:

$$v_{\{110\}} = \frac{370.1\tau}{T} \qquad \text{Eq. 2.3}$$

Where τ is the applied stress in MPa and T is the temperature in Kelvin. The key aspects for the {110} edge dislocation is that for the entire range of temperatures the velocity is linear with shear stress applied. The dampening coefficient increases linearly with temperature in agreement with phonon drag theory and no threshold stress is required to initiate dislocation motion.

2.3.3 ½ <111> {112} Edge Dislocation

For the ½ <111> {112}, unlike the ½ <111> {110} the kink formation energy is approximately five times higher, 0.15eV[46]. Due to the significantly higher formation energy, this edge dislocation has a more noticeable kink movement of the dislocation. In running simulations below 300 K, it is possible to observe isolated kinks for simulation times as long as a few nanoseconds[46]. An interesting characteristic of the kink for the ½ <111> {112} edge dislocation is that the formation energy and migration barrier are approximately the same value ~0.15 eV, this suggests that double kink nucleation and kink migration occur on similar timescales.

Double kinks are basically end points of finite portions of dislocation lines that jump across a stiff energy barrier from one equilibrium configuration to the next. The ~0.15 eV formation energy of a {112} edge dislocation is relatively low, this allows the edge dislocation to reach their viscous drag dynamic regime at relatively low stresses and temperatures. Although the {112} edge dislocation has the ability to form a kink, the energy of migration is very low and thus it has very little effect on the dynamics of the dislocation at higher temperatures than 50 K. However, although it has little effect on the dynamics of the dislocation movement, it does affect the threshold energy on either the twinning or twinning direction. The Peierls stress along the twinning direction is 260 ± 10 MPa and the Peierls stress along the antitwinning direction is 520 ± 10 MPa.

The time-displacement curve at 200 K and the velocity at various temperatures for a {112} edge dislocations are shown in figure 2.14. The velocity of the edge dislocation is obtained via extraction from a linear fit of these curves shown in figure 2.14 i.) and plotted on figure 2.14 ii.). Figure 2.14 ii.) shows the velocity of the edge dislocation as a function of temperature (50-300K) and stresses ranging from 1 to 1000 MPa. Unlike the {110} plane edge dislocations, the {112} plane edge dislocations has two distinguished regimes. The first region consists of the dislocation velocity growing exponentially and the second region consists of a more standard linear regime. The transition from exponential to linear dependence on velocity of the edge dislocation decreased with increasing temperature; an indication of a thermally activated mechanism of motion.

The calculations for the mobility of the {112} is broken into the two regions, the first region is for the exponential region. A least-squares fit has been obtained that has a fitting error of approximately 5%:

$$v_{\{112\}} = 1.68 \times 10^4 \frac{\tau_n(T)}{T} exp\{-0.15[1 - \tau_n(T)^{0.13}\}^{0.68} \qquad \text{Eq. 2.4}$$

Where $\tau_n = \tau_a / \tau_d$ where τ_a and τ_d are respectively, the applied stress and the temperature dependent threshold transition stress. Above the exponential region where the velocity has a linear relationship with the stress, the following equation was obtained:

$$v_{\{110\}} = \frac{\tau_a b}{B(T)} \qquad \text{Eq. 2.5}$$

Where b is the Burgers vector magnitude and B(T) is the temperature dependent damping coefficient. Overall the {112} edge dislocations has two dynamic regimes, the first at low applied stress, where the dislocation moves via thermally activated nucleation of kink pairs. The mobility in this regime is consistent with twinning and antitwinning asymmetry of the (112) bcc slip. At higher stresses, there is a transition to linear mobility, signaling a transition to phonon drag dynamics.

2.3.4 Screw Dislocation in a BCC Metal Structure

A key aspect of bcc materials is that at low temperatures bcc metals do not follow the Schmid law. The Schmid law states that glide on a given slip system starts when the resolved shear stress (RSS) on that system reaches a critical value. In the bcc material there are two major deviations: the first is that the critical RSS depends on the sign of the applied stress (this is a consequence of the twinning/antitwinning asymmetry of the bcc lattice), and second, the critical RSS is influenced by non-glide components of the applied stress tensor. The non-glide components of the applied shear stress are based on the shear stresses in the burgers vector direction acting on planes other than the glide plane, and shear stresses perpendicular to the Burgers vector. Figure 2.15 shows a standard screw dislocation in a bcc material[47].

A key issue with MD modelling of screw dislocations has been correctly modelling the dynamics of screw dislocations. Early potentials predicted that screw dislocations would move on the {112} planes, whereas experimental studies showed that movement of screw dislocations occurred on the {110} plane at low temperatures. A density functional theory (DFT) model of a screw dislocation is able to migrate along the {110} plane. In migrating along the {110} plane, the Peierls barrier is estimated to be between 30-40 meV, with a Peierls stress estimated to be around 1000 MPa, with a lower bound of 620 MPa. Although the Peierls stress was significantly higher than that of a real material, this is most likely an effect of tiny system required for DFT[48]. Although this had a high value for the Peierls stress, it showed that the screw dislocation could move along the {110} plane.

With the introduction of EAM potentials based on DFT based on the concept of a degenerate core spread symmetrically into the three {110} planes. Potentials are now able to create models that agree with the experimental results of the screw dislocation moving along the {110} plane in bcc iron. Prior to dynamic simulations of screw dislocations, some static properties are obtained for the dislocation. Equation 2.6 shows Schmid's law:

$$\tau = \cos\theta \cos\varphi \, \sigma \qquad \text{Eq. 2.6}$$

Where the Schmid factor is the combination of the cosine of the angle between the vector normal to the glide plane(θ) and the cosine of the angle with the glide direction(φ). The Schmid factor multiplied with the stress applied to the material (σ) is a way to calculate the critical reserved stress. As stated earlier in the section due to the relationship between the bcc matrix and the relationship between the antitwinning and twinning direction. This is evident in Figure 2.16 as the RSS based on Schmid's law is compared to the Peierls stress of the screw dislocation in a bcc matrix. The antitwinning and twinning asymmetry is evident in comparing the Peierls Stress for $\chi<0$ and $\chi>0$.

The next step in this study looked at the effect of dynamic movement of the screw dislocation. The study looked at temperatures between 50-150 K and stresses between 200-700 MPa, values significantly below the Peierls stress which is 1210 MPa for the $\chi = 0$ orientation. The glide mechanism at very low temperature or stress tended to nucleate and propagate based on a single kink regime. This regime is defined as the system where the glide is intermittent with a time waiting for the kink pairs that appear one-by-one and annihilate with themselves. The first kink moves the dislocation from its stable soft position to an unstable hard position, while the second kink brings the dislocation back into a stable soft position, in the next Peierls valley.

As the temperature and/or the stress increases, the kink-pair nucleation rate increases and the system moves from a single kink regime to a multiple kink-pair regime, a condition where multiple kink-pairs coexist on the dislocation line. The multiple kink-pair regime is further broken down into further regions. The first is the intermediate regime. The intermediate regime is similar to the single kink regime, with one major difference. The dislocation motion still consists of a waiting period but in this case instead of a single kink moving, you have an avalanche. An avalanche normally consists of 2-3 kink-pairs.

At higher temperatures and/or stresses above the intermediate regime the kink-pair nucleation rate and the number of kink pairs along the {110} planes increases. At these higher rates, the screw dislocation is able to pin itself by a mechanism called cross-kinks. At a cross-kink the dislocation has two potential unlock mechanisms. In one case the combination of kink pairs in both {110} planes, this allows the dislocation to connect on a single {110} plane. This mechanism causes two closed loops to form, one of a vacancy-type and the other of an interstitial type. However, in the case of a very slow velocity of the dislocation it is possible, the cross-kinks are mobile and are able to annihilate with each other. Figure 2.17 shows the visual difference between the single-kink regime and the multiple-kink regime for a screw dislocation.

2.3.5 Dislocation Interaction with Material Defect Structures

As the understanding in the mechanism and movement of dislocations in a bcc matrix are further understood. The next area of improvement is in the effect that defect structures have on the movement of dislocations. As edge dislocations are significantly easier to model, more published work has shown the effect defects have with edge dislocations[49–53]. Over these studies there has been a significant increase in the amount of studies looking at the interactions between voids compared to precipitates in an α-Fe matrix. The key understanding in the climb and glide mechanism of these studies will be investigated to understand the current understanding the mechanism between similar objects to compare to NCs.

Many studies have looked into the effects of edge dislocations with voids. A key part of understanding the interaction between a precipitate and a dislocation is furthering the understanding of the climb mechanism between the dislocation and the precipitate. So just like with NCs, void induced climbing is an important mechanism to understand. In a study looking at the effect of void diameter on the mechanism the surface area of the void plays a major role in the climb mechanism of the dislocation. For small voids, at a diameter of 1.2 nm, the dislocation is able to travel through the nanovoid without any climb motion, but rather by creating surface steps. A major difference with increasing void radius is the change in line of curvature of the dislocation. This phenomenon is shown in Figure 2.18, as it compares a 1.2 nm nanovoid to a 2 nm nanovoid. As the dislocation bows around the nanovoid the surface is much weaker in the case of the 2 nm nanovoid. For the 2 nm nanovoid the dislocation line behaves more similar to a screw dislocation once it interacts with the defect structure. As the dislocation reaches the critical depinning stress, the dislocation climbs over the nanovoid[52].

Along with voids, a study has looked at the pinning effect of a precipitate within the Fe matrix[49]. In the case of a precipitate there is again a strong relationship between the precipitate size and the effect on the edge dislocation. For small precipitates the dislocation is able to easily overcome the dislocation and maintain its original structure. However, for larger precipitates the dislocation will form an Orowan loop around the precipitate. Along with forming a loop around the dislocation, the dislocation also climbs over the precipitate changing the structure of the dislocation. This study shows that a key area of interest in MD simulations is furthering the understanding of the interactions between the climb over a defect structure.

2.4 Long Term Effects in Materials

From the point of point defects forming larger structures the following are major areas of growth within the bulk material[11].

- Growing voids which may lead to swelling within the material .

- Growing interstitial dislocation loops, dislocation climb, and the overall evolution of dislocation structure. This is a primary outcome of the bias of interstitials at dislocation loops, this effect has been shown to reach a saturation level in materials as the system is able to reach a system where an equal amount of dislocation loops are forming and annihilating.
- Radiation-enhanced diffusion and radiation-enhanced precipitation of solutes within the bulk material.
- Radiation-induced solute segregation and radiation-induced precipitation of non-equilibrium phases in solute-enrich regions.

All of these conditions lead to significant changes within the material. The introduction of dislocation loops within the material causes the material to become harder at lower temperatures The increased hardness also leads to a reduction in the fracture toughness of the material as the increased hardness leads to the growth of brittle phases in the material. The introduction of brittle phases in the material, decreases the uniform strain ductility due to an increased yield strength based on the introduction of loops. Creep is also a major area of concern for radiation damage. Along with effects due to the dislocations introduced, the voids cause significant swelling within the material.

At this point the basic evolution from a single cascade to long time growth in defects has been explained. A quick look at what an ideal characteristics a material should have to better hinder the growth of radiation damage and then a look at experimental results of a few key materials for the future. The first step of radiation is during the primary radiation stage, i.e. cascades. Unfortunately this stage is the least controlled process in engineering. No matter the changes to the material the amount of damage created due to a cascade will be nearly identical. So the real changes in a material need to work on mitigating the created point defects within a material. A key area is to create a high number of stable dislocation densities and a large number of incoherent interface areas, as these aspects have been shown to significantly decrease the effects of radiation-enhanced diffusion and radiation-induced segregation.

A system that utilizes microstructures of unbalanced sink strengths between interstitials and vacancies leads to lower swelling rates in materials. Swelling is also shown to decrease with a decreasing dislocation bias. In comparing the bcc and fcc structures, the bcc structure has been shown to outperform the fcc structure in regards to swelling. As the bias is lower for BCC structure compared to the fcc structure based on the dominance of screw dislocation in bcc alloys and defect relaxation volumes. High self-diffusion is also paramount to creating a strong material for radiation, as if defects are able to quickly self-diffuse back it significantly increases the odds of defects returning to lattice points versus becoming interstitials and vacancies.

2.5 Experimental Results of Materials of Interest

One of the key evolutions in nuclear materials for next generation fission and fusion reactors is the switch from the austenitic stainless steel, a fcc based material, to bcc materials. The technology that has been a major area of research for next generation reactors is reduced activation ferritic/martensitic (F/M) steels. This class of steel has shown to greatly outperform current steels in generation III reactors. Along with F/M steels, starting in the late 90s oxide dispersion strengthened (ODS) steels began to be proposed as a potential material for new reactor designs. ODS steels have very high strength via the inclusion of Y-O powders being added to a Ferritic or F/M base alloy. This section will look at the standard F/M steels and discuss the benefits of this material as a comparison to ODS steels.

2.5.1 F/M Steels

Ferritic-martensitic (F/M) steels have been used since the early 1910s. At that time it was found that Fe-based alloys with high Cr (9-12%) are resistant to rusting, while also producing a hard and sharp cutting edge, as such F/M steels were primarily used in knife and blade applications[54]. With continued development, F/M steels significantly improved in the 1930s by including small amounts of C, Mo, W, V, Nb, and N, a steel was developed that had increased creep-rupture strength and further improvements in resistance to corrosion and oxidation. At this point, F/M steels were now being used in the following technologies: chemical plants, gas turbines, boilers, steam power plants, aircraft/aerospace, and nuclear reactor components[54].

In the 1970s, F/M steels began to be proposed for use in nuclear reactors. During that time, austenitic stainless steels were the primary materials in the choice of fuel and cladding applications; however, austenitic stainless steels have been shown to have significant amounts of swelling over long periods of time in a reactor[54]. The benefit F/M steels have over austenitic steels is that F/M steels have much better resistance to swelling, while also having higher thermal conductivity and lower coefficient of thermal expansion[54]. F/M steels superior abilities over austenitic stainless steels made these steels the key material for next generation reactors.

2.5.2 F/M Steels Metallurgy

The process of creating a F/M steel follows 3 general steps: the first consists of austenizing at elevated temperature, second the transformation from austenite to martensite via rapid cooling to room temperature, and third tempering the material at a high temperature to obtain the desirable microstructure and macroscopic properties[54]. Within these three steps many things can be fine-tuned to have a major effect on the strength of the material at the end.

The Fe-Cr equilibrium phase diagram is shown in figure 2.17. 9% chromium F/M steels generally have an austenitic structure (γ-phase) in a temperature range from 850 – 1200 ˚C, with this phase extending out to 12% Cr. Through the inclusion of minor alloying elements the γ-phase can be changed. As elements such as, C, N, Ni, Mn, Cu, and Co can extend the loop. Unlike the following elements that reduced the Cr limit of the loop: Mo, Nb, V, W, Si, Ti, and Al[54]. The resultant phase of the alloy after rapid alloying is based on the Ni concentration and the Cr concentration. Based on those concentrations the resulting microstructure may have a combination of martensite, ferrite, or austenite. A key aspect of F/M steels is in the cooling time, due to the slower cooling using air versus the standard water or oil quenching techniques, the martensitic microstructures tend to form thick laths[54]. At this point, the transformation to a martensitic structure, the material is very brittle and generally not useful.

Thus a tempering process is required to make this material strong and applicable to a nuclear environment. The tempering process allows the material to recrystallize the microstructure and improve other important properties. A key aspect in tempering of the material is to maintain the temperature below the transformation back to an austenitic structure. The temperature that forces the structure to transform back to austenitic is based on the alloying elements, but the temperature is usually between 870-960 ˚C[54]. Tempering temperature also needs to be strategically chosen as at temperatures below 500 ˚C, the softening will be slow. In the range of 500˚- 550˚C, the annealing is much more pronounced[54]. At temperatures above 550˚ C, the microstructure with the combination of softening and the introduction of precipitation, $M_{23}C_6$ carbides or nitrides, the alloy becomes much harder[54]. In general a F/M steel will end the process with tempered martensitic laths with $M_{23}C_6$ along the ferritic grain boundaries. Though finer grains may be found within the martensitic laths or at the boundaries[54].

2.5.3 F/M Steels Limitations

Generation IV nuclear fission and fusion reactors are expected to operate at very high temperatures. Some of these designs are going to exceed 700˚C[4]. Because of high temperature, materials that are used as fuel or structural components are required to exhibit long-term thermal stability, on top of high irradiation resistance, at these conditions. In the case of F/M steels, the application of aging and creep straining at temperatures between 400˚ - 750˚C leads to further precipitation of several possible new phases in the microstructure. The key new phases that form is summarized in figure 2.19. Some popular designs, such as T91 and HT9 gives way to the precipitation of laves phases in these alloys after only ~2 hours of operation at these temperatures.

Due to the creation of precipitates at high operating temperatures, F/M steels are typically limited in thermal creep-rupture strengths above 550˚C[54]. Since some of the generation IV reactors are proposed to run at 700˚C, F/M steels require continued development to achieve this threshold. F/M steels have many areas that could be fine-tuned to further improve these materials and potentially increase the creep-rupture strength of the material. However even with the most perfect F/M steel it is very unlikely that this material will dramatically increase the temperature limits in the foreseeable future[54]. As a result, combing F/M steels with a population of small stable precipitates has gained much more attention due to their increased strength and stability at higher temperatures. The next section will provide an insight onto the development of ODS steels. ODS steels may be a potential solution to the higher temperature and irradiation environments of next generation reactors.

2.5.4 ODS Steels

ODS steels are a variation are a variation of F/M steels, via the introduction of a distribution of small, nanoscale particles intended to enhance the strength of the material at elevated temperatures where F/M steels are limited[54]. ODS steel dates back to the 1960s with a composition of 13% Cr-1.5% Mo and 11-13%Cr-3%W, and the inclusion of small oxide dispersions either Ti_2O_3 or Y_2O_3[54]. The small nanoclusters (NCs) provide additional strength at elevated temperatures, as they effectively inhibit dislocation motion. During the 1960s it was also found out that, these alloys were found to possess very strong swelling resistance during irradiation, even in the presence of He[54], as the oxide NCs provide sites for the nucleation and trapping of He bubbles. Since the 1990s, the development of ODS alloys had been greatly renewed with America, Japan, and Europe actively developing modern ODS steels[55].

In comparing the age of ODS steels to F/M steels, there is a significant drop in experience. However, although ODS steels are in the early stage of their development, these steel’s interest level continues to grow in the nuclear materials field based on ODS steels irradiation resistance and improved mechanical performance at higher temperatures. This section will give a quick overview on the ODS manufacturing process, and the key issues moving forward.

One of the major issues in the production of ODS steels is in the lack of a standardized process in making these materials. The standard process is shown in

Figure 2.20. The process starts with ball milling. Ball milling is a process where the fine powders of the metal are mixed with ultrafine oxide powders (commonly Y_2O_3)[54,55]. After the ball milling process the steel needs to be consolidated. There are a few popular techniques in ODS manufacturing: hot extrusion, hot isostatic pressing, or spark plasma sintering at high temperatures[54–56]. From there, similar to traditional F/M steels, the steel is rapidly cooled to achieve a martensitic structure, followed by a tempering process at elevated temperatures to achieve the final microstructure.

The finished microstructure contains fine grains less than 1 μm in length, thus creating a steel that has enhanced uniaxial creep-rupture strength and ductility. However, creating a steel with equiaxed grains has been a major issue, as many ODS steels tend to have elongated grains leading to anisotropy in mechanical properties[54,55]. Modern ODS steels NCs have consisted of Y-Ti-O structures, with the titanium shown to play a key role in lowering the size of the NCs[55]. The oxide NCs have been shown to improve the radiation resistance of ODS steels compared to F/M steels. The NCs provide a high density of interfaces, which act as sinks for the point defects generated during cascades. The inclusion of NCs within the F/M steel matrix causes a decrease in the number of clusters within the base metal, delaying the nucleation of voids, leading to less swelling within the material. In an ideal ODS materials, an ultrafine density of NCs (a few nm) and are homogenously distributed, to maximize the sink strength of the microstructure

2.5.5 ODS Steels Limitations

In comparing the age of ODS steels to F/M steels, there is a significant age gap. As F/M steels have been a focus in the nuclear field since the 1970s, whereas ODS steels have only been theorized since the 1990s, there is a significant age gap between these two materials. One of the key areas that needs to be addressed for ODS steels is the issue of anisotropy of mechanical properties, which has been shown to be due to elongated grain structures in certain directions[54,55]. A key area in correcting this anisotropy is by perfecting the processing steps in the manufacturing process. Though ODS steels with the inclusion of 9-11% Cr and 2-3% W have shown to have improved anisotropy and in excellent tensile strength[54].

Another key issue that has plagued ODS steel is in producing larger samples. Currently all ODS steels that have shown very good creep strength and irradiation resistance have all been very tiny, slim samples. A methodology for creating thick wall segments out of ODS steels has not been established along with thick walled segments, joining of ODS steels still needs a significant amount of progress to be considered in a real situation, i.e. currently it is impossible to build complex geometry using ODS steel [54]. Although ODS steels have these problems they are still a key material for the future of nuclear due to their high creep strength and irradiation resistance; hence the continued research and development of ODS steels is still a key part of the future of next generation fission and fusion reactors.

2.6 ODS Steel NC Evolution

The benefit ODS steels have over F/M steels and the other options for next generation reactors is the distribution of nanoscale precipitates within the matrix of the base alloy. The key benefit being that the compared to F/M steels, ODS steels have higher strength and creep resistance at higher temperatures[11,55,57,58]. The NCs significantly increase the strength of the material by inhibiting dislocation motion, the inclusion of NCs increases the strength without having a major effect on the ductility, and creates sites for vacancies and He clusters to nucleate, limiting the growth of swelling within the material[11,54,57,58].

A key area of research has started to look into the stability of these NCs over the course of an irradiation. A few of the key areas that have been theorized as controlling the growth or dissolution of these NCs is: 1) ballistic dissolution due to the cascades, 2) radiation-enhanced diffusion, 3) nucleation, and 4) Ostwald Ripening. Upon irradiation, each of these influences are potentially in effect, and the resulting evolution of NCs likely depends on each of these features over long time periods. This section will first look at the basic theories covering these four mechanisms.

2.6.1 Ballistic Dissolution

Ballistic impacts occur constantly within structural materials in a nuclear reactor. These ballistic impacts are caused by PKAs as they are able to knock atoms off of their lattice sites. These cascades are able to overlap NCs, and may potentially lead to the physical dissolution of NC atoms from the NC itself to the surround bcc matrix, resulting in the reduction of size of the NC. This process is often called ballistic dissolution and is controlled by two different mechanisms: first recoil dissolution, and second disordering dissolution[59]. Recoil dissolution is the process of ejection of solute atoms from the NC due to the physical displacement brought on by the PKA, and through the thermal shockwave, the NC atoms are moved to the matrix.

Disordering dissolution refers to the localized disordering of atoms within the damage cascade. These atoms are not physically ejected by the PKA; rather the NC atoms are less bound to the NCs, enabling the NC to be more readily moved in the matrix, resulting in cluster size reduction over larger time periods, of a single cascade. In either the first case or the second case, once an atom is removed from a NC it has the following options: 1. Rejoin the original NC, 2. Join a different NC, 3. Move to another NC via a recoil event, or 4. Stay in the Fe matrix.

MD simulations in this study will look at the primary damage state of a cascade and play a key part in answering and understanding the ballistic dissolution phase of a NC.

2.6.2 Radiation-Enhanced Diffusion

In a system with irradiation the concentration of point defects will exceed those driven by thermodynamics. The higher concentration of defects provides additional vacancies; these vacancies enable atomic transport by diffusion at higher rates[60]. The increased mobility of atoms enables the solutes to migrate more quickly, thus irradiation-enhanced diffusion will have a bigger effect on the NCs. NCs have the opportunity to either grow or shrink due to radiation-enhanced diffusion, dependent on composition gradients. Irradiation results in non-equilibrium conditions, suggesting that during the process the NC population may also be in a non-equilibrium state.

Radiation-enhanced diffusion (D^{irr}) is normally quantified as a comparison of the number of vacancies within the matrix with irradiation and without irradiation[60,61] .

$$D^{irr} = \frac{C_v^{irr}}{C_v^{eq}} D^{th} \qquad \text{Eq. 2.7}$$

Where C_v^{eq} and C_v^{irr} are the concentration of vacancies in equilibrium and during irradiation, respectively. The thermal diffusion rate (D^{th}) is the solute diffusion rate following Arrhenius behavior. C_v^{irr} is approximated as [60].

$$C_v^{irr} = R\tau \qquad \text{Eq. 2.8}$$

Where R is the defect production rate (dpa/s) and τ is the characteristic amount of time required for defects to react with the specific structure within the material. Τ can be described as [60].

$$\tau = \frac{1}{k^2 D_v} \qquad \text{Eq. 2.9}$$

Where k^2 is the sink strength of the structure and D_v is the thermal diffusion rate for vacancies. A key aspect of Eqs 2.7-2.9 is the importance of sink strength in these equations. With higher sink strengths more defects are quickly absorbed by the sink leading to smaller irradiation vacancy concentrations and thus lowering the D^{irr}. These equations show that with the addition of NCs overall the material will be more resistance to radiation-enhanced diffusion.

2.6.3 Nucleation

Nucleation is associated with NC atoms that are displaced through radiation and form new NCs during irradiation. The free energy of nucleation consists of two major considerations: the first is the volume free energy, and the second is the surface free energy[62]. The volume free energy is defined as the difference between the free energy of each phase, whereas the surface energy is a function of the interface between the matrix and the NC. The key aspect of nucleation is the critical radius of a NC. If enough NC atoms are able to surpass the critical radius size, the NC will be more favored to grow.

There are two major types of nucleation: heterogeneous and homogenous[62]. Homogenous nucleation involves the NC forming in the interior of the phase, whereas heterogeneous nucleation is based on a pre-existing surface or interface. Heterogeneous nucleation is more common as the lower surface free energy causes the activation barrier to be lower. However, the key aspect in nucleation is the diffusion rates of the species.

2.6.4 Ostwald Ripening

Ostwald ripening is the process of coarsening of NCs within a material. There are two major types of Ostwald ripening: the standard Ostwald ripening and inverse Ostwald ripening. The first method, Ostwald ripening, consists of smaller particles dissolving, whereas the larger NCs tend to grow due to the redeposition of dissolved solutes from the smaller particles. In this process the net result tends to be an increase in the average size of the particles, along with a decrease in the number density, a theoretical view of Ostwald ripening can be seen in Figure 2.22[63]. Ostwald ripening is driven by the difference in NC interfacial energy. Smaller NCs have higher interface energy and hence are less stable. Thermodynamically, the system is driven to minimize surface area and surface tension. With the goal of lowering the energy of the system on larger time scales the system will try and remove smaller NCs as a smaller number of larger, incoherent NCs are more favorable.

Ostwald ripening is not a new concept, the theory dates back to the late 1950s with two elementary models. The first was the Lifshitz-Slyokov theory; in this theory the reaction rate for Ostwald ripening is limited by the diffusion of atoms in the solution. The other model was the Wagner theory, which assumes that the reaction rate is only limited by the kinetics of the particle-matrix interface[64,65]. The modern and more complete look combines both of these two methods and is called Lifshitz-Slyokov and Wagner (LSW) models.

The current research on modelling Ostwald Ripening has focused on improving the LSW model to better predict the mechanism in more realistic conditions. But simulations are still very far away from modelling realistic materials as binary, ternary and multi-component alloys have been the focus so far[63,65,66]. It has only been recently that studies have looked at correlating these models to irradiation experiments.

Phase-field models have been utilized in simulating Ostwald ripening. The key assumptions of these models have been: one, the transport of mass occurs by diffusion only, and 2) the different NCs are not allowed to coalesce. Another major issue with these models is the assumption that the volume fraction is vanishing, so Kim modified the model to track the volume fraction over time. Figure 2.23 shows the evolution of the number of particles and the particle volume fraction over time[65]. The volume fraction is shown to grow initially before stabilizing over longer time steps and the number of particles is decreasing over the course of the simulation.

Many irradiation studies have shown that ODS NCs coarsen in the same way as predicted by the Ostwald ripening mechanism[67,68]. Observations of NC coarsening have lead studies to correlating the coarsening of the NCs with the irradiation flux proportional to a value of 1/3[60]. However, conflicting results have been published that have instead shown a reduction in average nanocluster size[69]. Other studies have shown a haloing effect around larger NCs[70]. Haloing is the process where the larger NCs breakdown and smaller NCs form around the larger NC.

In the last few sections (2.6.2-2.6.4) the potential methods for the evolution of NCs have been described. In reality, if anyone of these methods was the primary case then the results would be very easy. If it was completely ballistic dissolution, over the course of an irradiation the entire NC population would go away. If Ostwald Ripening was the controlling mechanism the small NCs would completely dissolve, and a point would be reached where the average radius increases and a stable population of NCs is formed. As these are not seen in ODS steels, this suggests that a combination of methods is controlling the evolution of the NCs. In further understanding of the NC evolution during the primary damage state, the beginning portion of the ODS particles will be further understood and may help understand how these mechanisms can occur.

2.6.5 ODS NC Population Statistics

Modern ODS steels contain NCs rich in Y-Ti-O atoms in the manufactured condition. Prior to irradiation these materials are shown to exhibit excellent strength and creep resistance, even at higher temperatures, and are expected to provide resistance to irradiation damage[11,55,57,58]. Any changes made to these NCs over the course of their lifetime in a reactor, would have an effect on these material characteristics, hence understanding ODS steels evolution in irradiation is imperative to put these materials into actual reactors.

There have been many experimental studies on a change in the NC average size, number density, chemistry and crystal structure over the course of an irradiation. However, there has been quite a few problems from all of these studies, succinctly summarized in the following review paper[71]. Some of the key issues are: 1. ODS steels with varying composition, fabrication processing, and heat treatment have various effects on the material and these differences can cause significant changes to the NC evolution. Table 2.4 is from a review on the irradiation evolution of NCs, and shows the inconsistences over the experiments run[71]. From table 2.4 it seems like there are no distinct trends in the evolution of NCs. This section will quickly summarize the key changes seen within a NC over an irradiation.

Experimentalists most used characteristic in looking at the effects an irradiation is the change in average radius, number density, and dose. Figure 2.24 is a summary of the current literature looking at three trends based on irradiation dose and temperature. In case a) the nanoparticle size, b) the number density, and c) the volume fraction. The symbols in figure 2.24 look at the change in the characteristics, specifically the increases, decreases, or if they characteristic stays the same. Figure 2.24 shows no obvious trends over the course of up to 200 dpa.

As changes in figure 2.24 show no conclusive results, experimentalists started to look at different aspects of the NC. A key aspect is the chemistry of NCs using transmission electron microscopy (TEM) with electron energy loss spectroscopy (EELS). In more modern studies, the use of atom probe tomography (APT) has been used often to characterize the NCs. The two key changes monitored in steels is the Y:Ti ratio and the (Y+Ti):O ratio. The Y:Ti ratio is used to understand he stoichiometry of the clusters and the (Y+Ti):O ratio is a comparison of the metal to oxide ratio. Figure 2.25 summarizes many studies looking at dpa and temperature for many experimental results. From these data points again there are no conclusive results. As many cases have seen the Y:Ti ratio increase over the course of the irradiation[60,72–75]. Whereas many cases have also seen the Y:Ti ratio decrease[76–80]. Whereas the (Y+Ti):)O ratio is shown to remain the same[72,73,79]. Another key aspect of evolution within the NC is the inclusion of chromium[81,82] or depletion of aluminum[75].

Another key aspect of the NC within ODS steel is in the crystal structure. As all Y-O oxides have an incoherent relation with a bcc matrix, this incoherency is a key aspect of the effectiveness of the interface as a sink for defects[69,82–85]. In literature, the NCs via high resolution transmission electron microscopy have tended to be coherent with the matrix[52,82,86–88]. Another key aspect of the stability of the structure of NCs during irradiation has been the aspect of the amorphization within NCs.

Many studies experimentally have shown the amorphization of NCs to varying degrees[60,89–92].

Table 2.1. Typical MD cascade parameters and required block sizes. Based on a table in [93].

Neutron Energy (MeV)	Average PKA energy (keV)	NRT displacements	Atoms in Simulation	Lattice Units
0.0034	0.116	1	3456	12
0.0058	0.236	2	6750	15
0.014	0.605	5	6750	15
0.036	1.24	10	54 000	30
0.074	2.54	20	54 000	30
0.19	6.6	50	128 000	40
0.40	13.7	100	250 000	50
0.83	28.8	200	250 000	50
1.8	61.3	400	1 024 000	80

Table 2.2. Number of surviving Frenkel pairs as a function of PKA energy, PKA direction and simulation temperature for bcc Fe[15].

	PKA direction											
	[111]			[112]			[110]			[135]		
	Temperature (K)											
PKA energy (keV)	100	500	1000	100	500	1000	100	500	1000	100	500	1000
1	6	4	3	7	4	3	4	3	3	6	3	2
5	11	8	4	13	9	6	11	8	4	12	9	5
10	19	12	10	21	17	11	12	9	8	17	11	10
20	33	25	17	36	23	18	29	21	14	34	26	19
30	38	33	22	39	37	27	31	27	19	37	31	25

Table 2.3. Nominal chemical composition of several RAFM steels and conventional FM steel[8].

	Mod. 9Cr–1Mo	F82H	Eurofer	INRAFM	CLAM
Cr	8.5	7.7	9	9	9
C	1	0.09	0.11	0.11	0.1
Mn	0.4	0.16	0.4	0.5	0.45
P	<0.020	0.002	<0.005	<0.002	
S	<0.01	0.002	<0.005	<0.002	
V	0.21	0.16	0.2	0.22	0.2
B		0.0002	<0.001	<0.001	
N2	0.05	0.006	0.03	0.03	
O2		<0.01	<0.01	<0.01	
W		1.94	1.1	1.35	1.45
Ta		0.02	0.07	0.07	0.15
Ti		100 ppm	<0.01	<0.005	
Nb	0.08	1 ppm	<0.001	<0.001	
Mo	0.92	30 ppm	<0.005	<0.002	
Ni	<0.20	200 ppm	<0.0050	<0.005	
Cu	<0.10	100 ppm	<0.0050	<0.002	
Al	<0.040	30 ppm	<0.0010	0.005	
Si		1100 ppm	<0.050	<0.05	
Co		50 ppm	<0.0050	<0.005	
Sn		(<20 ppm)			
As		(<50 ppm)	As + Sn + Sb + Zr < 100 ppm	AS + Sn + Sb < 0.03	

Table 2.4. A summary of the irradiation experiments done on ODS materials from a review by Wharry[71].

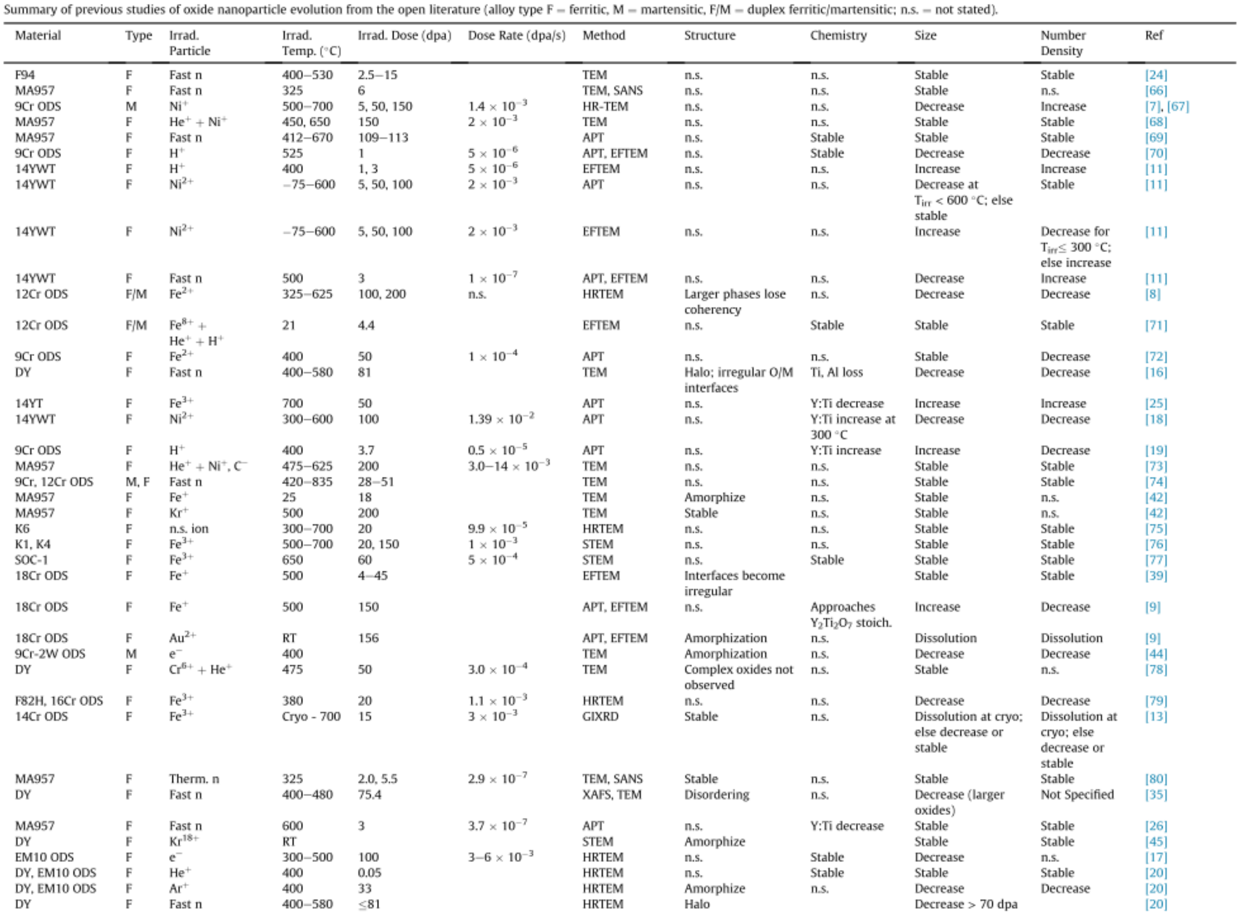

Summary of previous studies of oxide nanoparticle evolution from the open literature (alloy type F = ferritic, M = martensitic, F/M = duplex ferritic/martensitic; n.s. = not stated).

Material	Type	Irrad. Particle	Irrad. Temp. (°C)	Irrad. Dose (dpa)	Dose Rate (dpa/s)	Method	Structure	Chemistry	Size	Number Density	Ref
F94	F	Fast n	400–530	2.5–15		TEM	n.s.	n.s.	Stable	Stable	[24]
MA957	F	Fast n	325	6		TEM, SANS	n.s.	n.s.	Stable	n.s.	[66]
9Cr ODS	M	Ni^{+}	500–700	5, 50, 150	1.4×10^{-3}	HR-TEM	n.s.	n.s.	Decrease	Increase	[7], [67]
MA957	F	$He^{+} + Ni^{+}$	450, 650	150	2×10^{-3}	TEM	n.s.	n.s.	Stable	Stable	[68]
MA957	F	Fast n	412–670	109–113		APT	n.s.	Stable	Stable	Stable	[69]
9Cr ODS	F	H^{+}	525	1	5×10^{-6}	APT, EFTEM	n.s.	Stable	Decrease	Decrease	[70]
14YWT	F	H^{+}	400	1, 3	5×10^{-6}	EFTEM	n.s.	n.s.	Increase	Increase	[11]
14YWT	F	Ni^{2+}	−75–600	5, 50, 100	2×10^{-3}	APT	n.s.	n.s.	Decrease at $T_{irr} < 600$ °C; else stable	Stable	[11]
14YWT	F	Ni^{2+}	−75–600	5, 50, 100	2×10^{-3}	EFTEM	n.s.	n.s.	Increase	Decrease for $T_{irr} \leq 300$ °C; else increase	[11]
14YWT	F	Fast n	500	3	1×10^{-7}	APT, EFTEM	n.s.	n.s.	Decrease	Increase	[11]
12Cr ODS	F/M	Fe^{2+}	325–625	100, 200	n.s.	HRTEM	Larger phases lose coherency	n.s.	Decrease	Decrease	[8]
12Cr ODS	F/M	$Fe^{8+} + He^{+} + H^{+}$	21	4.4		EFTEM	n.s.	Stable	Stable	Stable	[71]
9Cr ODS	F	Fe^{2+}	400	50	1×10^{-4}	APT	n.s.	n.s.	Stable	Decrease	[72]
DY	F	Fast n	400–580	81		TEM	Halo; irregular O/M interfaces	Ti, Al loss	Decrease	Decrease	[16]
14YT	F	Fe^{3+}	700	50		APT	n.s.	Y:Ti decrease	Increase	Increase	[25]
14YWT	F	Ni^{2+}	300–600	100	1.39×10^{-2}	APT	n.s.	Y:Ti increase at 300 °C	Decrease	Decrease	[18]
9Cr ODS	F	H^{+}	400	3.7	0.5×10^{-5}	APT	n.s.	Y:Ti increase	Increase	Decrease	[19]
MA957	F	$He^{+} + Ni^{+}, C^{-}$	475–625	200	$3.0–14 \times 10^{-3}$	TEM	n.s.	n.s.	Stable	Stable	[73]
9Cr, 12Cr ODS	M, F	Fast n	420–835	28–51		TEM	n.s.	n.s.	Stable	Stable	[74]
MA957	F	Fe^{+}	25	18		TEM	Amorphize	n.s.	Stable	n.s.	[42]
MA957	F	Kr^{+}	500	200		TEM	Stable	n.s.	Stable	n.s.	[42]
K6	F	n.s. ion	300–700	20	9.9×10^{-5}	HRTEM	n.s.	n.s.	Stable	Stable	[75]
K1, K4	F	Fe^{3+}	500–700	20, 150	1×10^{-3}	STEM	n.s.	n.s.	Stable	Stable	[76]
SOC-1	F	Fe^{3+}	650	60	5×10^{-4}	STEM	n.s.	Stable	Stable	Stable	[77]
18Cr ODS	F	Fe^{+}	500	4–45		EFTEM	Interfaces become irregular		Stable	Stable	[39]
18Cr ODS	F	Fe^{+}	500	150		APT, EFTEM	n.s.	Approaches $Y_2Ti_2O_7$ stoich.	Increase	Decrease	[9]
18Cr ODS	F	Au^{2+}	RT	156		APT, EFTEM	Amorphization	n.s.	Dissolution	Dissolution	[9]
9Cr-2W ODS	M	e^{-}	400			TEM	Amorphization	n.s.	Decrease	Decrease	[44]
DY	F	$Cr^{6+} + He^{+}$	475	50	3.0×10^{-4}	TEM	Complex oxides not observed	n.s.	Stable	n.s.	[78]
F82H, 16Cr ODS	F	Fe^{3+}	380	20	1.1×10^{-3}	HRTEM	n.s.	n.s.	Decrease	Decrease	[79]
14Cr ODS	F	Fe^{3+}	Cryo - 700	15	3×10^{-3}	GIXRD	Stable	n.s.	Dissolution at cryo; else decrease or stable	Dissolution at cryo; else decrease or stable	[13]
MA957	F	Therm. n	325	2.0, 5.5	2.9×10^{-7}	TEM, SANS	Stable	n.s.	Stable	Stable	[80]
DY	F	Fast n	400–480	75.4		XAFS, TEM	Disordering	n.s.	Decrease (larger oxides)	Not Specified	[35]
MA957	F	Fast n	600	3	3.7×10^{-7}	APT	n.s.	Y:Ti decrease	Stable	Stable	[26]
DY	F	Kr^{18+}	RT			STEM	Amorphize		Stable	Stable	[45]
EM10 ODS	F	e^{-}	300–500	100	$3–6 \times 10^{-3}$	HRTEM	n.s.	Stable	Decrease	n.s.	[17]
DY, EM10 ODS	F	He^{+}	400	0.05		HRTEM	n.s.	Stable	Stable	Stable	[20]
DY, EM10 ODS	F	Ar^{+}	400	33		HRTEM	Amorphize	n.s.	Decrease	Decrease	[20]
DY	F	Fast n	400–580	≤81		HRTEM	Halo		Decrease > 70 dpa		[20]

Table 2.4 (continued)

Material	Type	Irrad. Particle	Irrad. Temp. (°C)	Irrad. Dose (dpa)	Dose Rate (dpa/s)	Method	Structure	Chemistry	Size	Number Density	Ref
								Al, Ti loss < 70 dpa; else stable		Decrease >70 dpa	
DY, EM10 ODS	F	e^-	300–550	33	$3–6 \times 10^{-3}$	HRTEM	n.s.	Stable	Decrease	Decrease	[20]
12YWT	F	Fe^+	300	0.7	1.9×10^{-4}	APT	n.s.	Stable	n.s.	Stable	[81]
12Cr, 14Cr ODS	F	$Fe^{5+} + He^+ + H^+$	RT, 600	10–30	1×10^{-3}	PAS	Vacancy cluster-Cr complexes	n.s.	Stable	n.s.	[54]
14LMT	F	Fe^{2+}	30	10–100		APT, EFTEM	n.s.	Stable	Stable	n.s.	[29]
14LMT	F	Fe^{2+}	500	10–100		APT, EFTEM	n.s.	Cr, La pickup	Decrease	Stable	[29]
Eurofer 97 ODS	F/M	H^+	40	0.3, 1, 2		TEM	Amorphize particles <20 nm	n.s.	n.s.	Stable	[46]
18Cr ODS	F	Xe^+	27, 500	2.5		TEM	Amorphize at $T_{irr} = 27$ °C	n.s.	Increase at $T_{irr} = 27$ °C; else stable	n.s.	[47]
MA957	F	Fe^+	500	150	6.5×10^{-4}	HRTEM, EFTEM	Stable	n.s.	Increase	Decrease	[10]
MA957	F	Fast n	412, 430	50, 75	1.3×10^{-7}	HRTEM, EFTEM	Stable	n.s.	Stable at $T_{irr} = 412$ °C; else increase	Stable at $T_{irr} = 412$ °C; else decrease	[10], [36], [37]
14Cr ODS	F	Fe^+	500	150		EFTEM	n.s.	Stable non-stoich.	Increase	Decrease	[30]
Fe-Y_2O_3 ODS	F	Fe^+ with/out He^+	500, 600	100		TEM, SANS	n.s.	n.s.	Stable at $T_{irr} = 500$ °C; else increase	Stable	[60]
Eurofer 97 ODS	F	Fast n	330	32		APT, TEM	n.s.	V loss, Y pickup	Dissolution (of particles > 10 nm)	Increase	[21], [22]
Eurofer 97 ODS	F	Fe^+, Fe^{2+}, Fe^{3+}	RT	32		APT, TEM	n.s.	V, N Loss	Dissolution	Stable	[82]
Eurofer 97 ODS	F	Fe^{2+} and Ti^{2+}	RT	0.8–0.9		APT, TEM	n.s.	Y, O, Mn pickup	Decrease	Increase	[23]
13.5Cr ODS	F/M	Ti^{2+}	RT, 300	0.8–2.4		APT, TEM	n.s.	O pickup; Y:Ti decrease	Stable	Increase	[23]
13Cr ODS	F	e^-	400, 500	12	2.2×10^{-3}	TEM	n.s.	n.s.	Difficult to discern	Difficult to discern	[83]
14Cr ODS	F	$Fe^{5+} + He^+ + H^+$	600	30		EFTEM	n.s.	Stable	Increase	Stable	[84]
Eurofer 97 ODS	M	H^+	40, 350	0.3–2.0		TEM	n.s.	n.s.	Stable	Stable	[85]
Cr16 ODS, EP450	F	Bi^+, Xe^+	350–650			HRTEM	Amorphous ion tracks	n.s.	Decrease for T_{irr}>600 °C	Stable	[41]
EP450	F	Xe^+, Kr^+, Ar^+	RT			HRTEM	Amorphous ion tracks	n.s.	n.s.	n.s.	[86]
9Cr ODS	F	H^+	500	3	1×10^{-5}	APT	n.s.	Stable	Decrease	Stable	[14], [15]
9Cr ODS	F	Fast n	500	3	1×10^{-7}	APT	n.s.	Y:Ti increase; (Y + Ti):O stable	Decrease	Decrease	[14], [15]
Eurofer 97 ODS	M	Fe^{2+}	400	2	$\sim 1 \times 10^{-4}$	APT	n.s.	Stable	Stable	Stable	[31]
1DS	M	Fast n	450–560	10.5–21		TEM	n.s.	n.s.	Decrease	Decrease	[27]
1DK	F	Fast n	450–560	10.5–21		TEM	n.s.	Y:Ti decrease	Increase	Decrease	[27]
F95	F	Fast n	400–530	2.5–15		HRTEM	Stable	Y:Ti decrease for $T_{irr} \geq 500$ °C	Stable	Stable	[24], [28]
M93	M	Fast n	400–530	2.5–15		HRTEM	Stable	Y:Ti decrease	Stable	Stable	[24], [28]
MA957	F	Fast n	500, 700	100	1.2×10^{-6}	TEM	n.s.	n.s.	Increase	Decrease	[38]
16Cr ODS	F	e^-	500	10		TEM	Stable	n.s.	Decrease	Stable	[55]
K3	F	Fe^{3+}	300, 500	1–10	1×10^{-3}	TEM	n.s.	n.s.	Stable	Stable	[87]
12.5Cr ODS	F	$e^- + H^+$	350–550	15	2×10^{-3}	TEM	O/M interface becomes irregular	n.s.	Stable	Stable	[40]
9Cr ODS	F	Fe^{2+}	500	3, 100	1×10^{-4}	APT	n.s.	n.s.	Decrease	Decrease	[12]
PM2000	F	Fast n, He^+	500	21		EFTEM	Amoprhization; faceted shape becomes spherical	Cr-rich shells	n.s.	n.s.	[88]

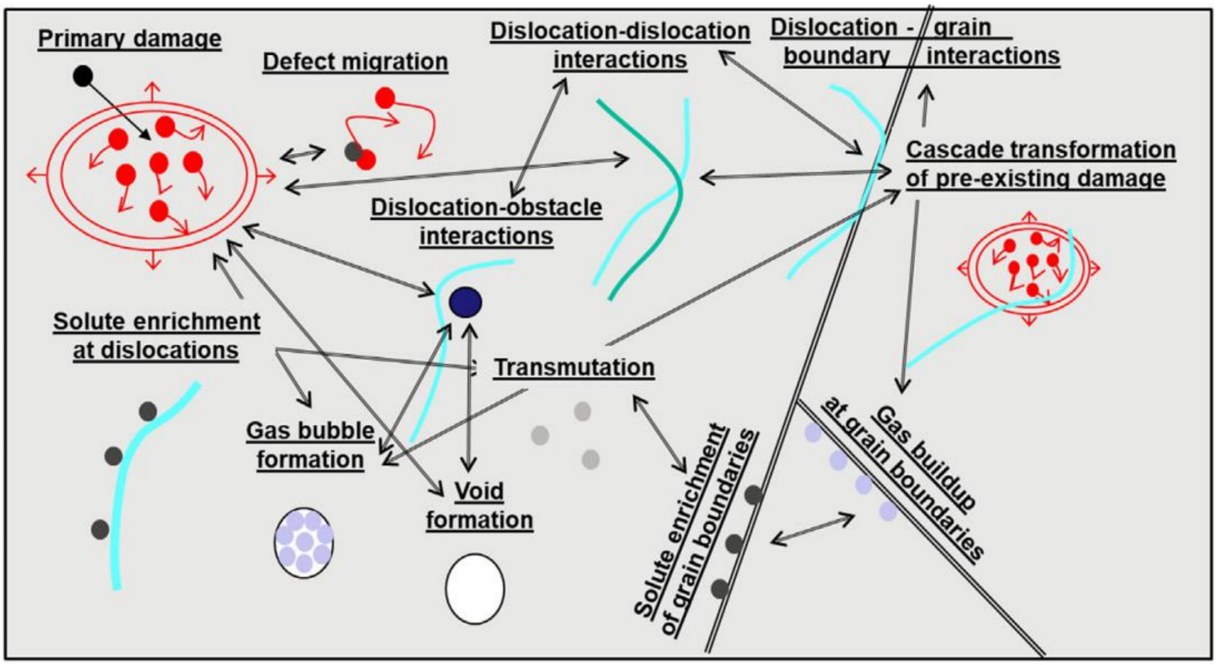

Figure 2.1. Looking at the stages of defect production and migration in a material[31].

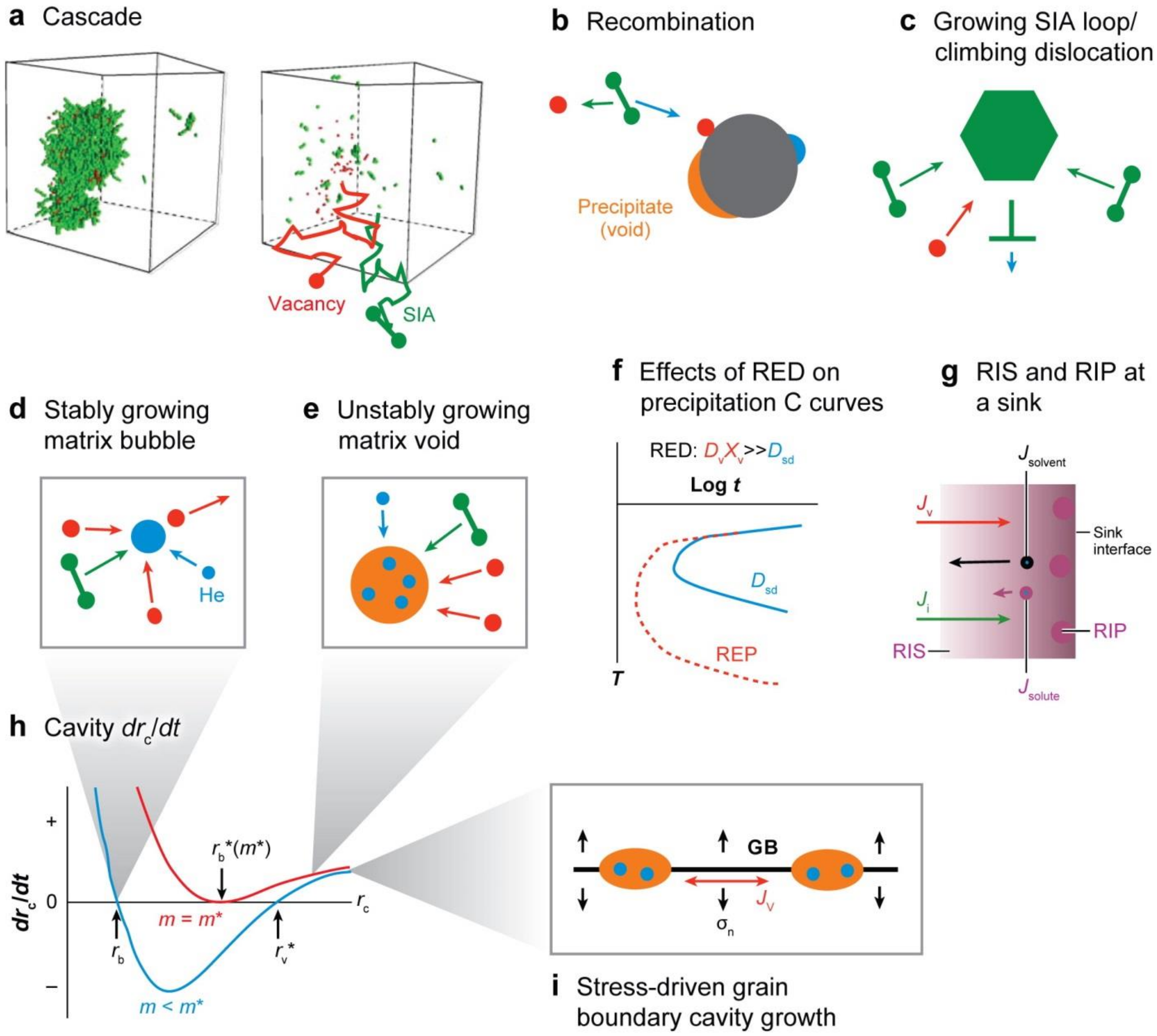

Odette GR, et al. 2008.
Annu. Rev. Mater. Res. 38:471–503.

Figure 2.2. The evolution of how radiation damage generates point defects. The point defect evolution to larger microstructural defects is shown[11].

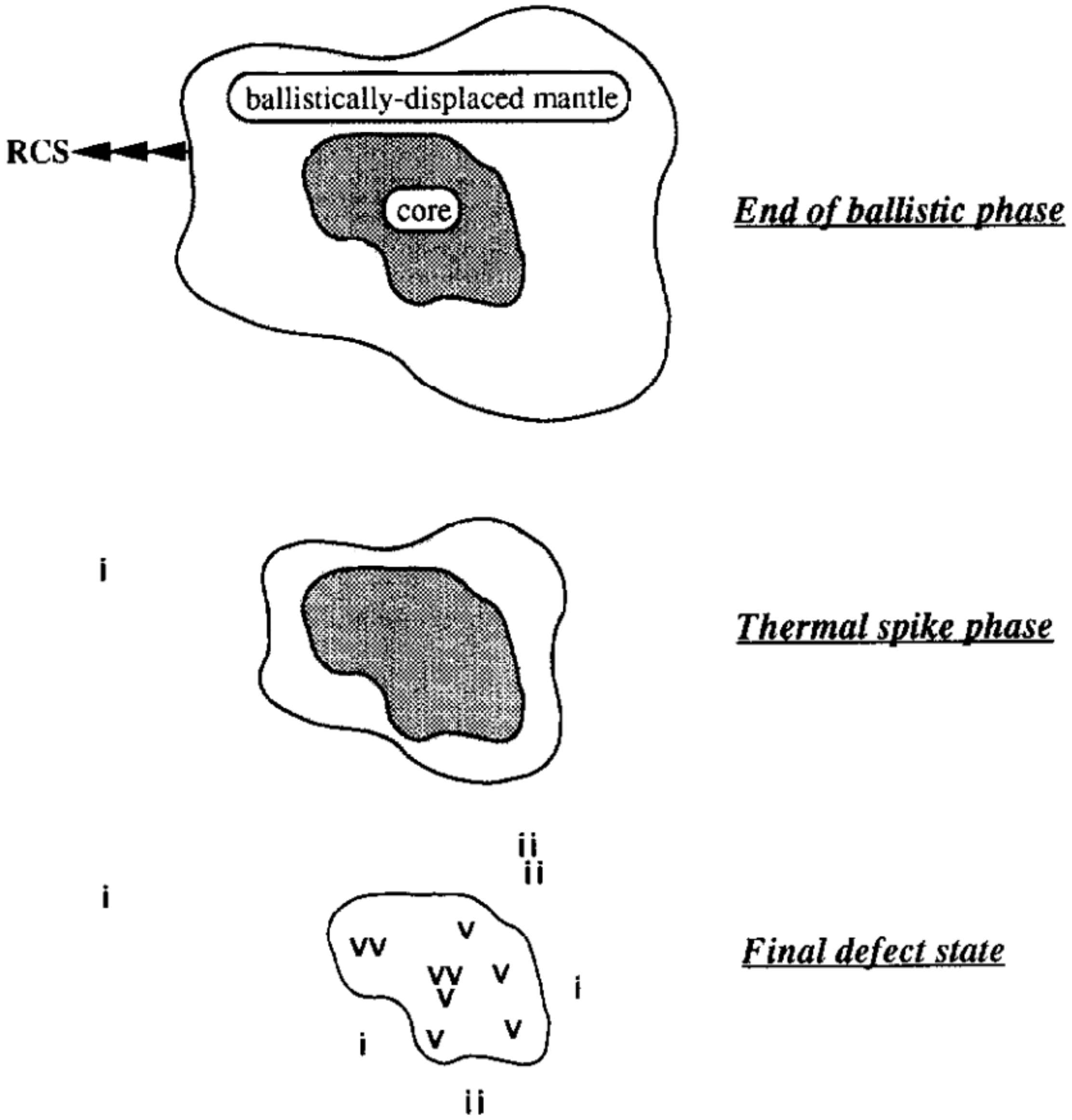

Figure 2.3. The evolution of a cascade modelled by MD[25].

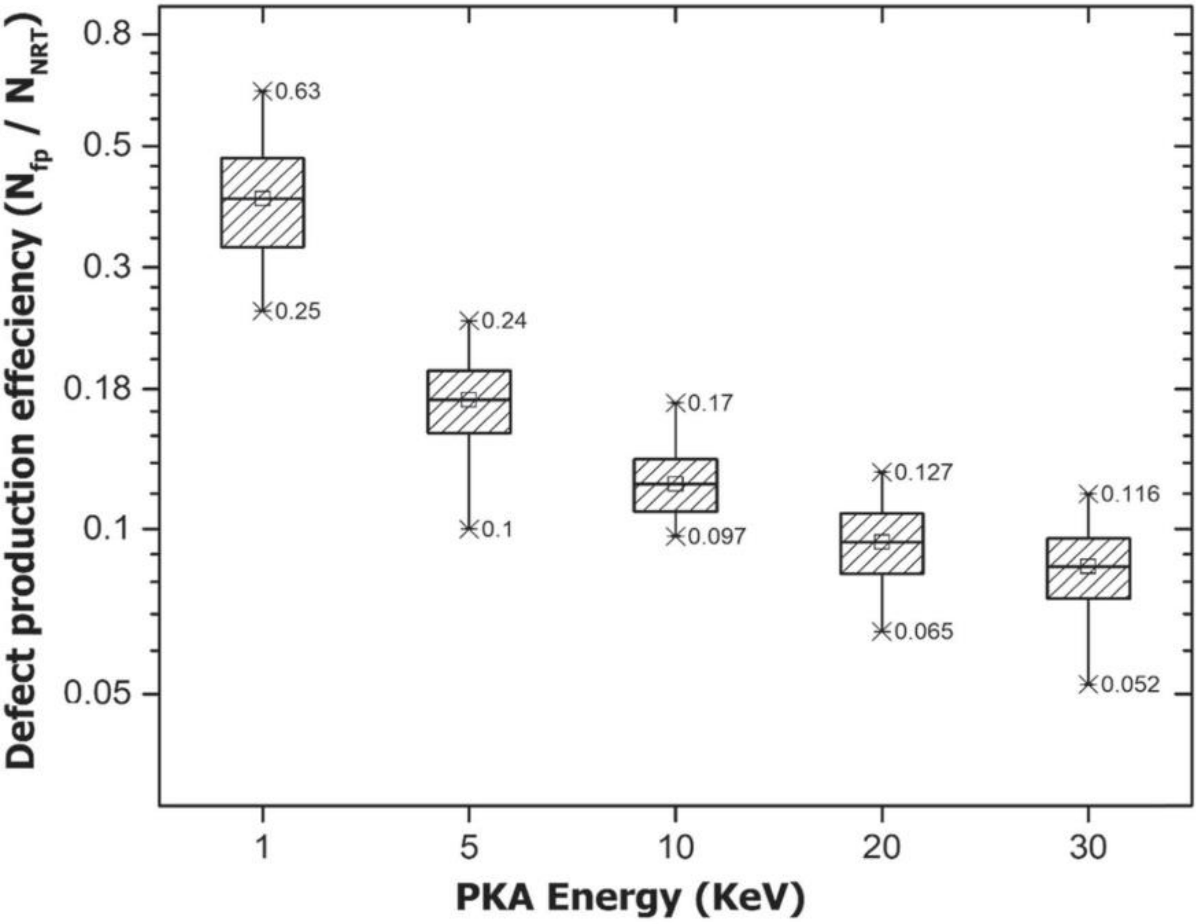

Figure 2.4. Ratio of the number of surviving Frenkel pairs to the NRT model based on PKA energy[15].

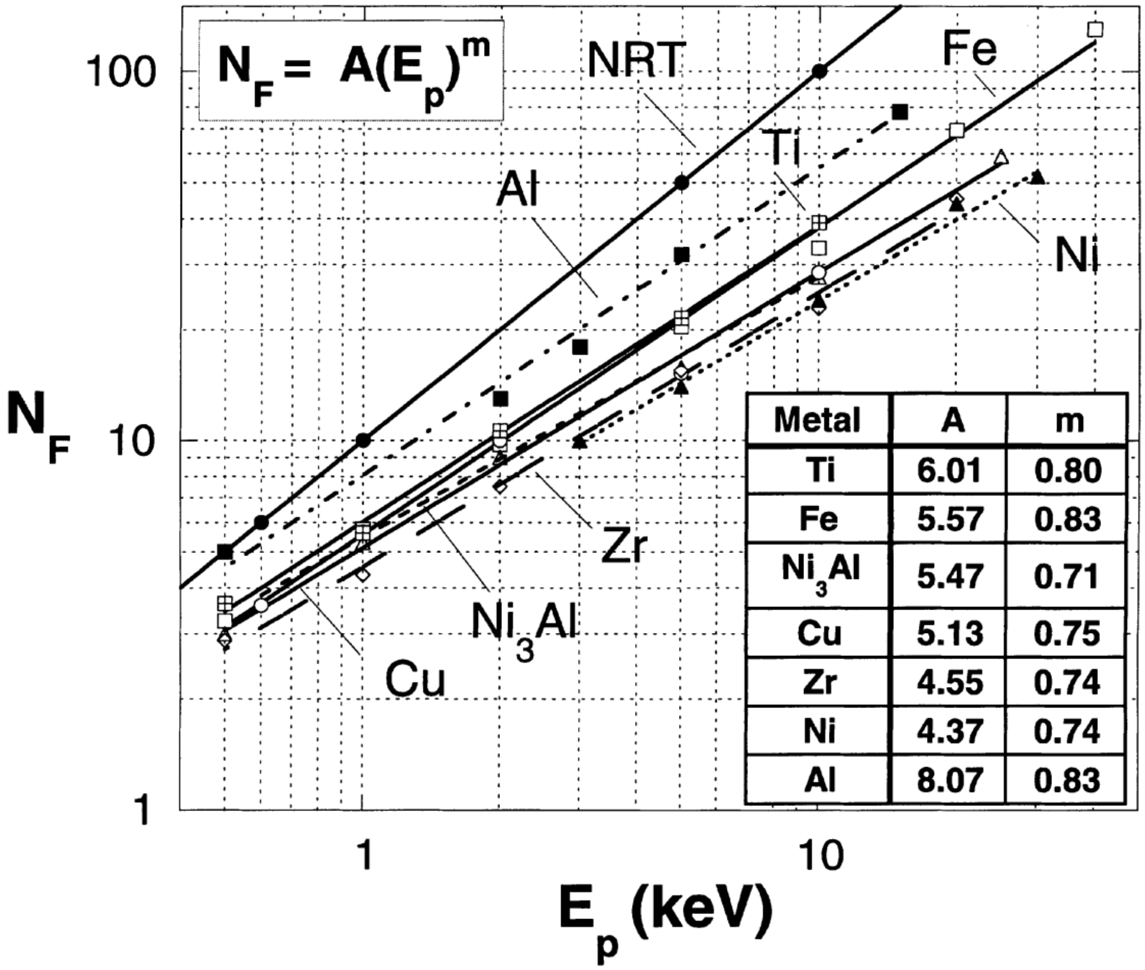

Figure 2.5. log-log plot of NF vs Ep for various metals at 10 K up to 40 keV, demonstrating the power–law dependence of Equation 2.2[14].

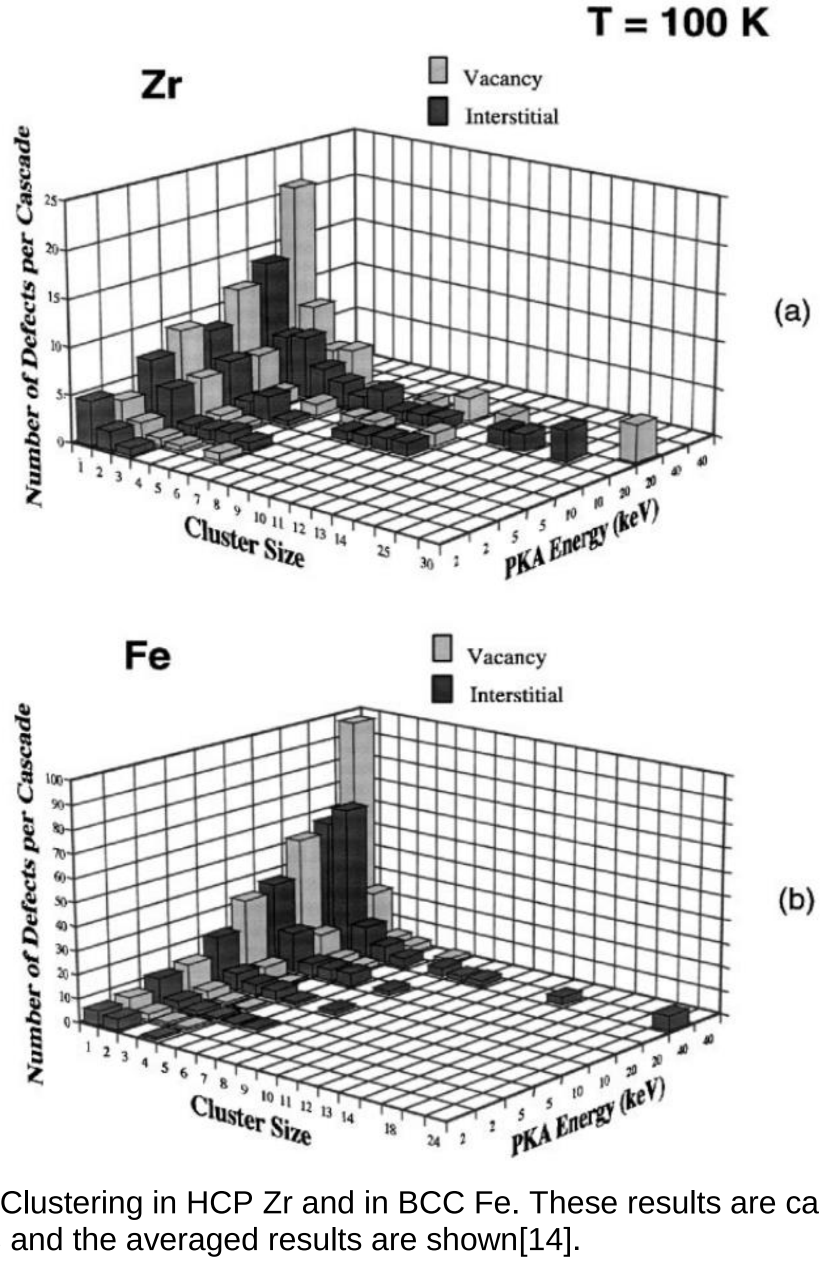

Figure 2.6. Clustering in HCP Zr and in BCC Fe. These results are calculated for all energies and the averaged results are shown[14].

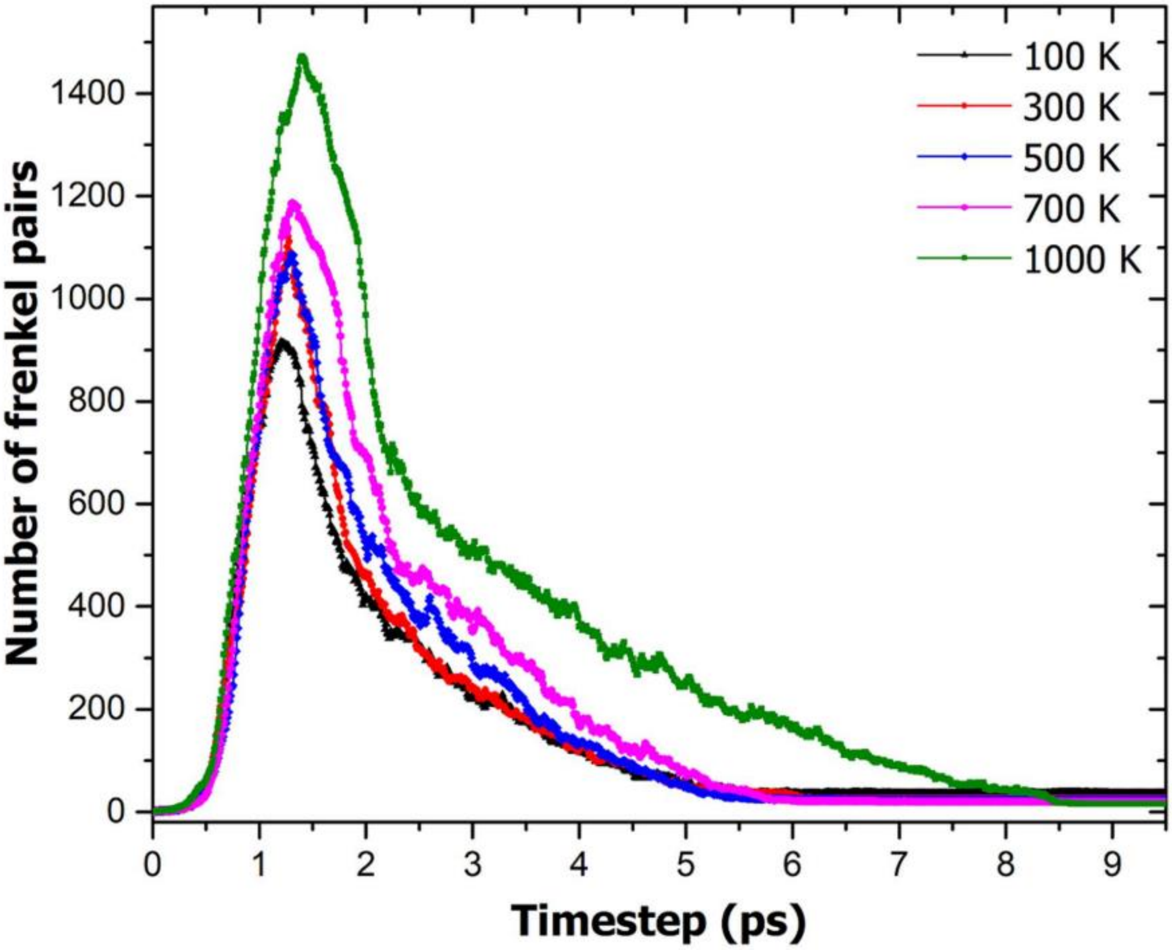

Figure 2.7. The effect of temperature is investigated for a 20 keV Fe cascade[15].

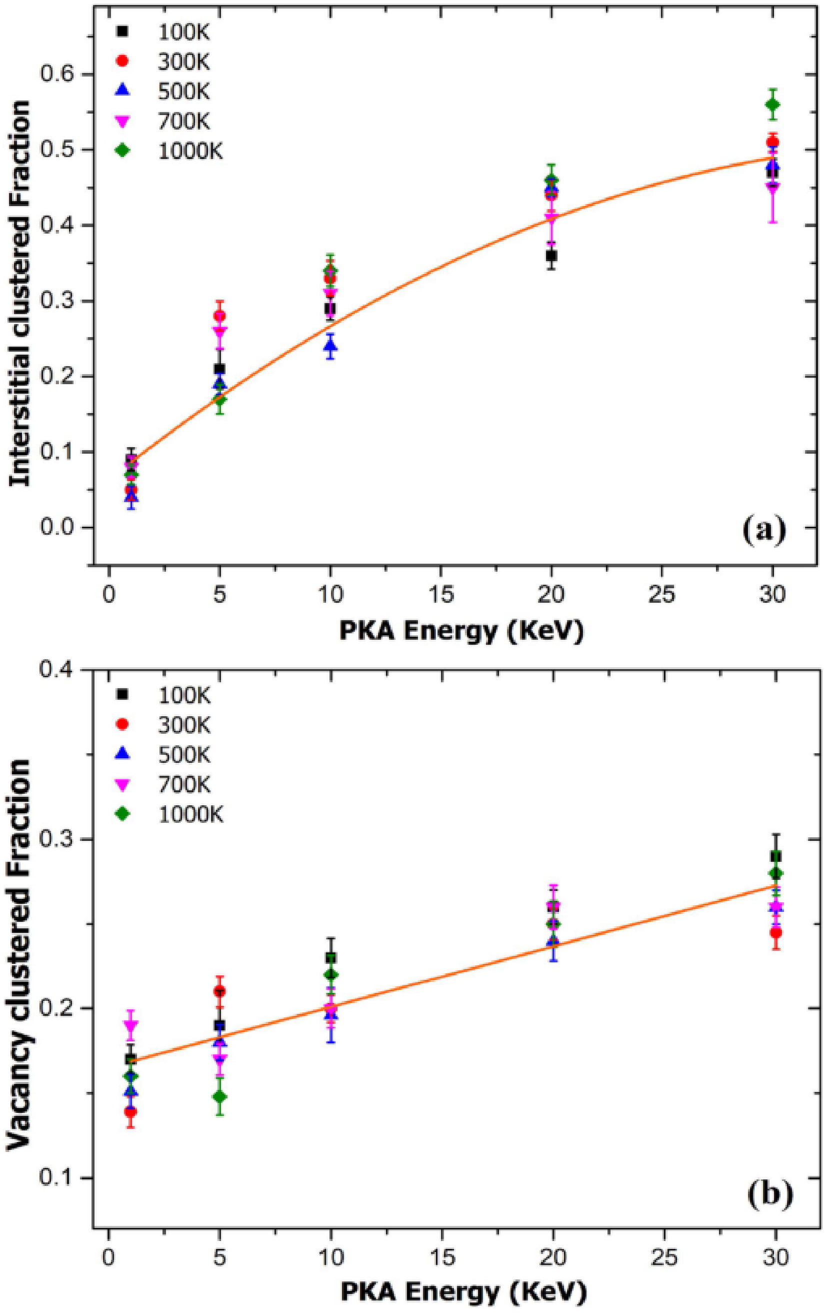

Figure 2.8. The clustering of defects within the Fe matrix[15].

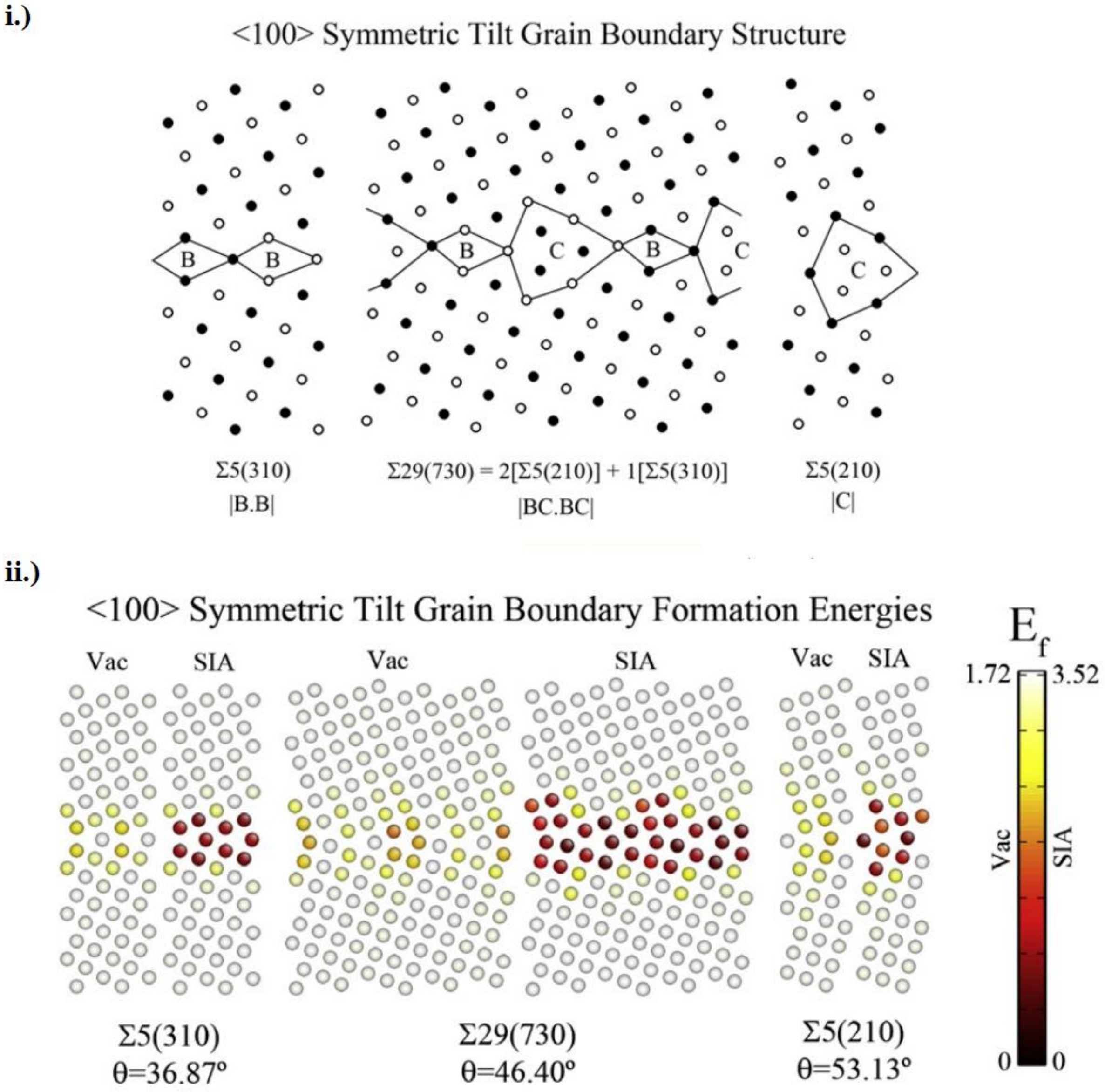

Figure 2.9.i.) <100> symmetric tilt grain boundary structures with structural units outlined for three cases of GTGBs. Black and white denote atoms on different {100} planes. ii.) the vacancy and self-interstitial atom formation energies as a function of location[34].

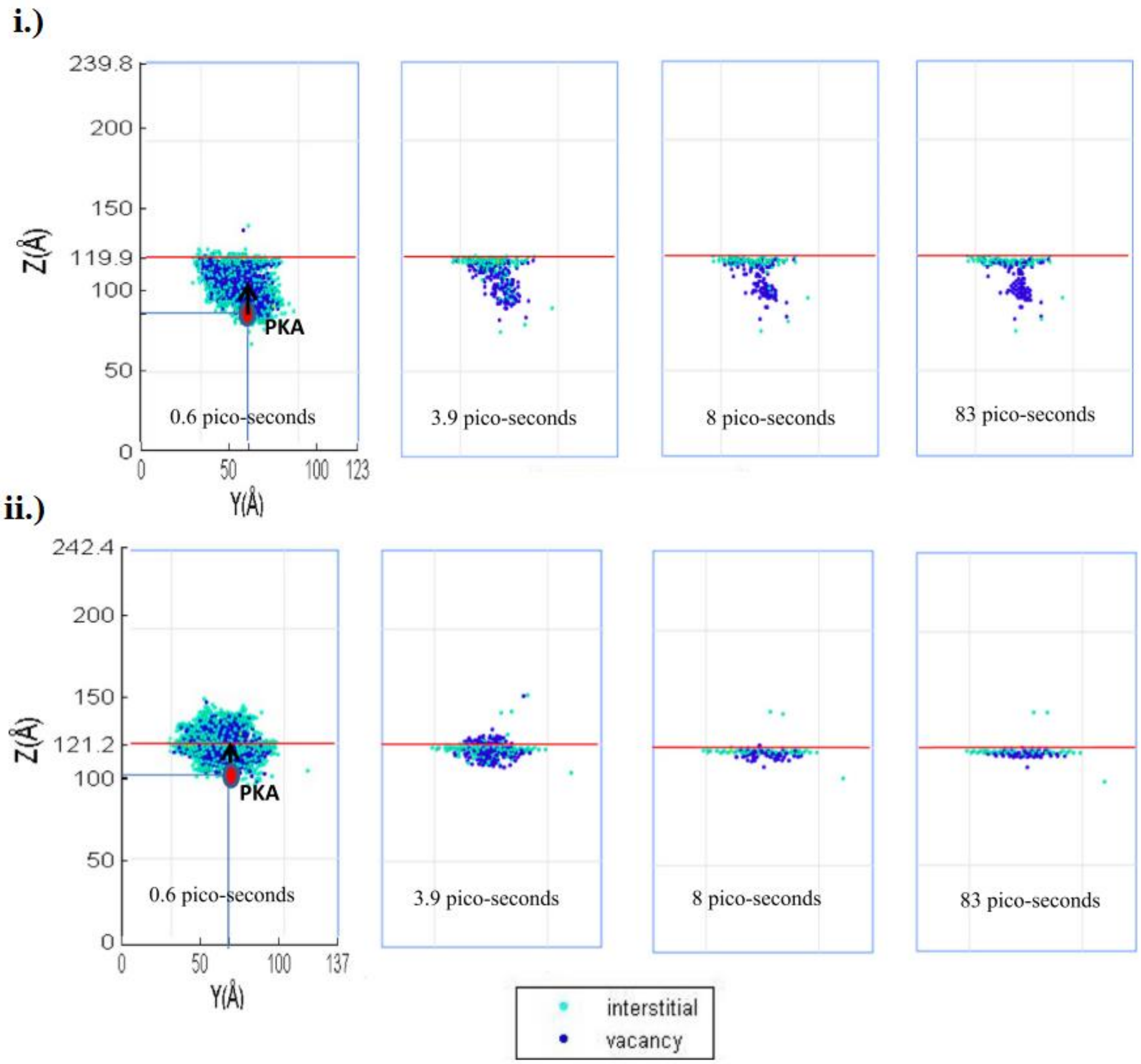

Figure 2.10. Snapshots of a 6 keV PKA interacting with a dislocation (red line). i.) high angle grain boundary. ii.) low angle grain boundary[35].

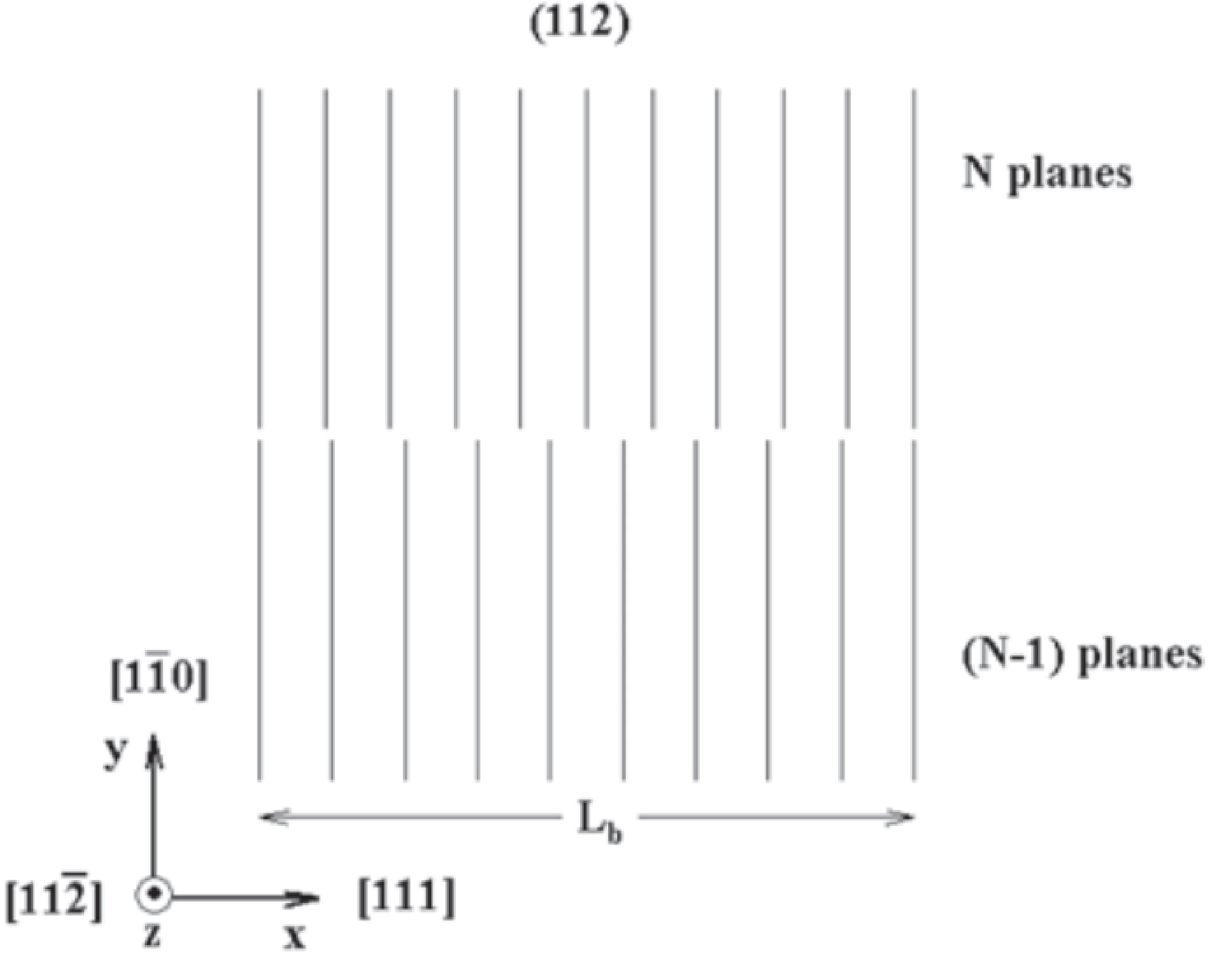

Figure 2.11. Schematic visualization of two half-crystals with a different number of y-z planes for construction of a ½ <111> {110} edge dislocation[44].

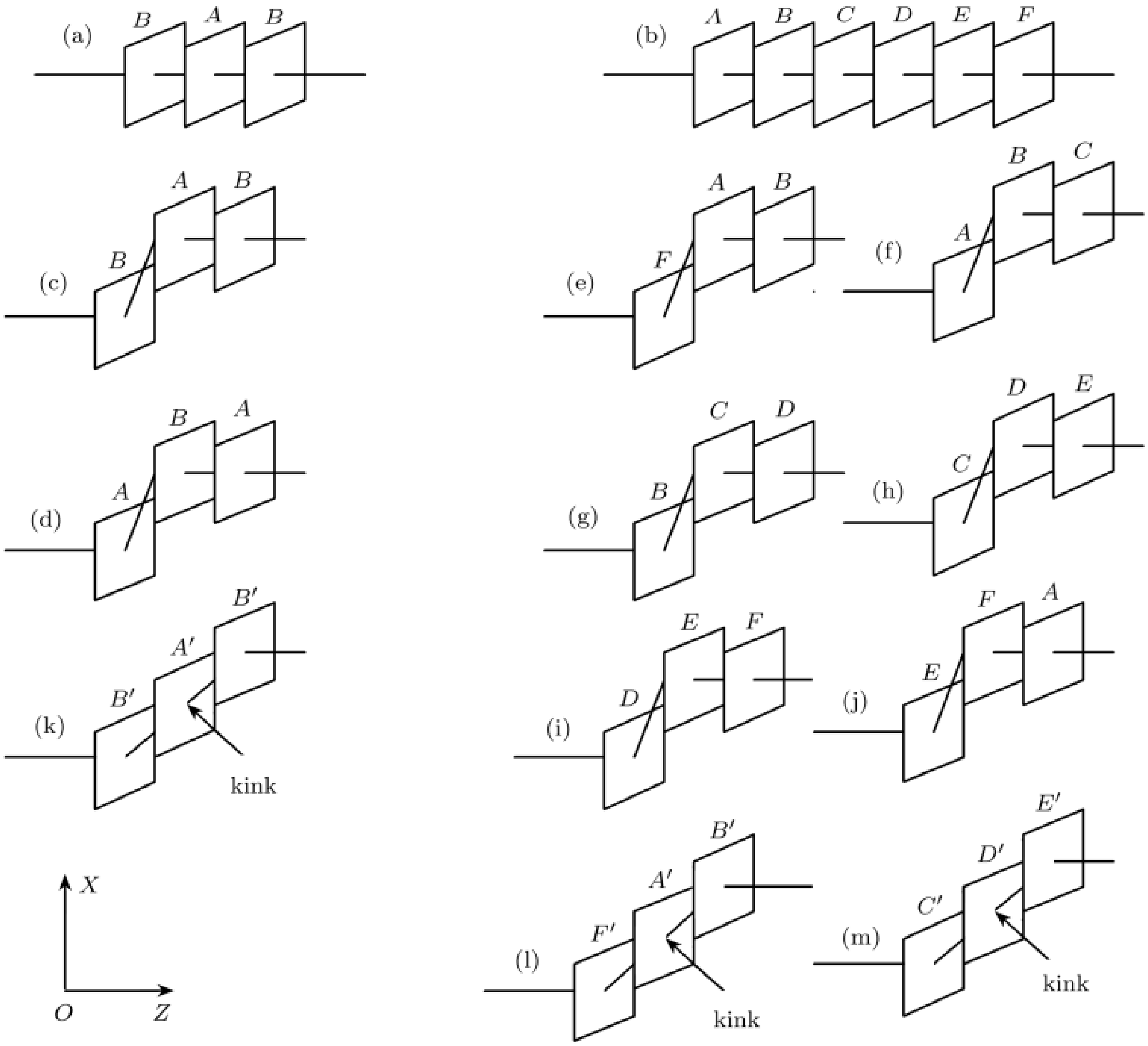

Figure 2.12. A schematic representation for the stacking sequence of atomic planes in the EDs, the types of the initial kinks, and the types of the kinks after the relaxation. (a) the ½ <111> {112} ED; (b) the ½ <111> {011} ED; (c) and (d) the initial kinks for the ½ <111> {112} ED; (e)–(j) the initial kinks for the ½ <111> {011} ED; (k) the kink in the ½ <111> {112} ED after the relaxation; (l) and (m) the kinks in the ½ <111> {011} ED after the relaxation[45].

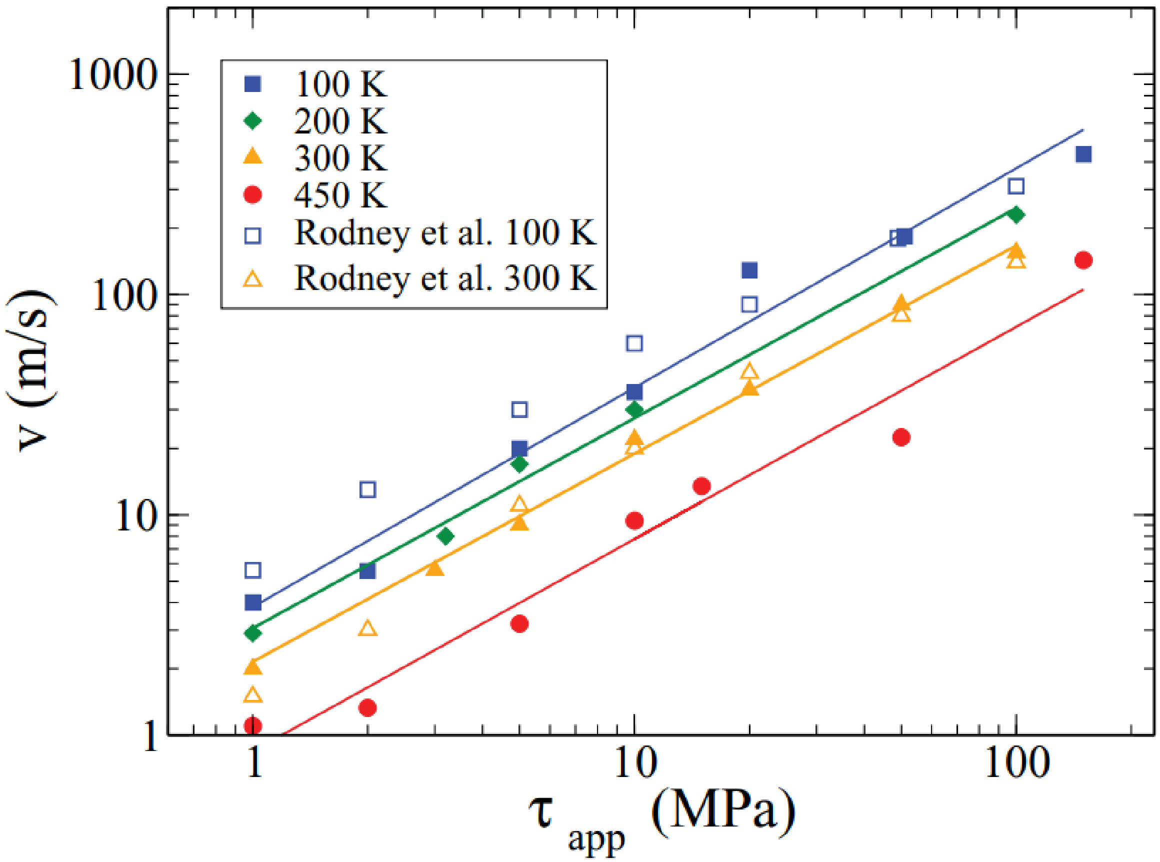

Figure 2.13. Mobility of a 1/2 <111>{110} edge dislocation in Fe for different applied shear stresses and temperatures[94].

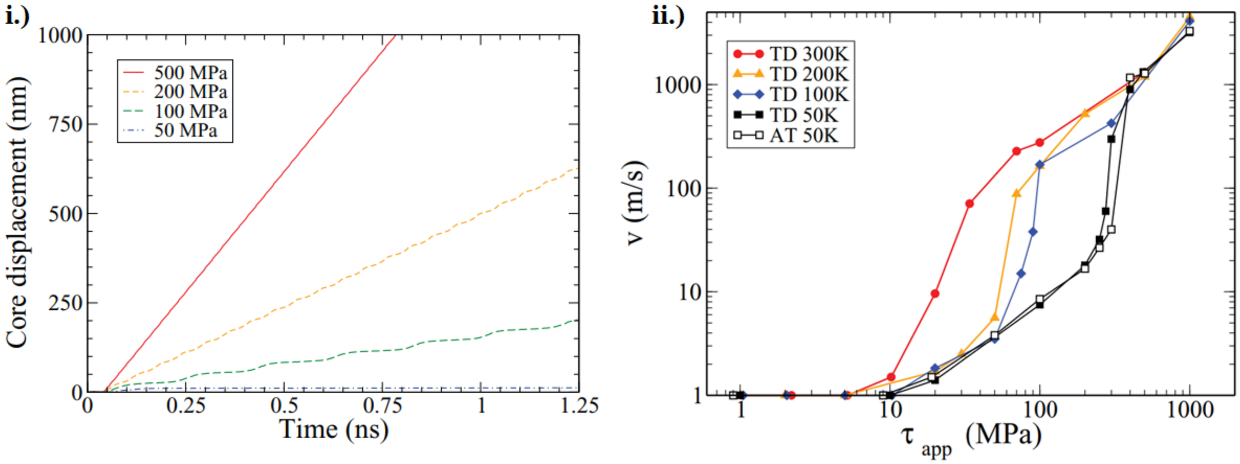

Figure 2.14. i.) Time-displacement curve for an edge dislocation gliding on a {112} plane at 200K at different applied stresses. ii.) Edge dislocation velocities on (112) planes as a function of applied stress and temperature. TD represents twinning direction, white AT indicated antitwinning direction[94].

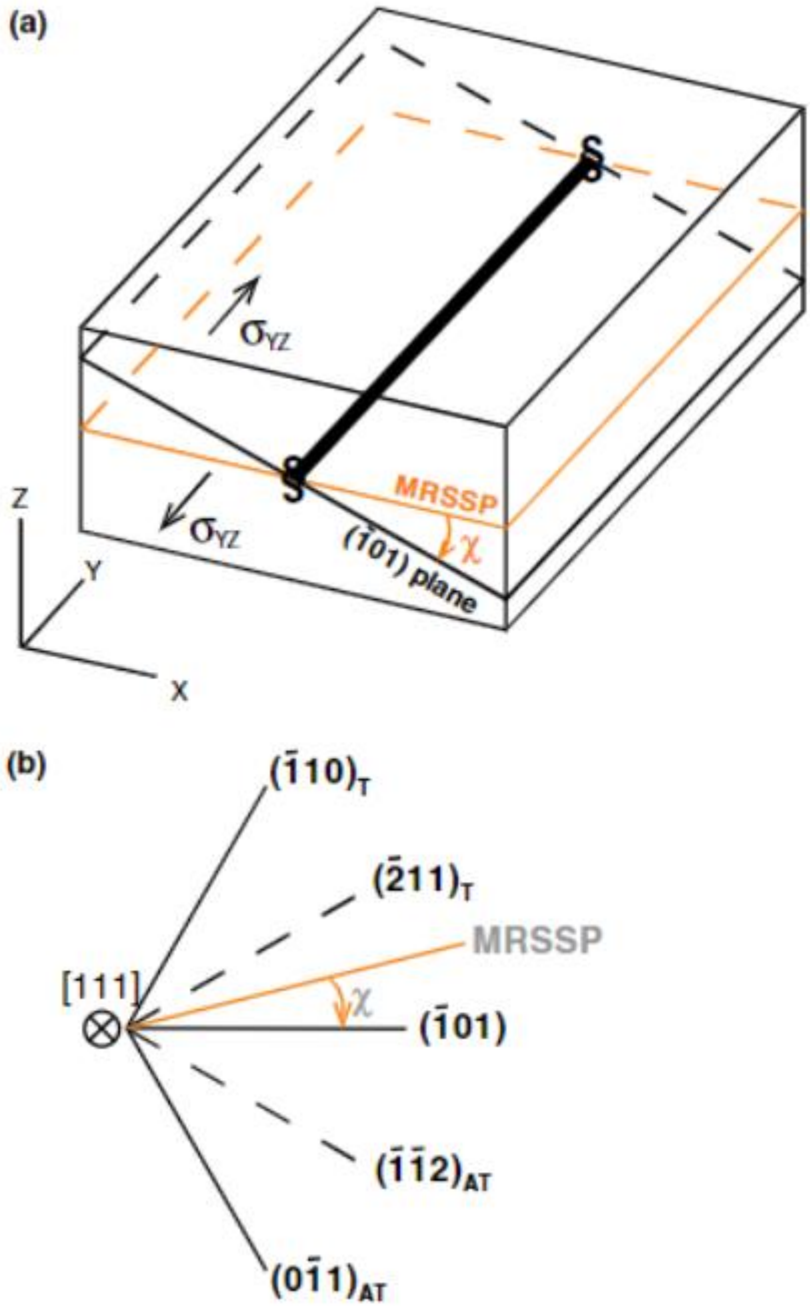

Figure 2.15. A schematic of the standard screw dislocation in bcc Fe[47].

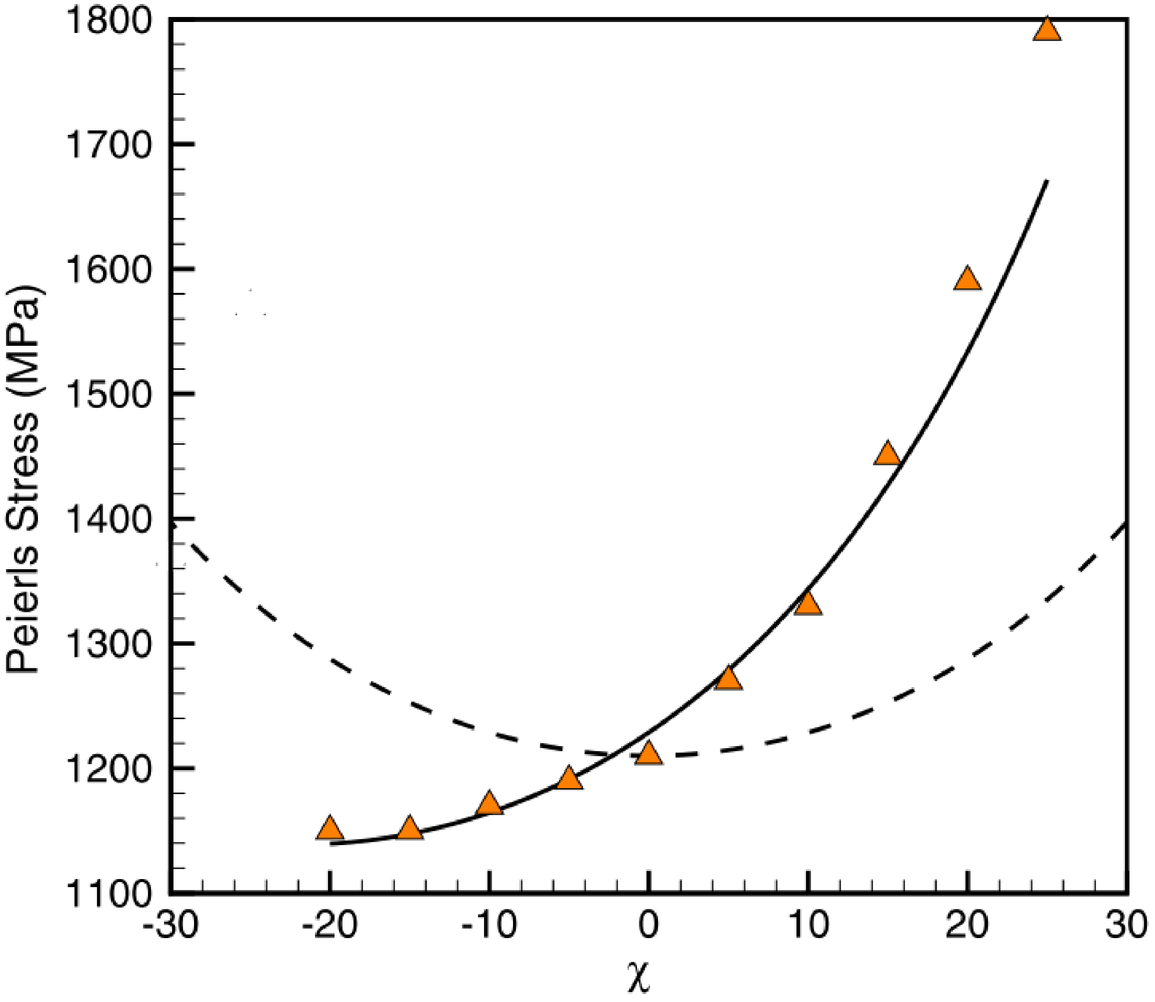

Figure 2.16. A comparison between Schmid law (dashed curve) and an effective Peierls stress relation (solid curve)[47].

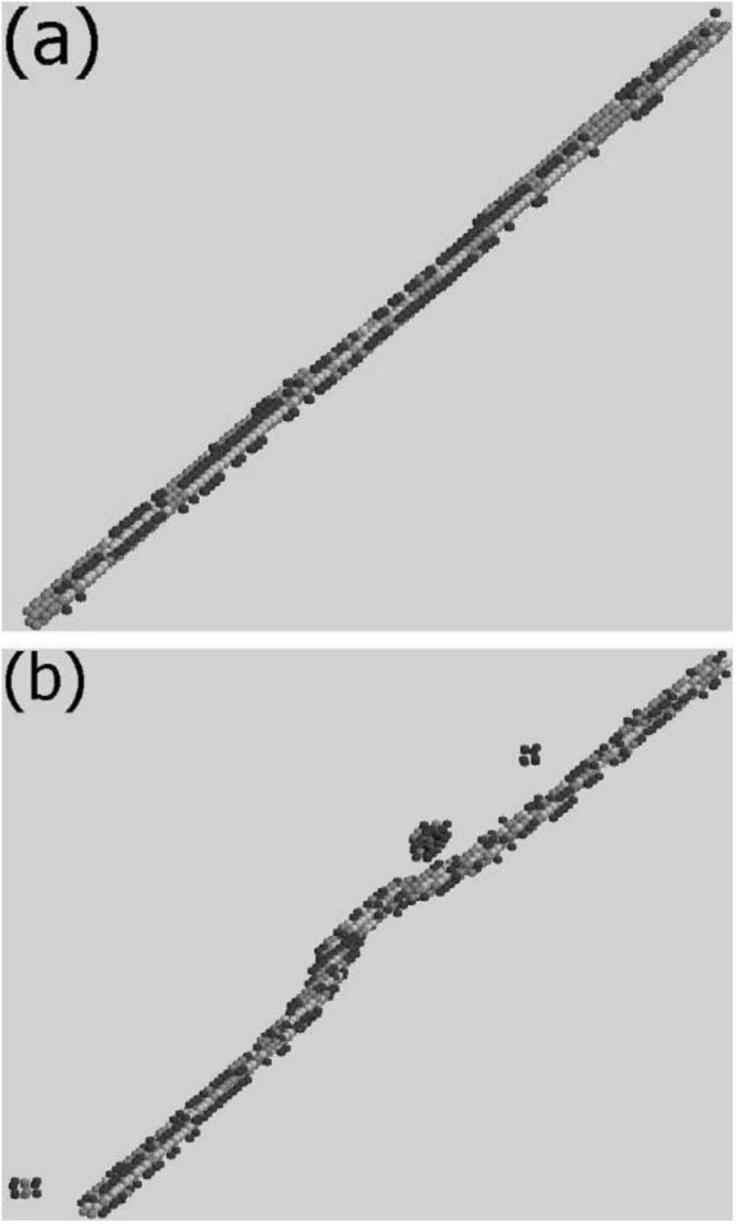

Figure 2.17. Core structures obtained with a first-neighbor analysis in (a) the single-kink pair regime (400 MPa, 50 K), (b) the rough multiple-kink pair regime (500 MPa, 150K)[47].

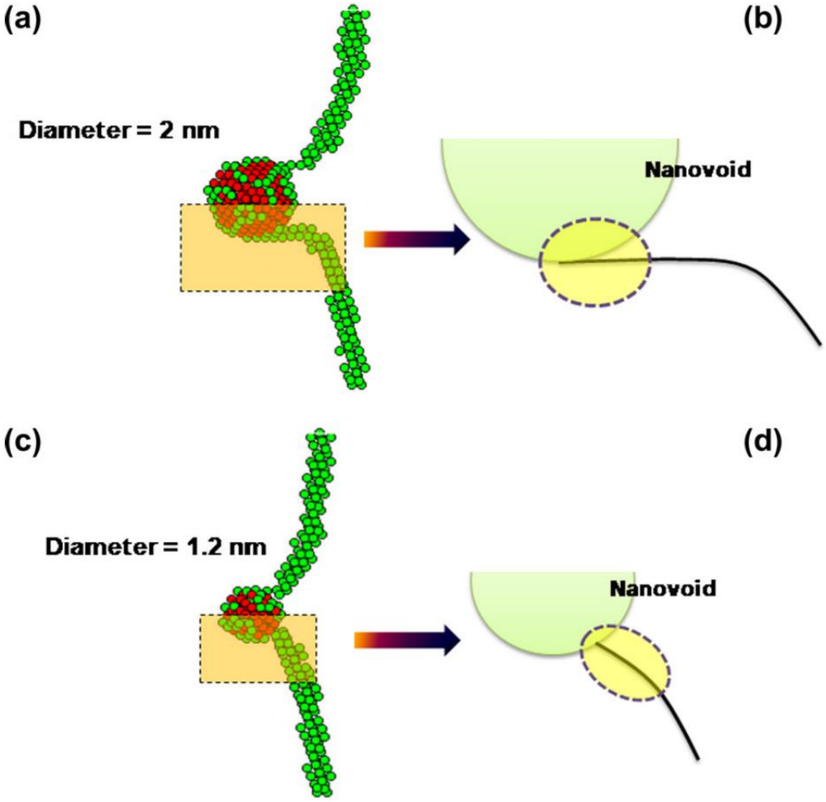

Figure 2.18. Bow-out of dislocation arms during depinning at the nanvoids. (a) for the 2 nm nanovoid a large curvature of the dislocation arm causes a small inclination with the surface of the nanovoid. (b) the pinned dislocation segment has a larger field of interaction with surface atoms, which provides a barrier-free path to initiate the void induced climb. (c) In contrast, the curvature is small for the 1.2 nm nanovoid and (d) the field of interaction is significantly reduced. In the MD snapshots shown here the dislocation line consists of straight segments instead of having continuously varying curvature. This is due to the atomistic discreteness of the lattice and the orientation-dependent line tension, which aligns the dislocation segments along the rational crystal directions so that the line can attain an energetically favorable shape[52].

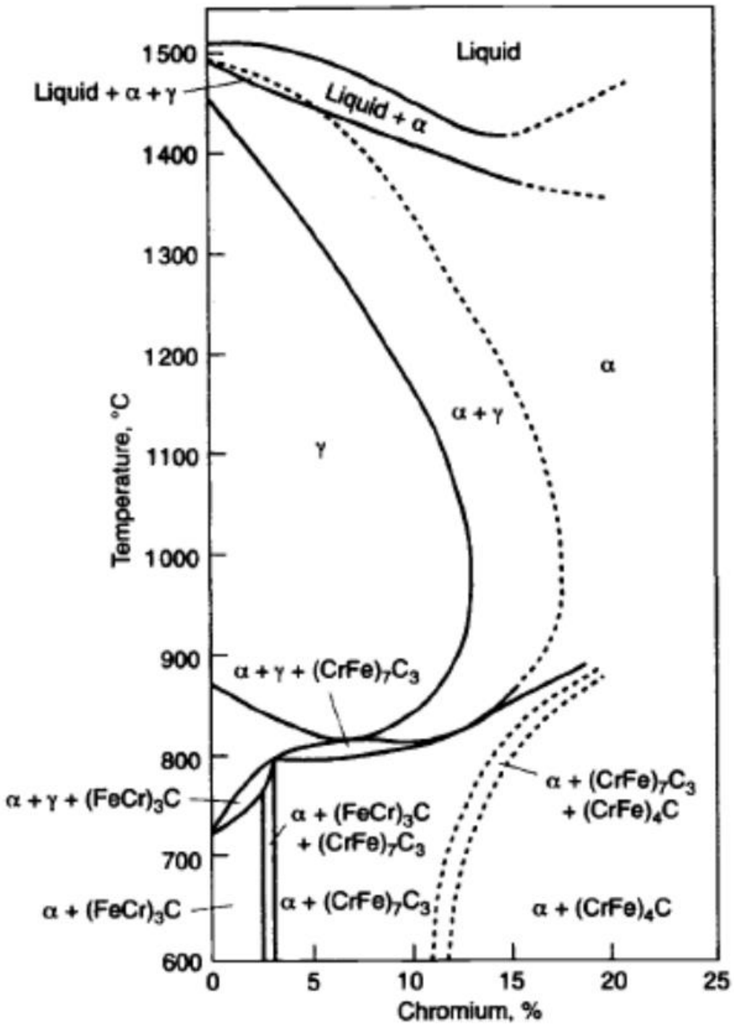

Figure 2.19. Fe-Cr equilibrium phase diagram[54].

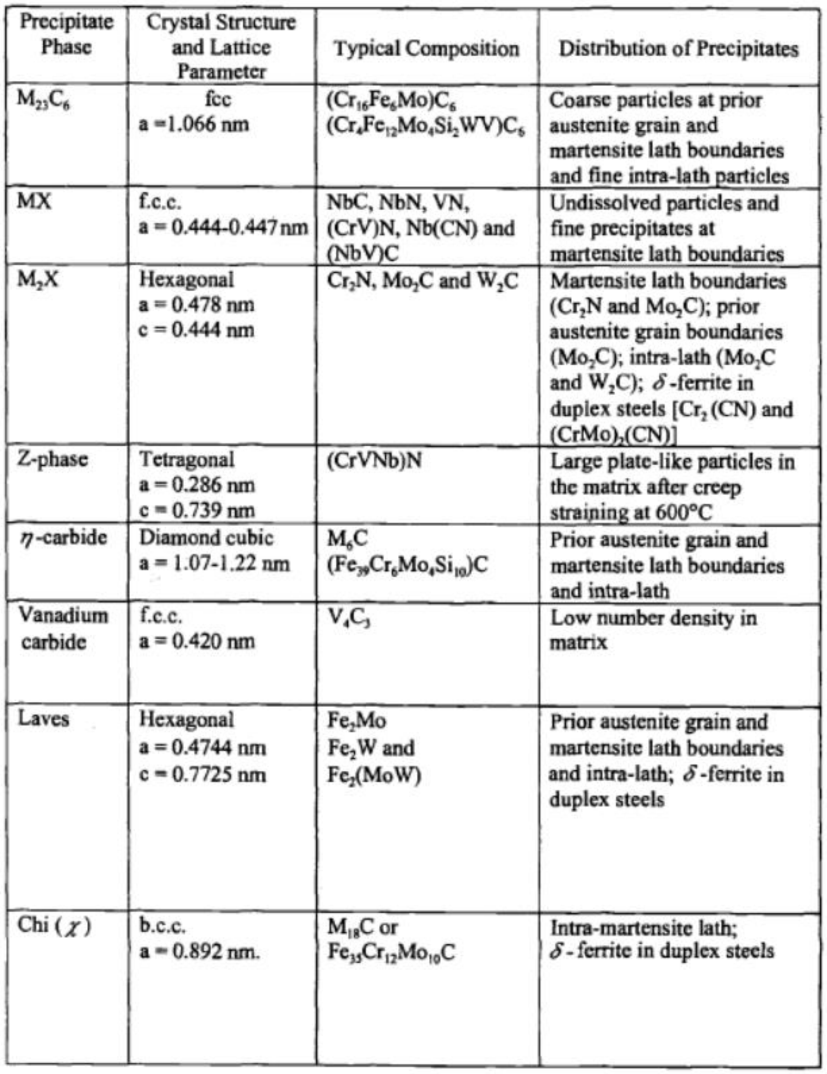

Precipitate Phase	Crystal Structure and Lattice Parameter	Typical Composition	Distribution of Precipitates
$M_{23}C_6$	fcc a =1.066 nm	$(Cr_{16}Fe_6Mo)C_6$ $(Cr_4Fe_{12}Mo_4Si_2WV)C_6$	Coarse particles at prior austenite grain and martensite lath boundaries and fine intra-lath particles
MX	f.c.c. a = 0.444-0.447nm	NbC, NbN, VN, (CrV)N, Nb(CN) and (NbV)C	Undissolved particles and fine precipitates at martensite lath boundaries
M_2X	Hexagonal a = 0.478 nm c = 0.444 nm	Cr_2N, Mo_2C and W_2C	Martensite lath boundaries (Cr_2N and Mo_2C); prior austenite grain boundaries (Mo_2C); intra-lath (Mo_2C and W_2C); δ-ferrite in duplex steels [$Cr_2(CN)$ and $(CrMo)_2(CN)$]
Z-phase	Tetragonal a = 0.286 nm c = 0.739 nm	(CrVNb)N	Large plate-like particles in the matrix after creep straining at 600°C
η-carbide	Diamond cubic a = 1.07-1.22 nm	M_6C $(Fe_{39}Cr_6Mo_4Si_{10})C$	Prior austenite grain and martensite lath boundaries and intra-lath
Vanadium carbide	f.c.c. a = 0.420 nm	V_4C_3	Low number density in matrix
Laves	Hexagonal a = 0.4744 nm c = 0.7725 nm	Fe_2Mo Fe_2W and $Fe_2(MoW)$	Prior austenite grain and martensite lath boundaries and intra-lath; δ-ferrite in duplex steels
Chi (χ)	b.c.c. a = 0.892 nm.	$M_{18}C$ or $Fe_{35}Cr_{12}Mo_{10}C$	Intra-martensite lath; δ-ferrite in duplex steels

Figure 2.20. Precipitation phases observed in tempered, aged, and creep-ruptured tested F/M Steels[54].

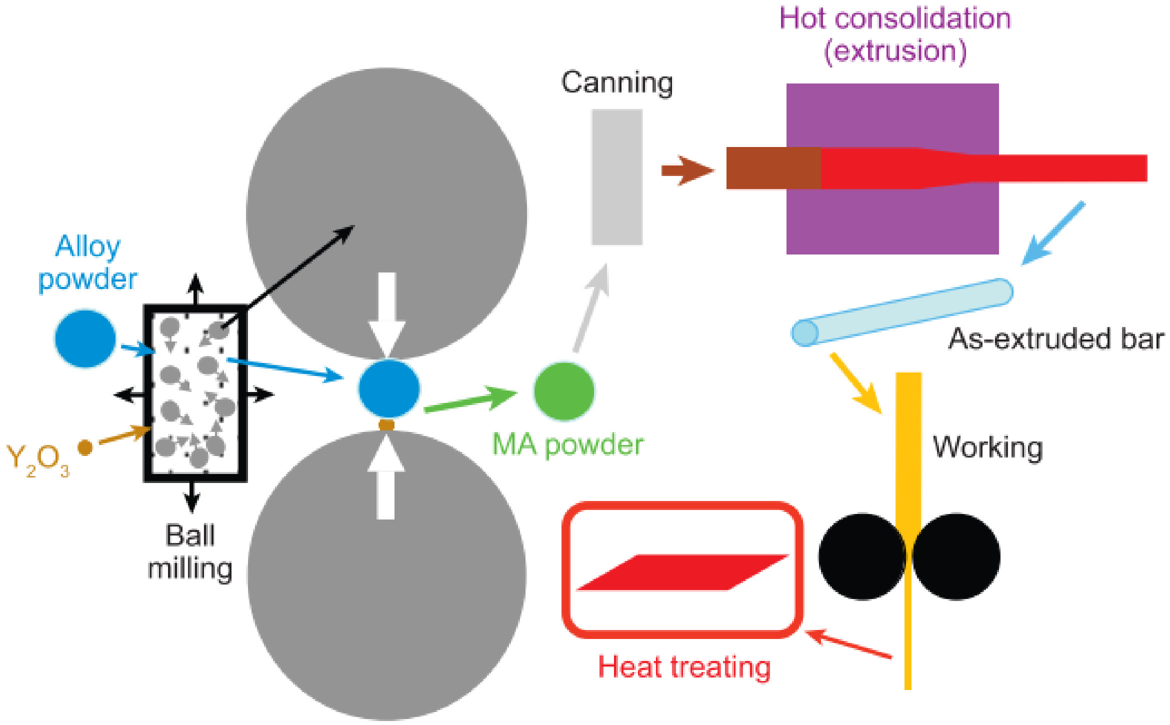

Figure 2.21. A schematic of the ODS steel manufacturing process[11].

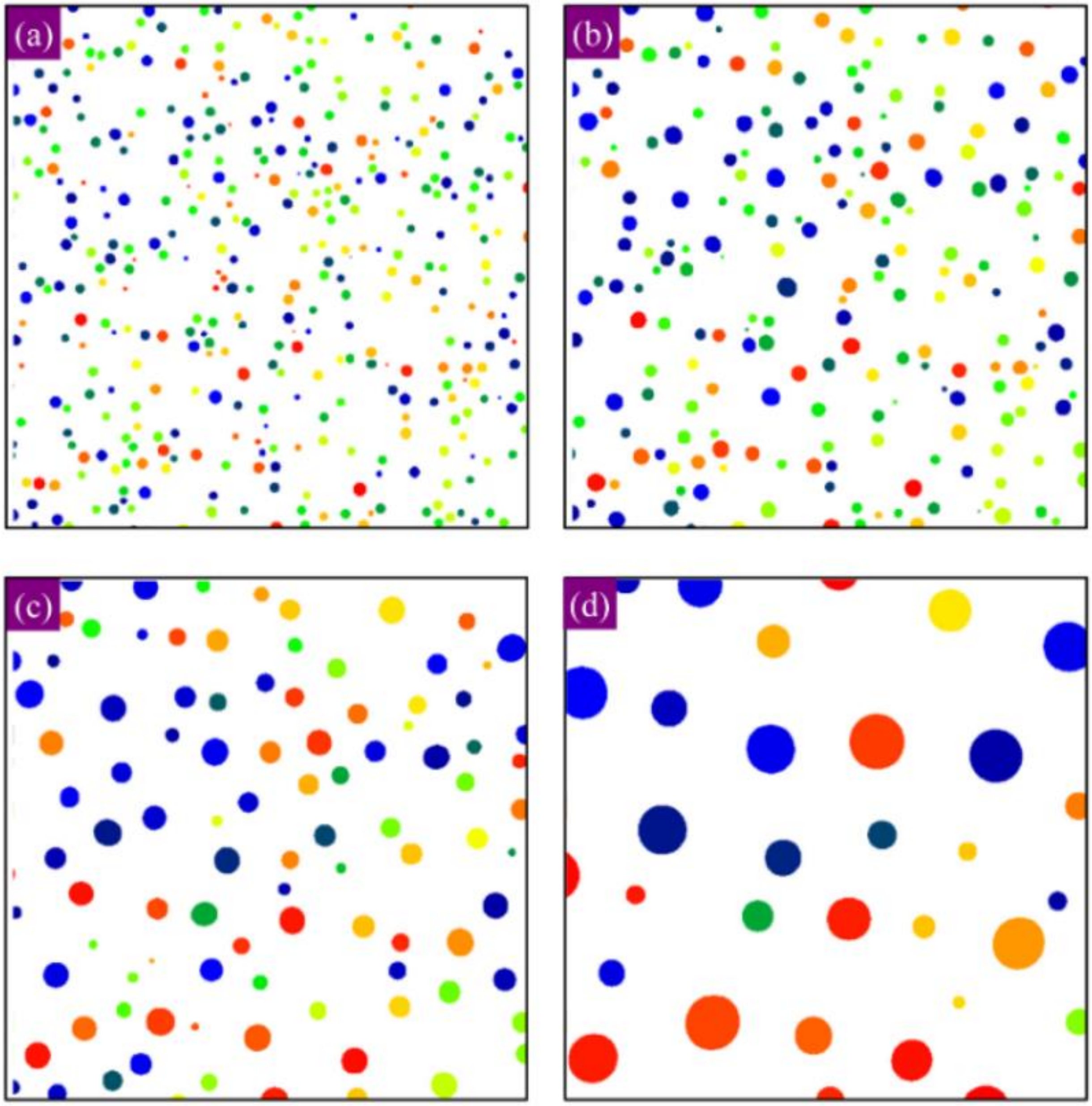

Figure 2.22. The microstructural evolution of Ostwald ripening over a time period. (a) to (d) are over larger time periods[63].

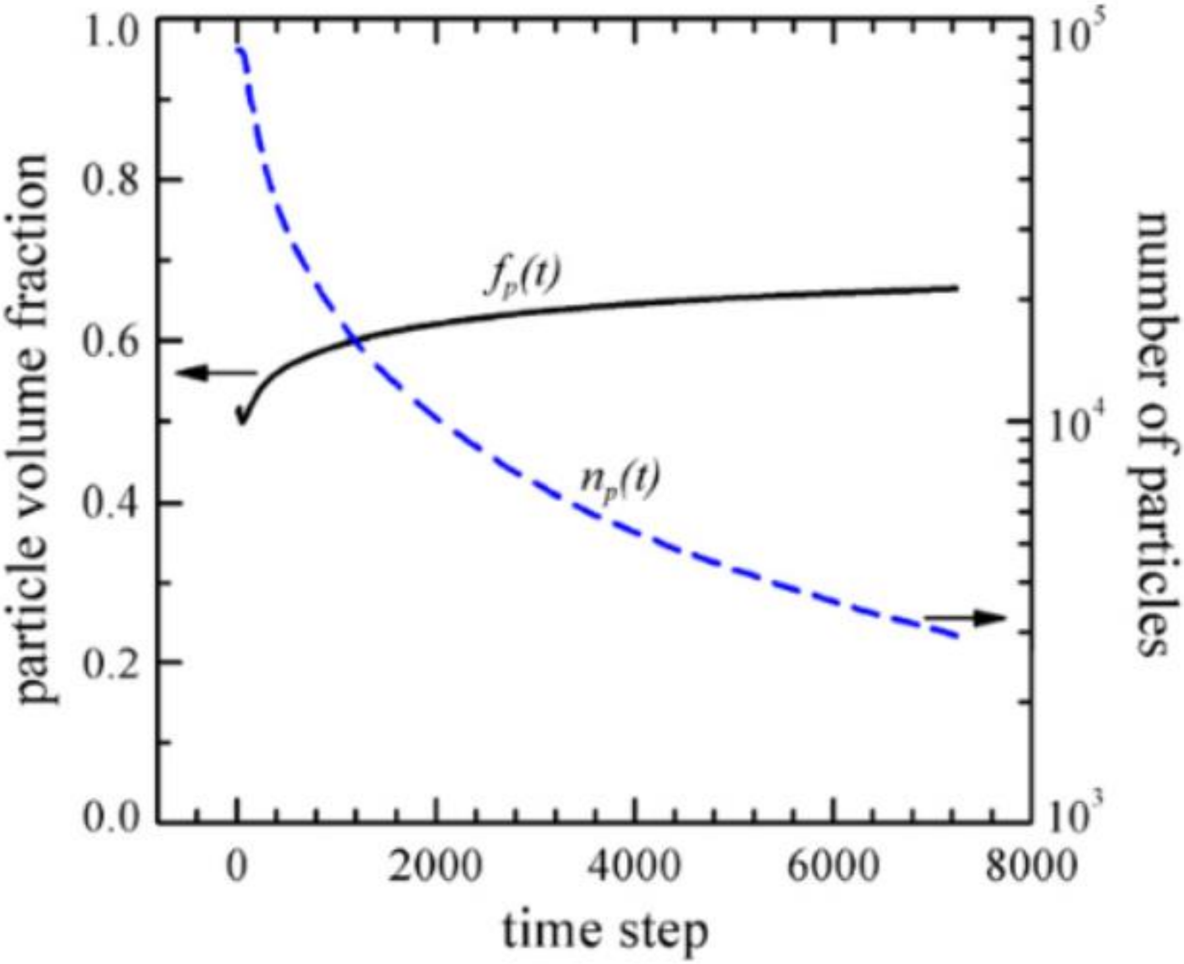

Figure 2.23. The evolution of the volume fraction is in black and the number of particles is shown in blue[65].

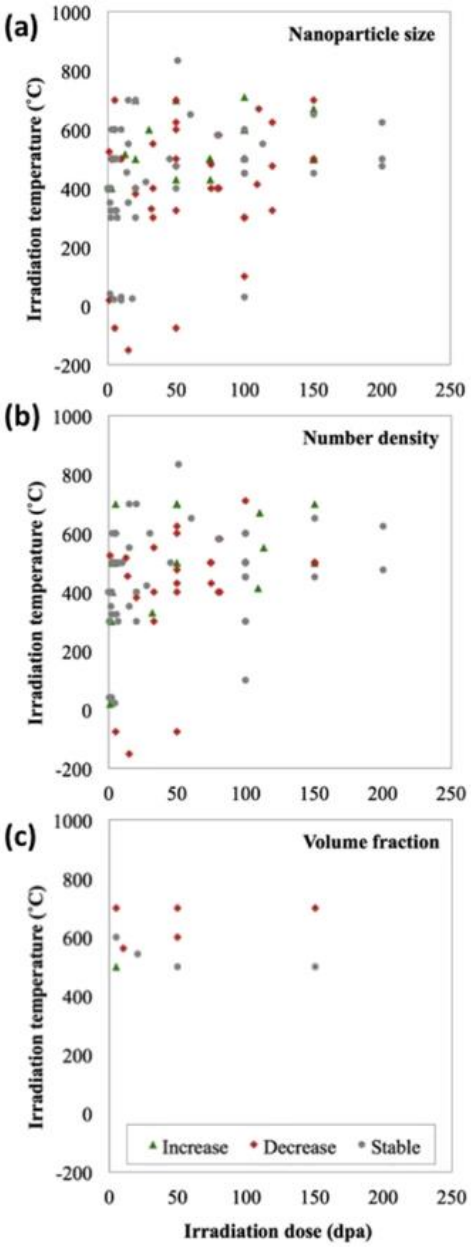

Figure 2.24. The evolution of a) Nanoparticle size, b) Number density, and c) volume fraction at various temperature and irradiation dose (dpa)[71].

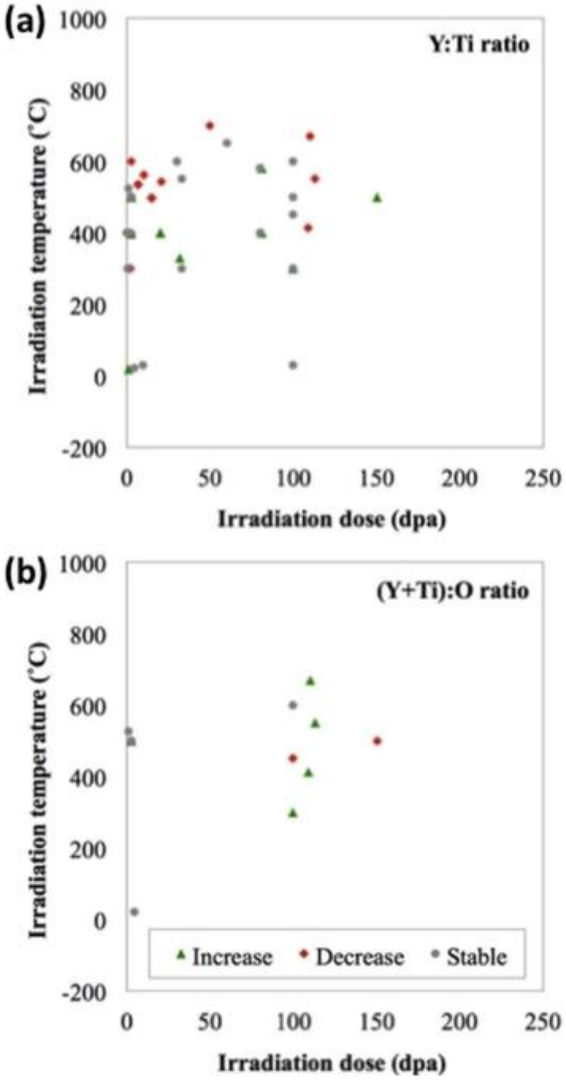

Figure 2.25. The evolution of a) Y:Ti ratio and b) the change in metal to oxide ratio[71].

Chapter 3 - Objective

The objective of this dissertation is to further understand the effects nanoclusters (NCs) have on the strength and irradiation resistance of oxide dispersion-strengthened (ODS) steels. In accomplishing this feat, two major areas of the effect of NCs have on a base Fe NC are investigated: the first looks at the effect NCs have on the primary cascade damage state using molecular dynamics (MD), and the second will look at the interactions between dislocations, both edge and screw, and NCs to see how NCs increase the strength of the pure bcc Fe matrix. This thesis looks at different NC diameters and temperatures; to see how these two key aspects affect the overall strength of ODS steels.

The structure of a NC and the interaction between the NC and the Fe matrix are an important part of ODS steel. High resolution transmission electron microscopy has greatly aided in understanding the structure of smaller NCs; however, small NCs are still too small to be truly understood via the standard experimental techniques, hence the structure at very small sizes is less understood. MD allows the structure to be investigated and viewed. In this study only one variable is changed:

- *NC Diameter:* The NC diameter is changed from 1 nm to 12 nm.

In investigating the irradiation resistance of a material, MD has greatly improved the understanding in how the primary damage state of a cascade evolves. In literature many studies have looked at the effect of a primary damage state of a pure metal[14–16,25]; however, only recently have studies started to look at defect structures within a material i.e. dislocations and voids[30,34–36]. In understanding the primary damage state of a cascade near and within a NC, the evolution of damage for a NC may tell the precursors to explain the long term structure changes within NCs in ODS steels. The following variables are controlled during the cascade simulations.

- *Box Temperature:* Temperature has been shown to play a key role in the experimental evolution of NCs, by comparing 100K, 300K, and 600K understanding the primary damage state of a cascade will be further understood for 3 different temperatures.
- *Primary Knock-on Atom (PKA) Energy:* The PKA energy effect on the damage in the Fe matrix and the NC will be investigated to understand how different PKA energies interact with the NC. PKA energies of 1 keV, 5 keV, and 10 keV are to be investigated.
- *NC Diameter:* As the ideal NC diameter has tended towards a smaller size, the effect of NC diameter on the evolution of the primary damage state needs to be investigated. Diameters of 2 nm, 4 nm, and 6 nm are to be investigated.

The next major area of research is into the effect NC diameter has on the strength of ODS steel. The inclusion of NCs within ODS steel greatly increase the yield strength and creep rupture strength compared to a standard ferritic-martensitic (F/M) steel. The effect of NC size and temperature are to be investigated the following parameters are controlled:

- *Dislocation Type:* Two types of dislocations in BCC iron are investigated. The first is the ½ <111> {112} edge dislocation and the second is the {110} plane screw dislocation.
- *NC Diameter:* The effect NC diameter has on the α value on the material are investigated. The diameters modelled are: 2 nm, 4 nm, 6 nm, 8 nm. And 10 nm.
- *Temperature:* The temperatures looked at are 300 K and 600 K.

Chapter 4 - Nanocluster Structure Simulations

Ferritic-martensitic (F/M) steels show great resistance to irradiation-induced void swelling, higher thermal conductivity and lower thermal expansion than austenitic steels [95]. The strength and swelling resistance of F/M steels can be significantly improved by adding a fine dispersion of various Y_2O_3 oxides [96], the inclusion of these oxides creates a new class of steel, oxide dispersion strengthened (ODS) steels. Generally, ODS alloys are fabricated by mixing Y_2O_3 particles with a Fe-Cr alloy through ball milling [11]. The resulting material tends to have fine grains, high dislocation density, and a high density of ultrafine nanoclusters (NCs). These NCs have a wide variety in size, but the NCs of interest are the particles between the size of 1-5 nm, NCs (NCs), which are believed to play the major role in strengthening the base alloy [97,98]. The F/M based ODS steels are considered promising candidate materials for first wall/blanket applications in a fusion reactor [97] and promising materials for future fission reactor structural materials. In addition, NCs may act as sinks for vacancy/interstitial recombination, enable nuclear sites for helium bubbles and act as dislocation obstacles [76,85,99–101].

The structure and chemical composition of these NCs has been investigated using many experimental methods: atom probe tomography (APT), transmission electron microscopy (TEM), electron energy loss spectroscopy (EELS), and energy dispersive xray (EDX) [102–105]. TEM characterization has been used to study NCs of Y_2O_3 cubic structure, $Y_2Ti_2O_7$ pyrochlore structure, and Y_2TiO_5 orthorhombic structure [100,103,106], whereas APT results have shown a chemical composition of high Ti/Y ratio and a low O/(Ti+Y) ratio and suggested that NCs are highly non-stoichiometric and coherent with the matrix [104,107,108]. Based on the evidence from TEM and APT results [103,107], a core-shell model for oxide NCs with a Y-rich core and solute-rich shell has been proposed. Although these studies provided the detailed segregation of the chemical species in the oxide NCs, atomic scale details of NC's structure is still not fully understood.

Computer simulations are corroborated with TEM observations to understand the detailed structures of Y_2O_3 in Fe. Density functional theory and Monte Carlo methods have been previously used to model the formation and growth of these NCs, during mechanical alloying (MA) and after consolidation, [12,109–112]. TEM is a functional tool and widely used in characterizing tiny features such as Y_2O_3 NCs in materials. However, the finest features (smaller than 1 nm), such as core-shell structures in very fine NCs, are very hard to observe by TEM because of the interference from matrix and the limiting microscope resolution. However, MD is a powerful tool in modeling the structures of these clusters at the end of production, i.e. following the ball milling and consolidation technique. The goal of the section is to get a better understanding of the Y_2O_3 NCs, and the computational results are compared with TEM examinations for validation.

4.1 Nanocluster Structure Simulation Setup

In the case of the nanocluster structure simulations, the following software and codes are paramount. The simulation are carried out using the large-scale atomic/molecular massively parallel simulator (LAMMPS) program [17]. Ovito software is used to visualize the data and determine the structure [18], and VMD is used to determine atom counts [113]. All of the simulations in this chapter use periodic boundaries along all three directions.

Prior to testing the structure of Y_2O_3 NCs, the potential used in this chapter are tested at determining the structure of a pure bcc Fe and pure cubic $Y_2O_{3.}$ The interactions between atoms are described using the Buckingham potential [114]. The lattice constant, of a pure α-Fe is first tested. A box of 20 x 20 x 20 lattice units, 16 000 atoms, is setup to determine key parameters of the Fe lattice based on the Hammond potential. In these simulations, the lattice constant is obtained for pure α-Fe as 0.2855 nm, is in good agreement with DFT calculations [114]. Further details on the interatomic potential used in these simulations can be found in reference [114]. Figure 4.1 shows plots of the interatomic potentials used in the structure simulations, based on the Hammond potential. For this study, the Hammond interatomic potential is modified to include the charges for the Y and O atoms. By adding the charges, the Y_2O_3 particles tend to be more stable because the charge hinders the movement of the O atoms.

Y_2O_3 has a cubic structure with space group Ia-3 [115]. The Y atoms occupy the 8(b) sites and 24(d) sites and the O atoms are located on the 48(e) general sites. Experimental Y_2O_3 has a lattice constant of 1.06 nm [115]. Figure 4.2 shows the standard cubic Y_2O_3 structure. In testing the Y_2O_3 structure, the interatomic potential used in this study underestimated the lattice parameter and the most stable structure occurred with a lattice constant of 0.95 nm. Due to the complexity of O atoms, it is nearly impossible to model O-O relation perfectly using a pairwise function; however, the overall trends for the system are not affected greatly because of the overall small percent of O in the system [114].

The stability of Y_2O_3 is tested in a box of size 10 x 10 x 10 unit cells, with a total of 80,000 atoms by relaxing the system, raising the temperature to 600 K for 15 ps, and then quenching to 0 K with the NVT canonical ensemble. Common neighbor analysis and coordination approach are applied to help determine the Y_2O_3 structure for comparison to the NC system. The built in common neighbor analysis and coordination approaches in Ovito are used to determine these attributes of the Y_2O_3 system. The common neighbor analysis on the Y atoms suggested a fcc structure of Y_2O_3 and the radial distribution function for pure Y_2O_3 is used to compare to the Y_2O_3 NC in the Fe system.

The stability and configuration of the Y_2O_3 NCs are simulated. An Y_2O_3 spherical NC is placed at the center of an iron matrix, computational cell. For small Y_2O_3 NCs (1-6 nm in diameter) a MD block with 40 x 40 x 40 unit cells (containing ~ 128 000 atoms) is used, but for the larger clusters (greater than 5 nm) a block with 64 x 64 x 64 unit cells (containing ~ 525 000 atoms) is used. Table 4.1 lists a summary of the key box characteristics for each NC study used in these structure simulations. The computational cells are relaxed using the conjugant gradient method and then raised to a temperature of 600 K for 15 ps, with a time step of 0.001 ps, within the NVT (constant atoms, volume and temperature) canonical ensemble, in order to identify the minimum energy configuration of the Y_2O_3 NCs.

A 12 nm NC diameter is used as the cut off in this dissertation as that is the cutoff where researchers have showed that Y_2O_3 NCs moves from a spherical structure to a faceted one with the Fe matrix [102]. In order to keep charge neutrality of the system, several Y or O atoms near the Fe-cluster interface are removed from the system, which is dependent of its size. For the NCs, the system is first relaxed using the conjugate gradient algorithm, followed by a structure annealing at 600 K and then quenched back to 0 K. For the 3, 5, 6 and 8 nm NCs are annealed at a higher temperature to see the affect temperature has on the structure. The higher temperature simulations consist of an energy minimization using the conjugate gradient algorithm, followed by a structure annealing at 1173 K, and then quenched to 0.015 K. For the larger cluster sizes the system is just relaxed, based on no significant changes in the smaller cluster systems during structure annealing and quenching back to 0.015 K.

4.2 Nanocluster Structure Simulation Results

The results obtained from MD are compared to experimental results looking at a ODS steel with Y_2O_3 NCs. The material fabrication and some of the basic properties for the ODS steel used in comparison are quickly described below. TEM observation is conducted on a 9Cr-ODS alloy with a nominal composition of Fe–9Cr–1.5W–0.4Mn–0.1Ta–0.2V–0.3Y_2O_3 (mass %). 9Cr-ODS alloy is prepared by MA in a planetary high-energy ball mill at room temperature for 50 h in an argon-gas atmosphere. The ball-to-powder weight ratio was 10:1. Followed by hot isostatic pressing, the samples ran at 1373 K under a pressure of 200 MPa for 2 h. TEM samples were prepared by focused ion beam (FIB) lift-out method on the mechanical polished raw 9Cr-ODS alloy, using FEI Helios Nanolab Dualbeam workstation. Scanning TEM (STEM) is employed to characterize the structure of NCs of Y_2O_3 using a double Cs-Corrected STEM (JEOL 3100R05) operated at 300 keV.

Common neighbor analysis via the Ovito software is used to determine the structure of the Y_2O_3 NCs; the crystal structure of the NC consists of a spherical Y_2O_3 structured region surrounded by a disordered region in which the Y and O atoms cannot be identified to as part of a particular crystal structure. For the clusters below 2 nm, the entire NCs are disordered. For the Y_2O_3 clusters between the sizes of 2 nm and 12 nm, the relaxed atomic configurations of Y_2O_3 NCs consist of a structured core of cubic Y_2O_3 surrounded by a disordered region. Both the disordered and structured regions have near stoichiometric Y_2O_3, but the disordered region separates the structured core from the Fe matrix, thus forming a core-shell structure.

The NCs have short-range order within the cluster without forming an atypical crystal structure. Figure 4.3(a) shows a cross section of a 2 nm cluster in Fe matrix, along with the radial distribution of the atoms within NC. Both the atomic configuration and the radial distribution indicate that the entire NC is disordered without a crystalline structure. The radial distribution consists of only a single major peak, and shows the typical systems without periodicity and a liquid-like structure. Figure 4.3(b) shows an image of a 5 nm cluster (the cross section, and the radial distribution of the structured region, where the inset in the right corner shows the atomic arrangement of the Y_2O_3 shell and its corresponding radial distribution). The center of the NC has a cubic Y_2O_3 structure, and the radial distribution peaks occur at the same places compared to the pure Y_2O_3 system. Within the shell, the radial distribution is similar to that shown in figure 4.3(a) with a single major peak, and the atoms in the shell also appear to be disordered.

Table 4.1. A summary of the box information for the structure simulations.

Y_2O_3 diameter (nm)	Atoms in NC	Dimensions in lattice spacing	L (Å)	Total Number of Fe Atoms	Temperature (K)
1	70	40 x 40 x 40	114.2	127 935	600 → 0.015
2	395	40 x 40 x 40	114.2	127 661	600 → 0.015
3	1 300	40 x 40 x 40	114.2	126 757	600 → 0.015
4	3 130	40 x 40 x 40	114.2	125 109	600 → 0.015
5	3 660	40 x 40 x 40	114.2	122 399	600 → 0.015
6	10 630	40 x 40 x 40	114.2	118 279	600 → 0.015
8	25 360	64 x 64 x 64	182.7	501 239	600 → 0.015
10	29 727	64 x 64 x 64	182.7	473 792	600 → 0.015
12	85 670	64 x 64 x 64	182.7	446 353	600 → 0.015

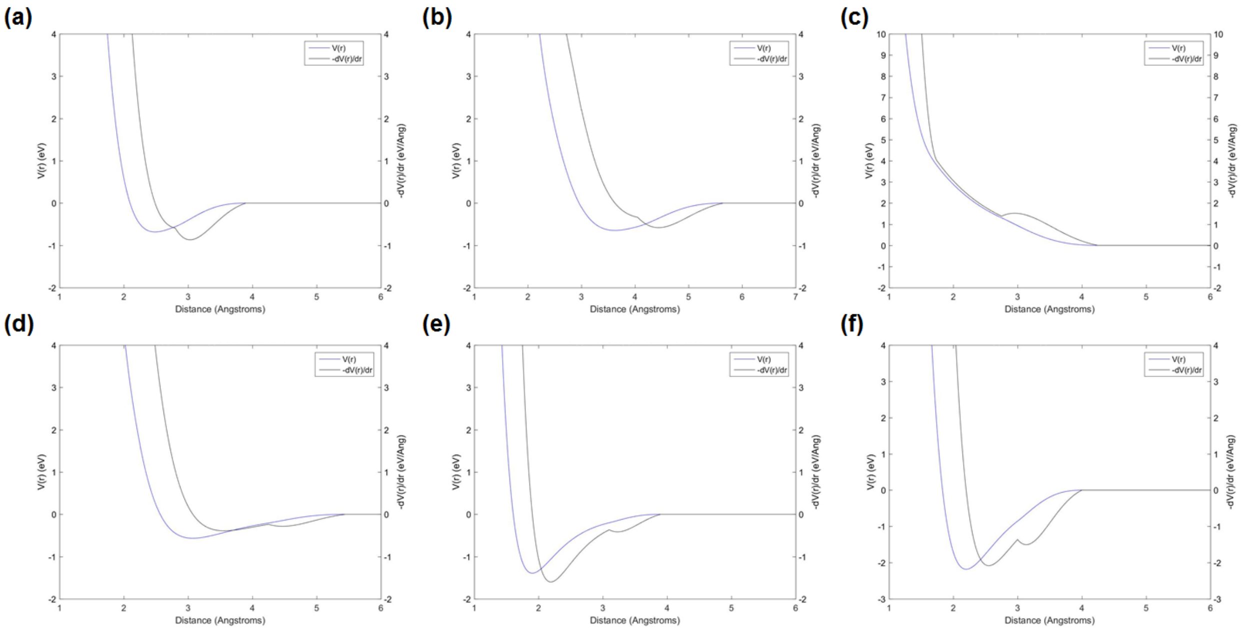

Figure 4.1. The Buckingham Potential Files plotted based on the Hammond Model[114]: (a) Fe-Fe Potential, (b) Y-Y Potential, (c) O-O Potential, (d) Fe-Y Potential, (e) Fe-O Potential, and (f) Y-O Potential.

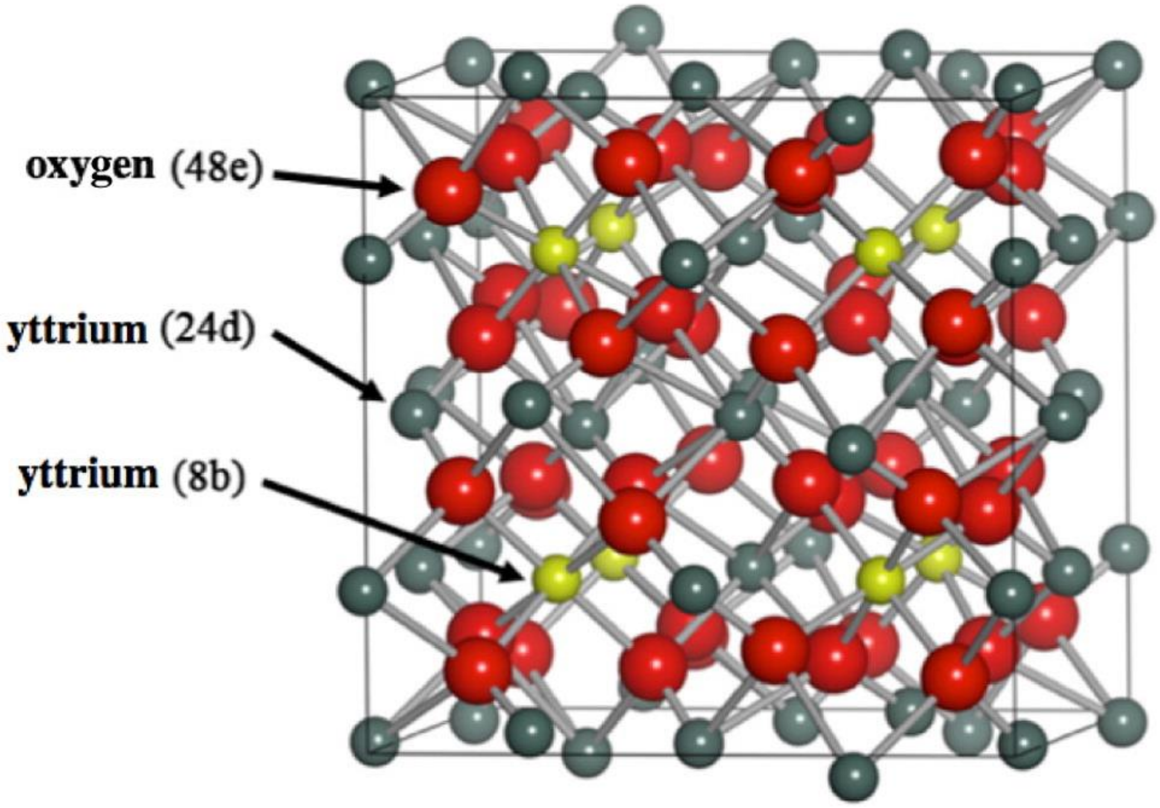

Figure 4.2.The cubic C-type Y_2O_3 (bixbyite) structure[116].

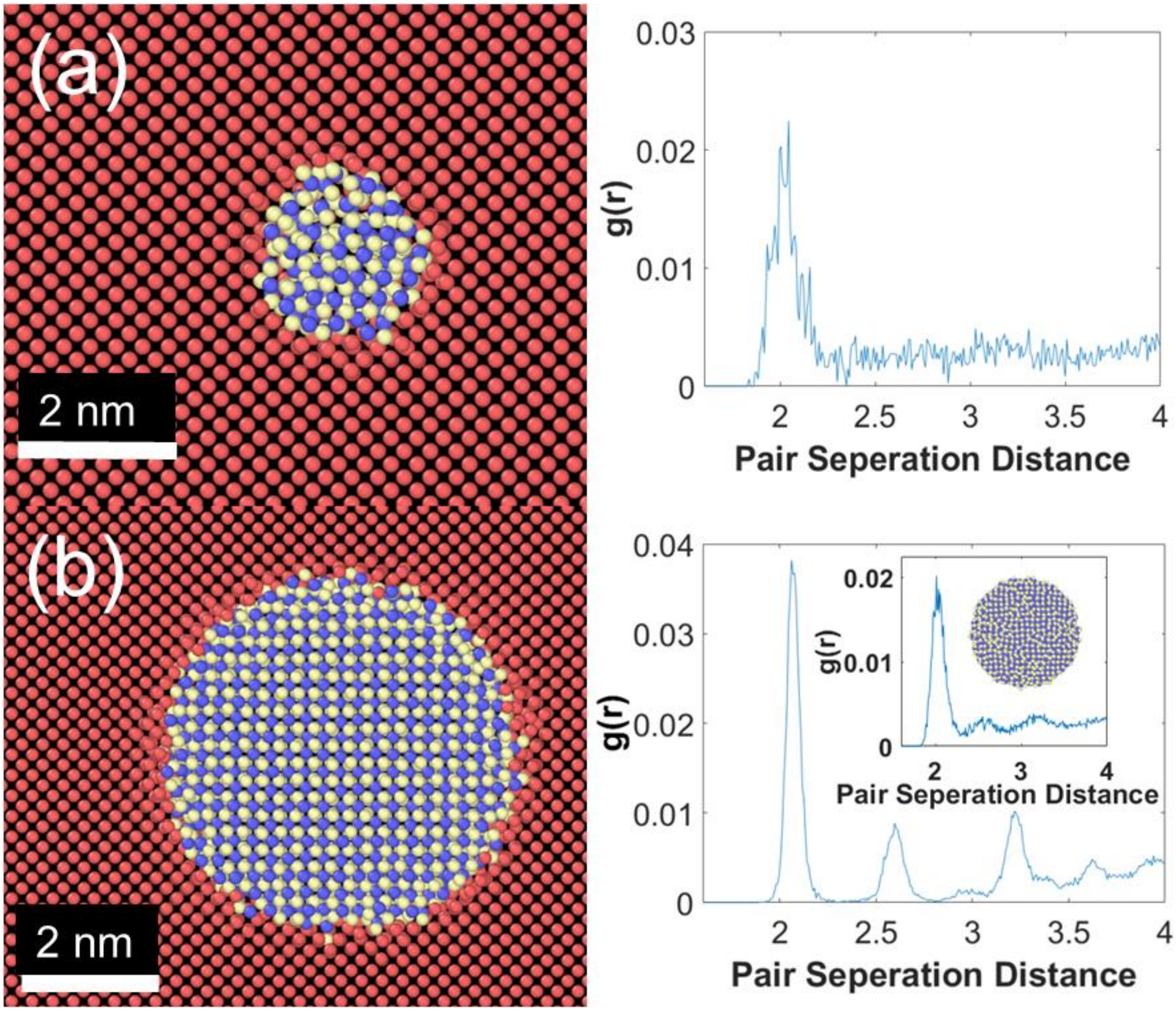

Figure 4.3.In images (a) and (b), the red atoms are the Fe atoms, the blue atoms are Y, and the yellow atoms are O. (a) shows a cross section of the 2 nm cluster along with the radial distribution function. (b) shows a cross section of the 5 nm cluster along with the radial distribution function of the structured core, where the insert exhibits the atomic arrangement and the radial distribution function of the disordered shell[117].

Chapter 5 - Cascades in the Iron-Nanocluster System

Next generation reactors require higher irradiation tolerant structural materials for more corrosive environments and higher temperatures. One of the popular candidate materials is oxide dispersion-strengthened (ODS) steels. ODS steels have been proposed as duct, cladding, and structural materials for fission reactors and as a material for the first wall and a blanket material in fusion reactors[20,106,118]. There have been many experimental studies on the benefits of nanostructured ferritic alloys (NFAs). Several review papers on NFAs have shown that these materials have high yield strength, and high irradiation resistance[11,97]. NFAs high irradiation resistance is due to nanoclusters (NCs) acting as successful sites in trapping defects and NCs ability to act as a site for recombination[11,97].

Although ODS steels, in theory, should have excellent irradiation resistance, ion irradiation experiments have shown conflicting results. A recent review paper published by Wharry summarized the inconsistent experimental results from ion and neutron irradiation experiments on ODS steels[13]. Depending on the material composition, consolidation and heat treatment performed, and the type of ion used for the irradiation, the results of the experiments varied greatly, with reports published stating opposite trends are occurring in these NFAs[13].

The irradiation stability of NCs is a major area of experimental research. As the NCs are one of the key factors in the strengthening of ODS steels, these materials have advantageous irradiation resistance properties for next generation reactors. The major ways of tracking the irradiation stability of NCs are in studying the evolution of the diameter, size distribution, number density, volume fraction, the chemistry of these NCs, and the changes to the surrounding crystal structure as a function of dpa[13]. Prior to irradiation, it has been shown, both experimentally and computationally, that NCs tend to be stable within the Fe matrix[104,108,117,119]. After irradiation, irregularities have been observed in the NCs; atom probe topography (APT) is used to corroborate the dissolution of Y_2O_3 NCs, along with NCs composition changing heavily after irradiation[120]. Other experiments have shown an increase in the irregularities between the Fe-matrix and NC interface[87,121]. Fundamental computer simulations play a key role in furthering the understanding of the irradiation evolution of ODS NCs.

Density Functional Theory (DFT) calculations have been used to understand the effects elements have on the formation and structure of NCs[109,122]. Along with DFT calculations, higher order simulations, such as thermodynamic and kinetic Monte Carlo models, have shown the evolution of NCs during the heat treatment common in ODS steel manufacturing[12,123]. All of these studies have advanced the understanding on the formation of NCs in ODS steels. In furthering the understanding of the primary damage state of cascades in NCs, studies have focused on pure Y_2O_3 damage, and the effect of an embedded NC has on the damage evolution in an Fe matrix at very low energies[124].

Molecular Dynamics (MD) has been the main tool for looking at the primary damage state of displacement cascades[14,21,24,25]. In this dissertation, MD is employed to understand defect generation, damage morphology, radiation resistance and enhanced defect recombination in ODS steels for NCs with various radii, a range of primary knock-on atom (PKA) energies, and temperatures. The simulations with various PKA energies provide significant insights into the relative stability of ODS steel NCs and their evolution within a displacement shockwave. Using MD to analyze the effects of displacement cascades on Y_2O_3 NCs furthers the understanding of the primary damage state of NCs, along with the surrounding α-Fe matrix in ODS steels and plays a key role in furthering the understanding of the irradiation properties of NCs and ODS steels.

5.1 Cascade Simulation Setup

The key codes and software used in modelling cascade simulations is large-scale atomic/molecular massively parallel simulator (LAMMPS) and Ovito is used to visualize and analyze the LAMMPS dump files [17]

All interactions between atoms are governed by an empirical potential in MD simulations. The interatomic potential describing all of the interactions for the Y and O atoms in the simulations is developed by Hammond as is used in Chapter 4, and uses the form suggested by Buckingham[114]. The Buckingham form uses a Born-Mayer potential to represent the Pauli repulsion of electron clouds at close distances coupled with a long range attraction term. The Born-Mayer potential is successful at modeling the equilibrium state of the structure; however, non-ideal for non-equilibrium situations common in primary cascade simulations. To remedy this issue, a universal repulsive potential of the form, Ziegler, Biersack, and Littmark (ZBL) formula, is used to better model these non-equilibrium conditions. The ZBL potential and the Born-Mayer potential are connected via a polynomial equation; the basic setup is shown in equation 4.1. More information on the specific cutoffs for each atom pair and the dE term, a term to connect the two different potentials, can be found in Hammond's paper[114]. The Fe potential used for the cascade simulations is an embedded atom model potential developed by Marinica, which is shown to agree with experimental results and DFT calculations. The potentials have been previously employed to model the irradiation properties of α-Fe[27].

$$V(r) = \begin{cases} V_{ZBL}(r) + dE & r \leq r_1 \\ \sum_{n=0}^{5} s_n r^n & r \in (r_1, r_2) \\ V_{Buckingham}(r) f_{cut}(r) & r \geq r_2 \end{cases} \qquad \text{(Eq. 4.1)}$$

The details for setting up a Y_2O_3 NC in a Fe matrix are described in Chapter 4, and only the central principles are described here. Initially, a Y_2O_3 NC is placed at the center of a Fe matrix, and the system is relaxed using the conjugant gradient method to release the accumulated stress. Then, the systems' temperatures are raised to 600 K and equilibrated for 15 ps with the NVT (constant atoms, volume, and temperature) canonical ensemble, thus, achieving the minimum energy configuration of the Y_2O_3 NCs. The cascade simulations take place at a temperature of 100 K, 300 K and 600 K with the system being equilibrated over 50 000 time steps for a total time of 50 ps to achieve an equilibrium state of the phonons at each temperature of interest. 3 Temperatures are investigated in the primary damage state of a cascade near a NC. The three temperatures allow the effect of the NC and the effect of defect mobility to be better separated and thus a better understanding of the improvements of NC inclusion has on the irradiation resistance of ODS steel. At higher temperatures the key difference in a standard metal matrix is that there is a slight increase in the number of Frenkel pairs during the peak damage state. However the amount of time required to reach the final population of Frenkel pairs increases in time with increasing temperature[14,24,25].

Following the equilibration of the system, it is now time to insert the kinetic energy into the system. A python script is utilized to determine Fe atoms that are 1.5 nm away from the outer shell of the NC. From that list of atoms, the PKAs are chosen. These atoms are given a velocity towards the center of the NC, .i.e. the position of the PKA is used in defining the velocity in x, y , and z directions. Figure 5.1 shows the standard setup, prior to the PKA receiving the additional kinetic energy. These simulations are computationally expensive due to the necessarily small-time steps taken so that the relatively high change in energy of the system is maintained and no atoms are lost. In the simulations, an adaptive time step is required.

An adaptive time step is a tool within LAMMPS to better control the size of timesteps based on a set of user given parameters. In the case of cascade simulations, the high transfer of energy via the PKA dispersing energy to the surrounding matrix is the key factor needed to be controlled. To ensure no atoms are lost, the following limiting factors are set: 10^{-8} to 10^{-3} ps time limit and a max distance traveled of 8 to 2 pm, decreasing with increasing PKA energy. A strict adaptive limit is set for the first ps of each simulation, as this is the point where most of the energy is being dispersed and after the peak energy transfer from the PKA to the box, the adaptive limit is loosened to allow shorter run times for the remainder of the cascade simulation. The max distance is increased to 8 pm for all simulation cases after the first ps; the simulations are halted at a simulation time of at least 20 ps, when the damage state is at the final equilibrium.

Through the use of an adaptive time step, the simulation is able to run smoothly over the entire run time, and also decreases the run time, while preserving accuracy. All simulations are carried out for a fixed volume and fixed number of atoms, with a periodic boundary condition along the three dimensions. A proper MD-cell size is chosen so as to avoid overlap of the displacement cascade with itself due to the periodic boundary conditions. For a displacement cascade with a 10 keV kinetic energy PKA, a crystal of ~250 000 atoms (50x50x50 Fe unit cells) for the 2 nm and 4 nm NC systems and a crystal of ~430 000 (60x60x60 Fe unit cells) for the 6 nm NC system are employed for these simulation. Table 5.1 gives a quick rundown of the key box information for the cascade simulations in this dissertation.

In terms of analyzing the results of the cascade, Ovito is a powerful tool in tracking the defects created during a cascade. In general, Wigner-Seitz is often used in tracking the number of point defects within the primary damage state of a cascade in MD. Wigner-Seitz defect analysis consists of comparing the location of atoms between two images, the first is the image at time zero of the PKA simulation, following equilibration, and the images as the PKA transfers energy to the system. By comparing the α-Fe NC system as the PKA transfers energy to the perfect system, post-equilibration, the interstitials, antisites and vacancies are recorded based on the differences between the two images. Ovito is a useful tool in analyzing the dump files outputted by LAMMPS. The Wigner-Seitz subroutine within the Ovito software is used in these simulations, along with some python post analysis scripts to analyze the location of point defects. The clustering analysis tool within Ovito is used to look at the clustering surrounding the NC. Ovito is also used to illustrate the simulation box, and give a visual track the formation of defects and defect clusters in the system[18].

The key way to track and understand the damage state of a cascade is in looking at the number of defects within the system: vacancies, interstitials, and antisites. A vacancy is defined as an empty lattice site. Interstitials are lattice sites that have more than 1 atom. Antisites are a sub-class of interstitials. Antisites are a type of defect that occurs in more than 1 atom type systems, where an atom will sit on another atom type's lattice site. In the cascade simulations, the key antisites of interest are the Fe atoms on the O and Y lattice sites.

5.2 Cascade Simulation Results

In chapter 4 of this dissertation, it is shown that for small diameter NCs, less than 2 nm, the preferential structure of Y_2O_3 is a disordered structure and with increasing diameter, the NCs formed a core-shell structure in the Fe matrix[117]. Y_2O_3 NC core has the standard cubic Y_2O_3 structure, bixbyite type[115], surrounded by a shell of amorphous Y and O atoms. Surrounding the NC, the Fe atoms are displaced from their lattice sites. A core-shell structure for Y_2O_3 NCs is validated both experimentally and computationally via first principle calculations[103,107,125]. In furthering the understanding of the NC structure, the next step is to understand the effects of NCs on the evolution of the primary damage state of a cascade in the Y_2O_3 NC and surrounding Fe matrix. In this study, a Fe PKA interacts with a NC at various energies, and the results are compared to a perfect bcc Fe system at the same PKA energies.

The small NCs are the focus of this work, as small NCs play a key role in the strength of ODS steels[11,96,97]. Three NC diameters are investigated in the current work: 2 nm, 4 nm, and 6 nm. Three PKA energies are investigated in the current work: 1 keV, 5 keV, and 10 keV for each NC. All of the simulations are run at 3 temperatures: 100 K, 300 K, and 600 K, each temperature helping to further understand the radiation resistance of NCs. The 100 K cases, allow for a better understanding on the effects the inclusion of NCs have on the Fe matrix, by limiting the migration of defects due to temperature. However, the higher temperature cases allow for more atom mobility and are at more practical temperatures for ODS steel. In this research, the irradiation stability and evolution of damage of the Y_2O_3 NCs, along with the effect NCs have on the Fe Frenkel pair evolution in the Fe matrix, are the primary concerns.

Figure 5.2 shows the key regions of interest in this study; the Fe matrix, the atoms directly surrounding the Y_2O_3 NC, and the Y_2O_3 NC itself. The region cutoffs are based on the structure of the atoms. Common neighbor analysis is used to determine the structure of the Fe atoms and the NC atoms. The cutoff where all Fe atoms are bcc is determined as the Fe matrix region, the interface region consists of the Fe atoms which are displaced from the Fe lattice due to interactions with the NC atoms, and then the NC itself. The thickness of the Fe-NC interface region is independent of the NC size, as the thickness of perturbed atoms is independent of NC diameter. The location and clustering of the defects is used to understand the effects of adding a Y_2O_3 NC to the Fe matrix. By combining the information obtained from Wigner-Seitz defect analysis and cluster analysis to compare the number of Frenkel pairs at the peak damage and at the final damage state, after equilibration at the end of the simulation; the effect of adding NCs to primary cascade evolution is further understood.

The results are first discussed in the general trends based on all the temperatures in this study, with the final section in results showing the affect temperature has on the evolution of point defects in the surrounding area and in the NC. The error bars and points in the figures in this chapter are based on the average results, points, over the simulations and the first standard deviation is set as the error bars.

5.2.1 Fe Matrix

Understanding how NCs affects defect evolution in the Fe matrix is an imperative step in understanding the role NCs have in strengthening the irradiation resistance of ODS steel. The first step to explore is how the NCs affect the evolution of the defect populations within the Fe matrix. For low energy (1-10 keV), the primary cascade damage for pure α-Fe has been heavily investigated using MD[14,24,93,126]. Figure 5.3 shows a standard displacement cascade for a 10 keV pure Fe PKA. The PKA interacts with the surrounding atoms, with the damage being dispersed within a single shockwave.

The shockwave consists of an inner sphere of vacancies and an outer shell of interstitials. After the thermal peak, recombination dominates and within a few ps, the system reaches an equilibrium state, with a few remaining Frenkel pairs. In comparison to Figure 5.3, Figure 5.4 shows the evolution of the Fe defects with the inclusion of a NC and a 10 keV PKA for the 2, 4 and 6 nm NCs at 100K. With the inclusion of a NC, the cascade morphology changes significantly with PKA energy. At lower energies, 1 and 5 keV, the NC acts as a cessation point for the cascade, causing a cascade to occur at the NC-Fe boundary. For the 10 keV PKA, a major difference occurs compared to the standard Fe shockwave. At this energy, the PKA is able to penetrate and transfer energy through the NC causing two smaller shockwaves on separate sides of the NC.

The NCs significantly change the damage morphology of cascades within the Fe matrix, via the NC acting as a cessation point for the peak damage state in the Fe matrix or splitting up the shockwave, depending on the PKA energy. At all energies the NC preempts the shockwave and due to the higher coordination number of cubic Y_2O_3 causes the peak damage state to occur at smaller times compared to a pure Fe system. The decrease in time for the peak damage state increases with increasing NC diameter as shown in Figure 5.5. Due to the higher density of atoms, the amount of time required for the energy of the PKA to be dispersed into the system is less.

At low energy, 1 and 5 keV, it shows that the NC preempts the shockwave, causing less damage to be transferred to the Fe matrix. At 10 keV, where the PKA energy is able to transfer through the NC, the decrease is more noticeable for the 4 and 6 nm NC simulations, with the 2 nm NC being the most similar to a pure Fe matrix. Since the shockwave at 10 keV is larger than the 2 nm NC, the 2 nm NC has less of an effect on the shockwave formation within the Fe matrix. Because of the higher coordination number of cubic Y_2O_3 compared to α-Fe, the NCs are able to quickly disperse PKA energy to the system (specifically the NC itself), causing a significant drop in the energy dispersed back into the Fe matrix, and causing the Fe shockwaves to occur and disperse quicker compared to a pure Fe system.

The Fe defect population is broken into two regions based on Figure 5.2, the defects that populated the Fe matrix, and the defects that populated the Fe-NC interface region. Figure 5.6 shows typical cases for the Fe matrix defect evolution for each of the

NC diameters compared to a pure Fe matrix at a PKA energy of 10 keV. The cases chosen are cascade simulations that behaved closest to the average values at both the peak and final defect population for each NC diameter. Figure 5.6 shows that the peak damage within the Fe matrix significantly decreases with increasing NC diameter. However, this significant decrease in Fe defects is less visible in the final number of point defects within the Fe matrix. The vacancy population for the 2 nm and 4 nm NCs are very similar to pure system at 20 ps; whereas, the 6 nm shows a noticeable drop in vacancy population at the end of the simulation. Unlike the vacancy population, the final interstitial population is NC diameter dependent. For the 2 nm case, the population of interstitials is very similar to the pure Fe system. However, in the 4 nm and 6 nm cases there are a large drop in number of defects, with the 4 and 6 nm interstitial populations behaving similarly.

Figure 5.7 shows average results for the point defects at the peak and final damage states, as a function of NC diameter and PKA energy, based on all the cases run. With an increasing NC diameter, there is a fairly significant decrease in the number of interstitials and vacancies at the peak damage state in the Fe matrix. The decrease in Fe matrix peak defect population is also strongly associated with the NC size. As the 2 nm case is the smallest, a key aspect being that the 2 nm is smaller than the cascade shockwave, the PKA energy is easily transferred through the NC, such that the 2 nm diameter most resembles a pure Fe system, having nearly the same amount of point defects at the peak damage state. With increasing diameter, more and more energy is transferred to the NC, causing significant drops in the number of defects at the peak damage state within the Fe matrix. With significant drops in the number of defects at the peak damage state, within the Fe matrix, the final damage state varied with NC diameter.

Figure 5.7 ii.) and iv.) show the NC diameter has a noticeable effect on the number of defects at the end of the simulation, the point where the stable Frenkel pair population is created. The NC has different effects on the interstitials and vacancies. The vacancy population is less effected by the introduction of a NC, with only a slight drop in the final number of vacancies for the 2 and 4 nm NCs and a more noticeable drop for the 6 nm NC. The interstitial population has a more pronounced result. The 2 nm NC is nearly identical to a pure Fe system, whereas both the 4 and 6 nm NCs dropped the final number of point defects to roughly a 1/3 of a pure Fe matrix. The increased vacancy population is likely an effect of the difference in migration energy between the interstitials and the vacancies. With interstitials having significantly lower migration energies, their migration is possible in a MD simulation, whereas vacancies on average migrate on a microsecond timescale making their migration not visible on the MD timescale.

The major takeaway for the inclusion of a NC in the α-Fe system is that there is an energy dependence on the effects NCs have on the Fe matrix defect population. At low energies (1 and 5 keV), the NC acts as a cessation point for the shockwave, in this situation the number of point defects is decreased for both the interstitial and vacancy population. The interstitial population drops more than the vacancy population. At higher energies (10 keV) the effect of NC diameter is more evident. As the 2 nm NC compares greatly to the pure Fe system and the 4 nm and 6 nm with the cascade being broken into two smaller shockwaves resemble a new phenomenon. As the 4 nm and 6 nm NCs have a noticeable drop in interstitials and vacancies. Although at 10 keV, the population of Fe vacancies compared to interstitials within the Fe matrix is higher, likely a result of the mobility of vacancies versus interstitials. During the shockwave, the vacancies occur primarily within the center of the shockwave, with some occurring near the fringes of the shockwave. After the initial wave of recombination with nearby vacancies, some interstitials migrate to the NC.

5.2.2 Fe-Y_2O_3 NC Boundary Y_2O_3 NC

The inclusion of a NC shows a noticeable drop in interstitials and a drop for vacancies, for the larger diameter NCs in the Fe matrix; however, a significant population of interstitials and vacancies forms along the outer shell of the NC after the shockwave and during the cascade relaxation process. As shown in Figure 5.4, the number of defects surrounding the NC or at the interface increases until a saturation number of defects is reached. Figure 5.8 shows how the Fe defect populations directly surrounding the NC evolve over time for a 10 keV PKA based on NC diameter. The interstitials are broken into three smaller groups: pure Fe interstitials, Fe-Y antisites, and Fe-O antisites; where an antisite is defined as an atom sitting on the lattice site of another atom type, in this case Fe on O lattice sites and Fe on Y lattice sites.

Figure 5.9 shows a plot of the number of Frenkel pair defects as a function of the surface area of each NC. With increasing PKA energy, the following trends are evident: a plateau in the number of defects per surface area surrounding the NC is reached for the 2 nm NC, a characteristic of the significantly smaller volume the 2 nm NC has compared to the 4 nm and 6 nm NC diameters. Whereas the 2 nm NC defect population plateaus, the 4 nm and 6 nm NCs show an increasing number of point defects as a function of surface area with increasing PKA energy, fairly linearly for both the vacancy and interstitial populations, with the 4 nm NC having a slightly higher concentration of Fe defects surrounding the NC.

In evaluating the evolution of Fe antisites, the following is very evident: with increasing PKA energy the number of Fe antisites within the NC increases with increasing NC diameter and PKA energy. Figure 5.10 plots the average, final antisite population for the 3 NC diameters in this study, the fraction of Fe interstitials that are characterized as antisites within the NC, and the fraction of NC lattice sites filled with Fe antisites. The PKA energy is able to knock significantly more O atoms off of their lattice sites versus the Y atoms, as expected based on the atomic weights of these two elements. The 2 nm case sees the least amount of change in antisite population, with increasing energy, due to the limited size of the NC, and the energy being able to more easily transfer through the NC back to the Fe matrix. The fraction of interstitials that are antisites follows a similar trend with energy; with the fraction increasing with PKA energy, and NC diameter. With increasing energy, more Fe atoms are able to penetrate and interact with the NC atoms, and with increasing NC diameter the number of NC lattice sites significantly increases, giving the Fe atoms a much higher chance of interaction. The effect of increasing NC radii is shown in the final plot, Figure 5.10 iv.), with the fraction of Fe antisites on NC lattice sites significantly increasing with decreasing radii.

By taking into account the surface area of the NCs, the effect of NC diameter did not have a noticeable effect on the clustering of Fe interstitials and vacancies. In a pure bcc system, the clustering occurs primarily during the thermal spike and then shortly afterwards via the diffusion of interstitials and vacancies. In the case of a Fe-NC system, most interstitials and vacancies are generated near the boundaries of the NC during the shockwave. After the peak damage state, the Fe interstitial atoms in the matrix preferentially migrate towards the NC. An interesting phenomenon, shown in Figure 5.4, is the migration of defects after the peak damage state. The interstitials and vacancies, during the relaxation process of the cascade, surround the NC forming a uniform-thin layer of defects. These point defects are not limited to the shockwave volume, but over time begin to surround the entire NC. This property shows that Y_2O_3 NCs act as a key factor in irradiation resistance of the Fe matrix. Fe antisite evolution shows that within the NC, there is very little difference in the peak number of antisites during the peak damage state and the number of antisites at the end of the simulation. The antisites that are able to penetrate into the NC during the primary shockwave are maintained and play a key role in the evolution of the NC.

5.2.3 Y_2O_3 NC

Figure 5.11 shows a visualization of the evolution of defects within the NC. Unlike the standard cascade evolution, the damage within the NC continues to grow until it later reaches a plateau level. The Fe antisites impeding into the NC play a key role in this evolution trait of NCs. The Fe antisites within the NC tended to stay in the NC after the initial shockwave, shown in Figure 5.8. During the primary shockwave, the NC atoms are displaced. The standard displacement cascade is followed by a thermal peak where interstitials migrate to vacancies and recombination occurs; however, in the case of the NC, due to the combination of both Fe antisites and the incoherent boundary between the Fe matrix and the NC, recombination is considerably more difficult compared to a pure system. Figure 5.12 shows the evolution of the defect populations within the NC based on diameter. The 2 nm and 4 nm NC show a slight amount of recombination, whereas the 6nm NC never has an initial peak defect population early, but rather a gradual growth in the number of defects until reaching a plateau. In the case of increasing NC diameter, more and more PKA energy is transferred to the NC versus the Fe matrix. The key evolution in the primary damage state of a cascade during the NC is that over the course of each simulation the NC reaches a plateau in damage and is unable to recover back to the NC's standard cubic structure.

The PKA energies examined show two key ways that the PKA energy can be dispersed through the NC. At lower energies, the PKA energy instead of transferring through the NC, bounces off the NC, causing some damage to the NC, but the resulting shockwave has a minimal effect on the NC compared to higher PKA energies. In the 1 keV and 5 keV cases, the behavior is more comparable, where the 10 keV cases their own category. In these cases, the shockwave is contained to one side of the NC, with the cascade affecting a larger portion of the NC surface area for the 5 keV case compared to the 1 keV case. The PKA energy, rather than transferring through the NC, ricochets off of the NC and back to the Fe matrix. In the 10 keV simulations, the PKA energy is able to penetrate the NC, and the peak damage state occurs with two smaller shockwaves on opposite sides of the NC; however, significantly more energy is transferred to the NC in the 10 keV PKA case. With increasing energy, the initial number of Frenkel pair defects within the NC at the peak damage state increases, causing a larger defect population in the NC.

Figure 5.13 shows the fraction of NC defects compared to the number of NC lattice sites, for the 2 nm, 4 nm, and 6 nm NCs for the three PKA energies investigated in this study after the defects have reached their plateau population. With increasing PKA energy the fraction of defects increases for all three cases. In comparing the number of defects based on PKA energy and NC diameter. There is a plateauing amount of defects over the course of the cascade within the NC, with this plateau increasing with PKA energy. The plateauing effect within the NCs is due to incoherency between the α-Fe matrix and the cubic Y_2O_3 NC. The incoherency, along with the Fe boundary atoms, seems to cause the NC system to go into disorder. The NC loses its original core-shell structure and is not able to recover throughout the cascade relaxation process. The Y and O atoms stay within the original volume of the NC lattice sites, and a point defect sink quickly surrounds the NC. Although the damage leads to an increase in disorder of the NC, the NC’s atoms stay together, thus future cascades will have to interact with the newly formed point defect sink, prior to the NC.

5.2.4 Temperature Dependence

The previous sections looked at the general trends within the following regions: Fe matrix, Fe-NC interface, and the NC. This section will summarize the results as it pertains to the temperature affect within these three regions.

Figure 5.14 plots the number of interstitials and vacancies at the peak damage state and at the final relaxed state for all PKA energies and temperatures investigated n this dissertation. From figure 5.14 i.) and ii.) the change in number of vacancies is shown. From these plots it is evident that for a pure Fe matrix there is a slight change in the number of Frenkel pairs created within the pure Fe matrix, with the peak number of point defects being slightly higher and the final number of defects being very similar. As shown in Figure 5.14 i.) and ii.) there is little effect on the number of vacancies created within the Fe matrix at higher temperatures. However, although there is little effect, there is a slight increase in the number of vacancies at higher temperatures. The change in the interstitial population is plotted in Figure 5.16 iii.) and iv.). In agreement with the general trends in the above sections, the 2 nm conditions at all three temperatures showed a similar amount of interstitials as a pure Fe system. In the case of the 4 nm and 6 nm cases a general trend of a slight increase in the number of interstitials with increasing temperature.

As discussed in section 5.2.2, the key evolution of damage in that region is based on the fraction of Fe interstitials that are antisites. Figure 5.15 plots the fraction of Fe interstitials within the Fe-NC region that are antisites. From figure 5.15 the affect temperature has on the fraction of antisites is minimal. As in most cases the average of the fraction slightly increased with increasing temperature; however, although there is a slight increase in the fraction, this increase is well within the standard deviation markers for the 100 K, 300 K, and 600 K cases, suggesting that temperature has little effect on the primary damage state of the interface region of the NC.

As the energy of the cascade transferred to the NC itself, temperature had some somewhat interesting properties, especially at lower energies. Figure 5.16 plots the fraction of point defects as a function of the number of lattice sites within a NC. Figure 5.16 i.) shows the NC disorder fraction for vacancies and figure 5.16 ii.) shows the NC disorder fraction for interstitials. In the case of the 1 keV cases run in this simulation an interesting phenomenon occurs. At 600 K the fraction of disorder is significantly higher for both vacancies and interstitials in both the 2 nm and 6 nm diameter cases, as the 4 nm simulations are fairly similar at all three temperatures. In this case as the PKA energy is able to more easily penetrate the NC at lower energies, this is evident in the increased amount of damage within the NC at 1 keV for both the 2 nm and 6 nm diameters. At higher energies the average fraction of disorder for the three NCs diameters and temperatures is within standard deviation, suggesting that temperature has no effect on the structure of NC above 1 keV PKA.

Table 5.1. The key parameters are shown for the Fe-NC cascade simulation cases.

NC Diameter (nm)	# of Cases	Temp (K)	Energy (keV)	Lattice Units	Box Length (Å)	Number of Fe Atoms	Number of NC Atoms
0	16	100, 300, 600	1,5,10	50 x 50 x 50	142.9	250 000	0
2	16	100, 300, 600	1,5,10	50 x 50 x 50	142.9	249 661	398
4	16	100, 300, 600	1,5,10	50 x 50 x 50	142.9	247 085	3 172
6	16	100, 300, 600	1,5,10	60 x 60 x 60	171.2	422 231	10 700

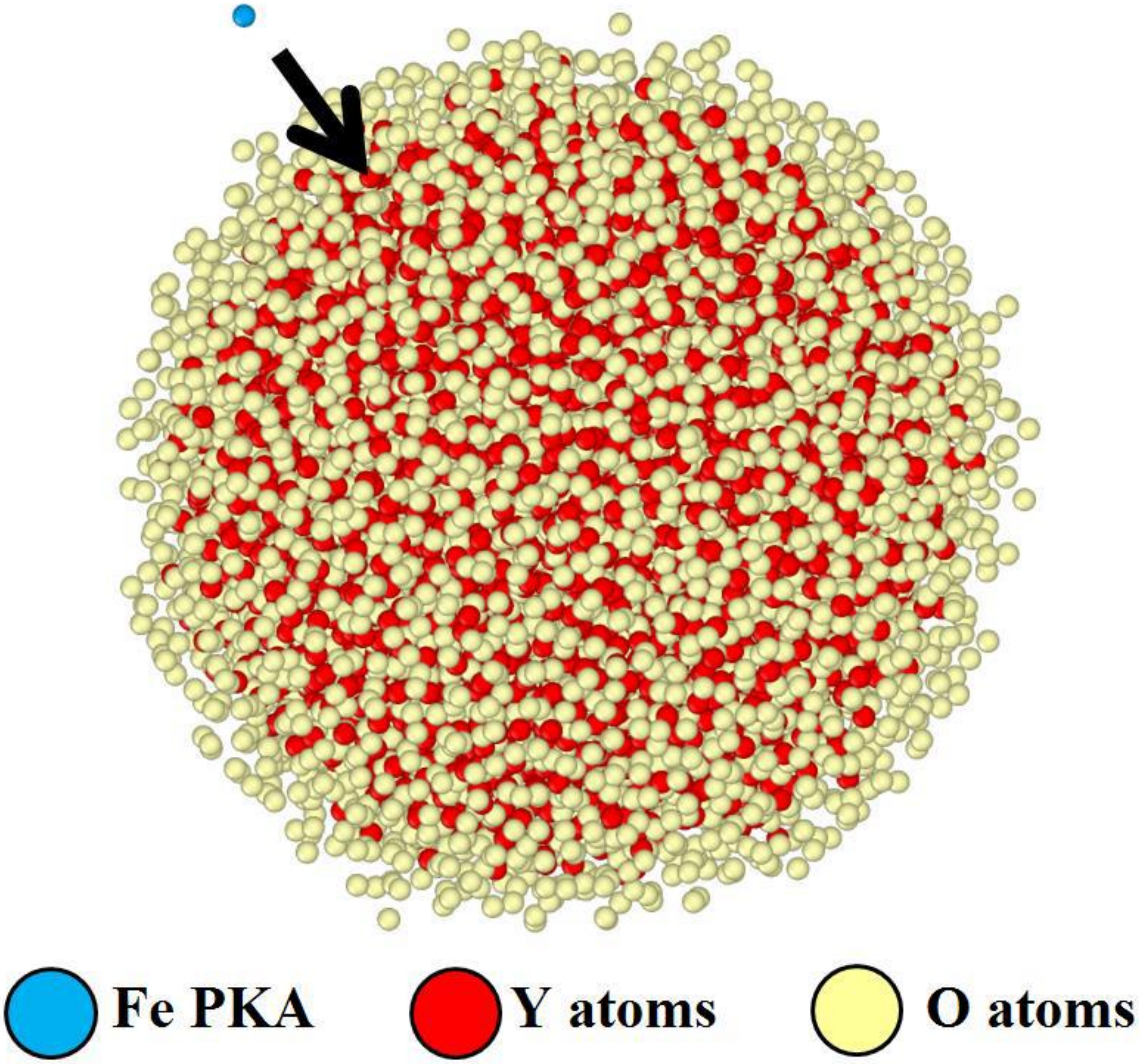

Figure 5.1. An illustration of the Fe-NC system after equilibration with the non PKA Fe atoms removed. The Fe PKA is given kinetic energy and a direction towards the center of the NC to simulate a displacement cascade within the NC[127].

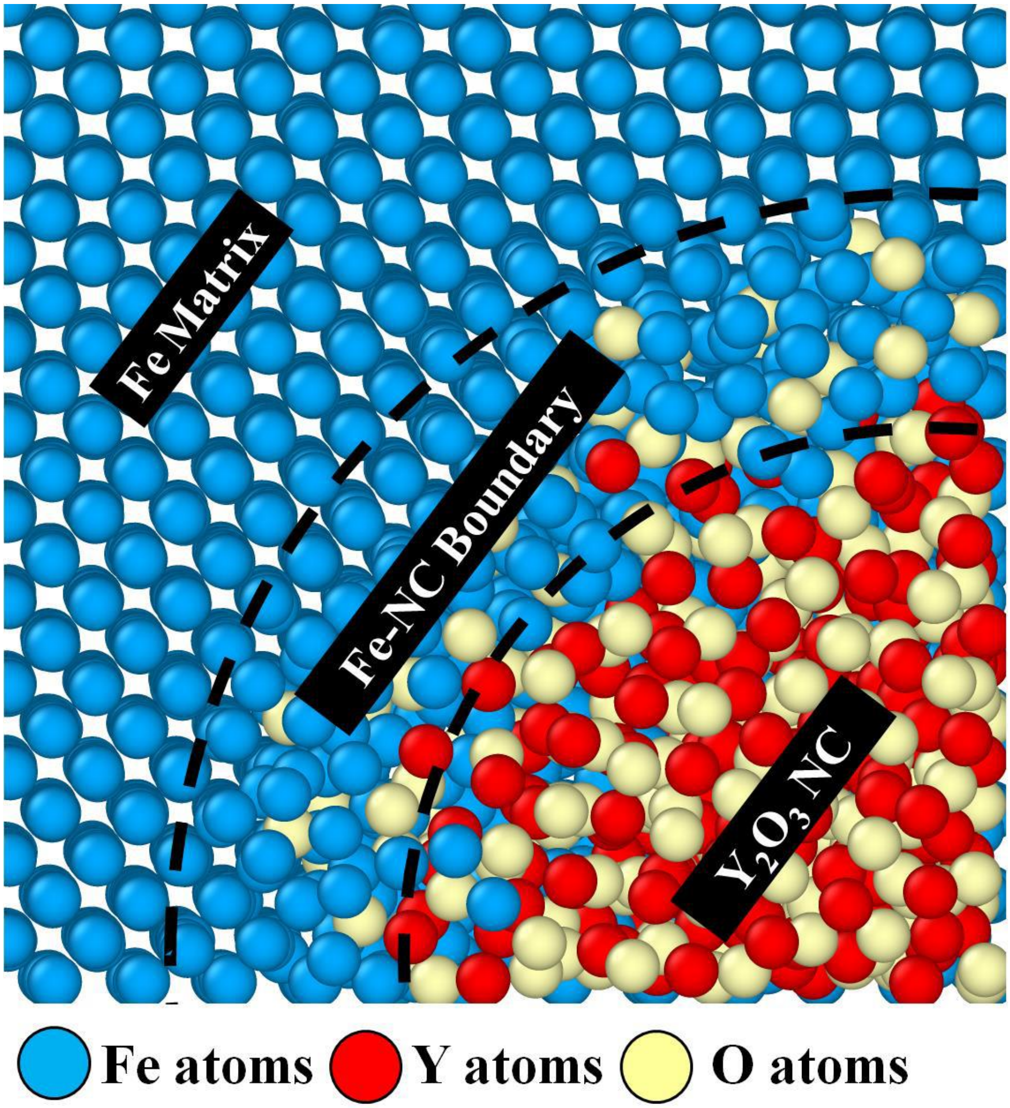

Figure 5.2. An illustration showing the regions of interest during the cascade simulations. From outer to inner; the first region is the pure Fe matrix. These atoms are far enough away from the NC, and have no interactions with the Y or O atoms. The next region is the Fe-NC boundary. This region consists of the Fe atoms that have been displaced from the pure bcc Fe lattice positions due to interactions with the Y and O atoms. And last the pure Y2O3 NC[127].

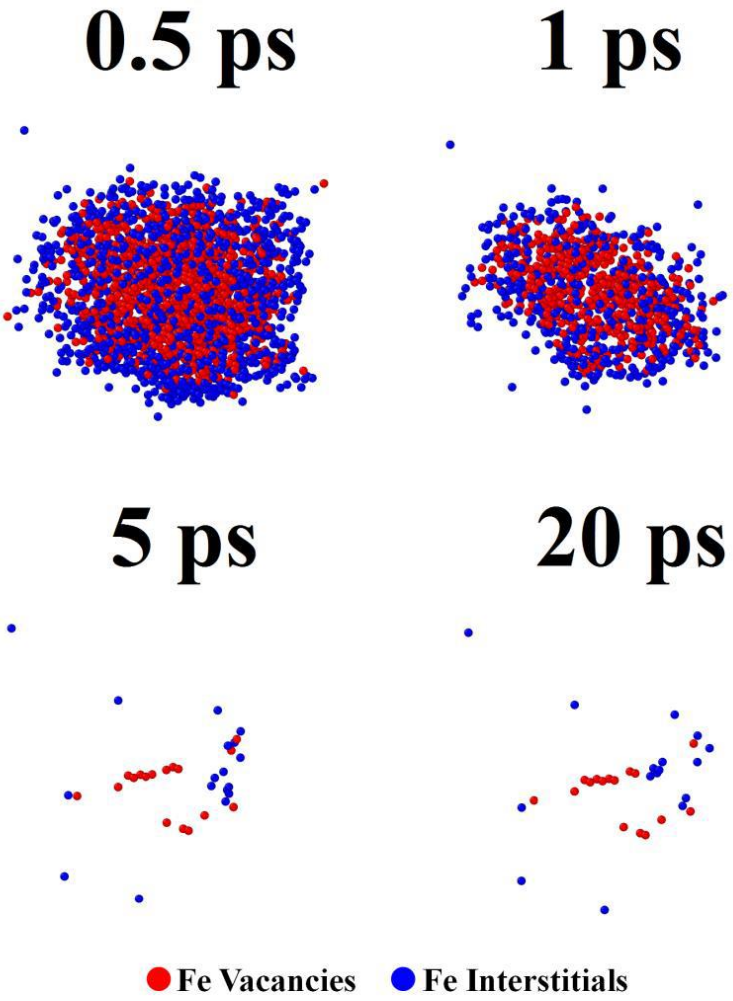

Figure 5.3. Snapshots showing a standard cascade of a 10 keV PKA in α-Fe. The peak damage occurs in a single shockwave that quickly dissipates, reaching an equilibrium number of interstitials and vacancies around 5 ps[127].

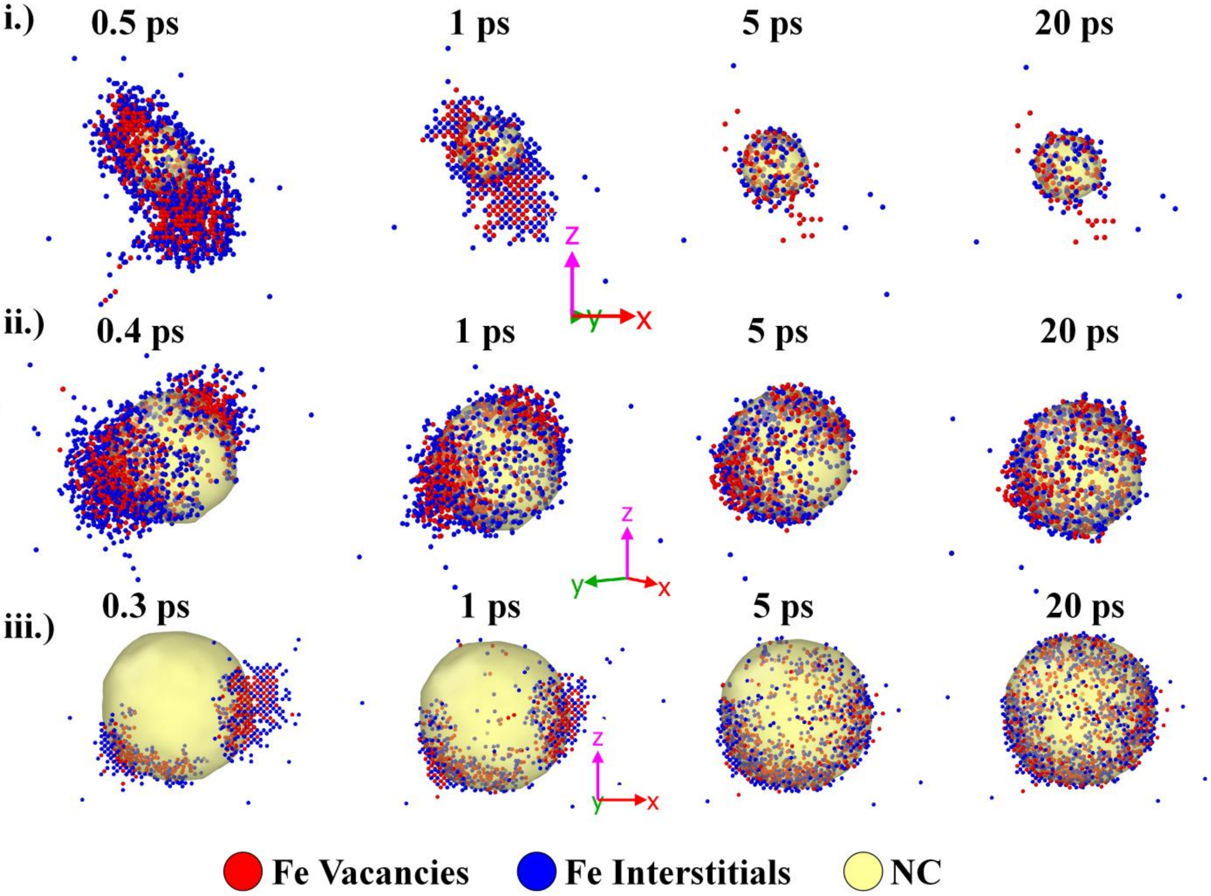

Figure 5.4. Example cases of the defect evolution of a 10 keV displacement cascade in the Fe-NC systems. From top to bottom: i.) 2 nm, ii.) 4 nm, and iii.) 6 nm NCs[127].

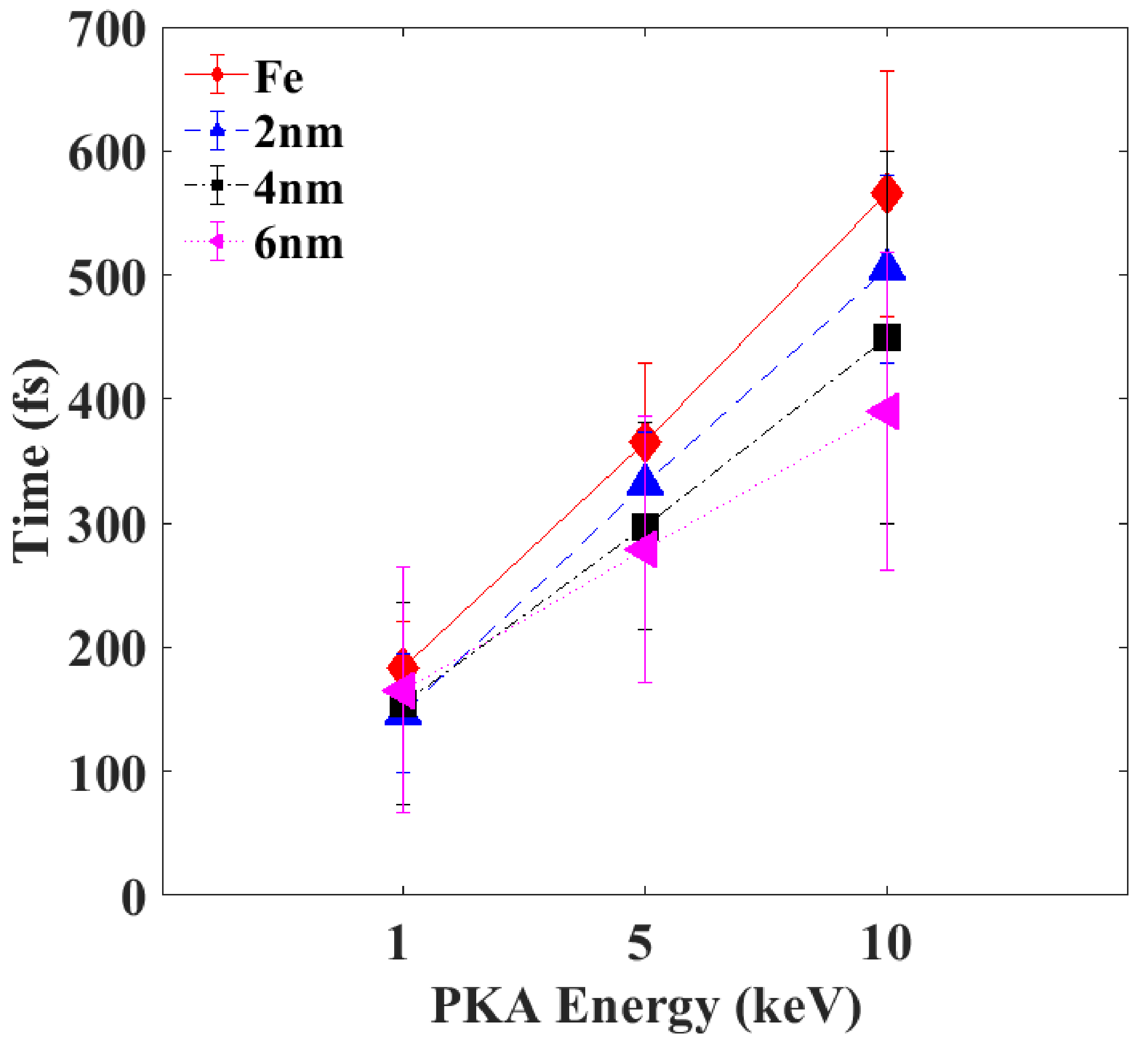

Figure 5.5. The time at which peak point defect populations occur within the Fe matrix as a function of NC diameter and PKA energy.

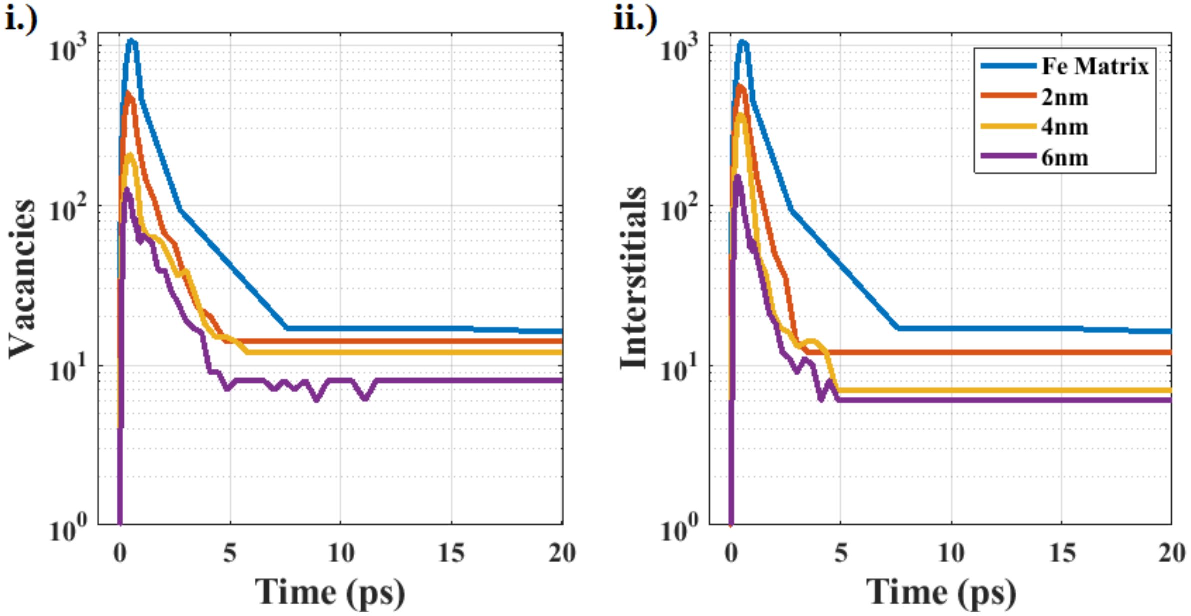

Figure 5.6. The evolution of the point defects generated within the Fe matrix for a 10 keV PKA, showing the effect a NC has on defect population in the Fe matrix. i.) Fe vacancies and ii.) Fe interstitials[127].

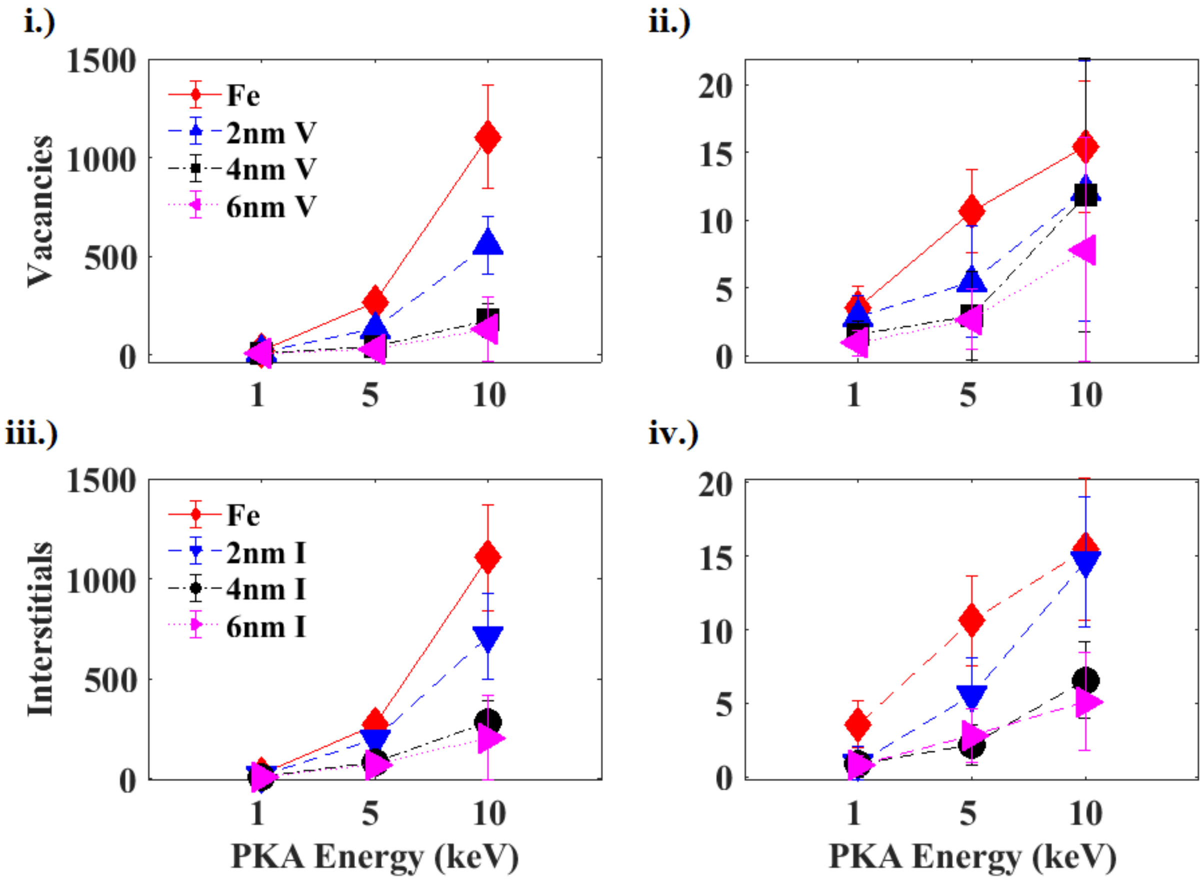

Figure 5.7. Comparing the number of interstitials and vacancies averaged over the 8 cases for the Fe matrix. The number of the defects at the peak and at the end is plotted. i.) Vacancies at peak damage, ii.) vacancies at the end of the simulation, iii.) interstitials at peak damage and iv.) interstitials at the end of the simulation[127].

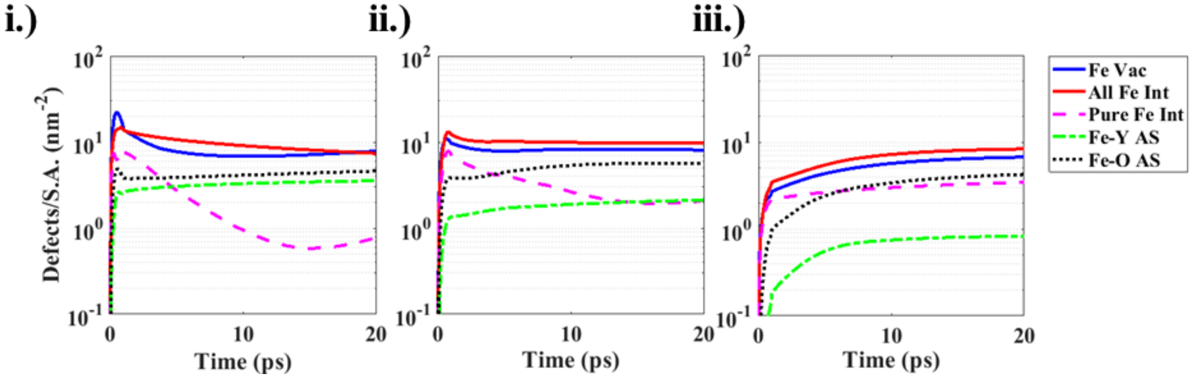

Figure 5.8.The evolution of the concentration of Fe defects surrounding the NC; i.) 2 nm NC, ii.) 4 nm NC, and iii.) 6 nm NC[127].

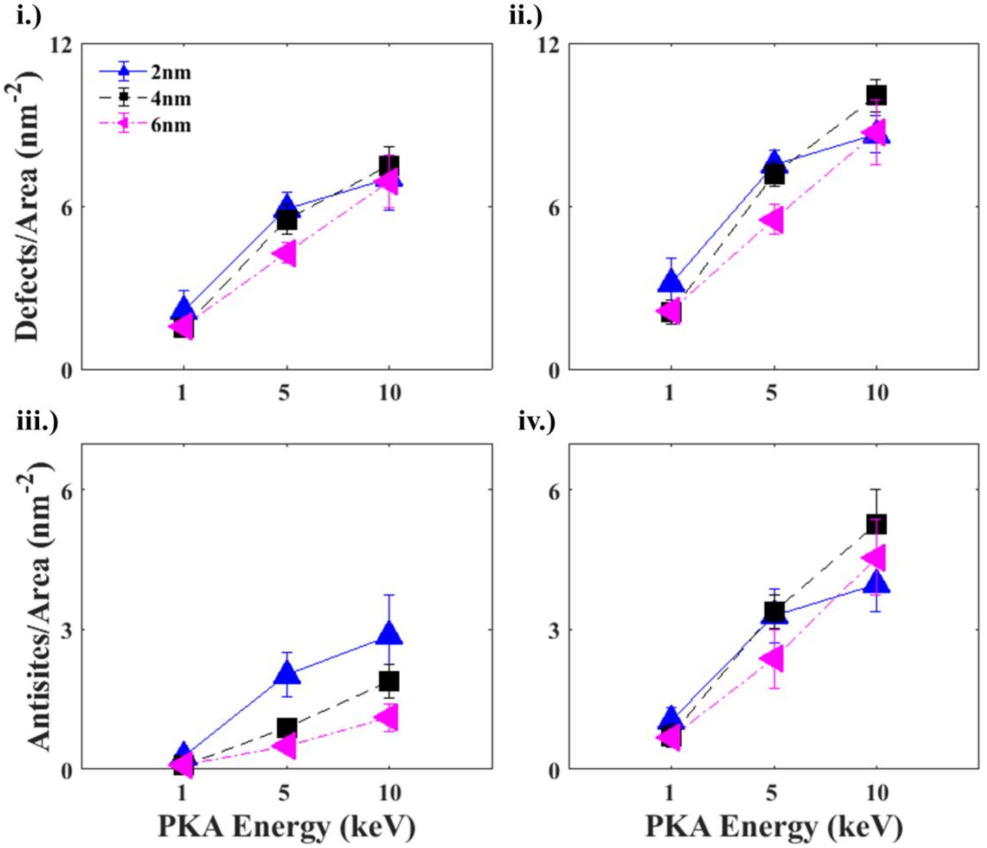

Figure 5.9. The Fe defects surrounding the NC are characterized, averaged over all the simulations; i.) Fe vacancies, ii.) Fe interstitials, iii.) Fe-Y antisites, and iv.) Fe-O antisites[127].

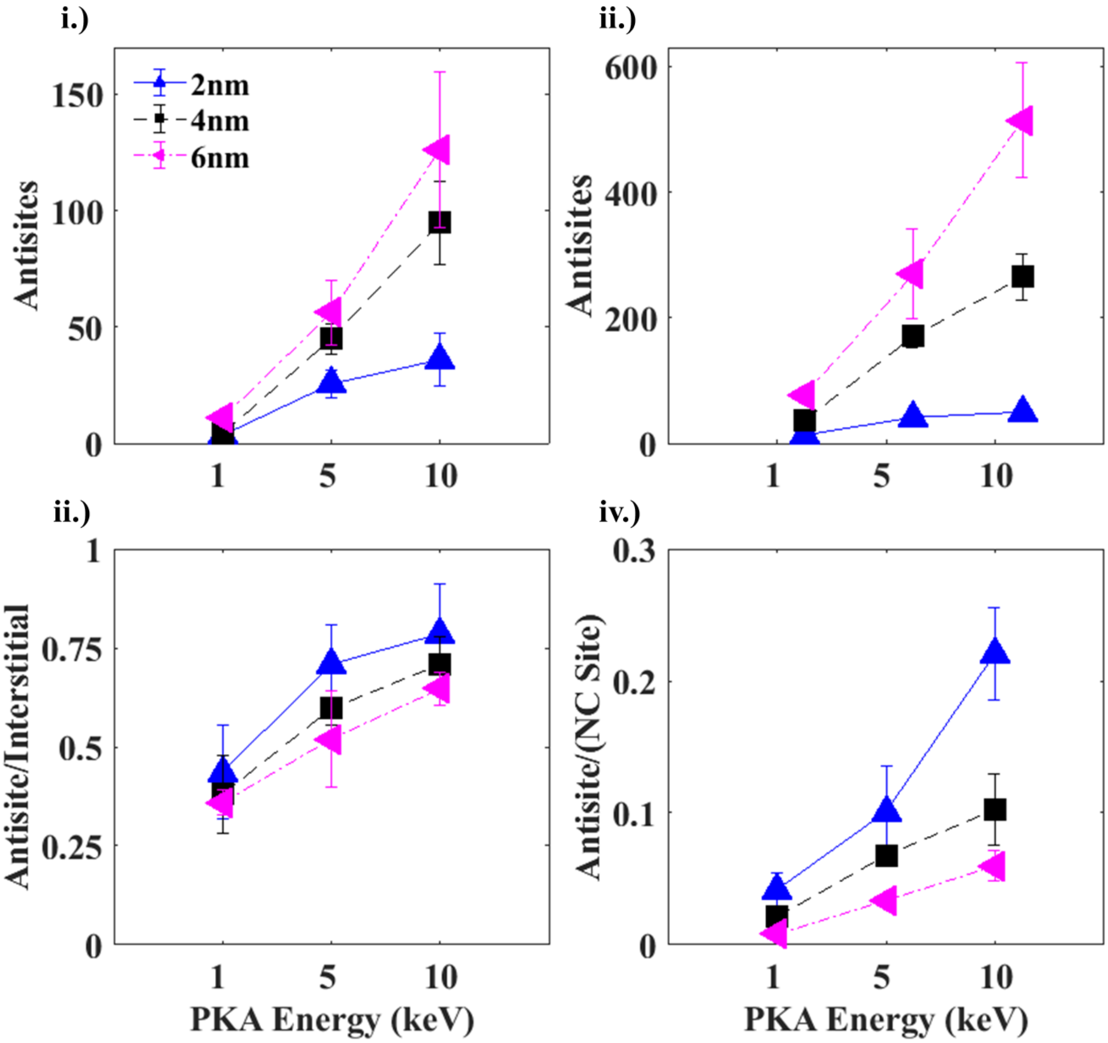

Figure 5.10. Plots showing key information for the Fe antisites within the NCs; i.) number of Fe-Y antisites, ii.) number of Fe-O antisites, iii.) the fraction antisites to the interstitial population, and iv.) the fraction of Fe antisites to NC lattice sites[127].

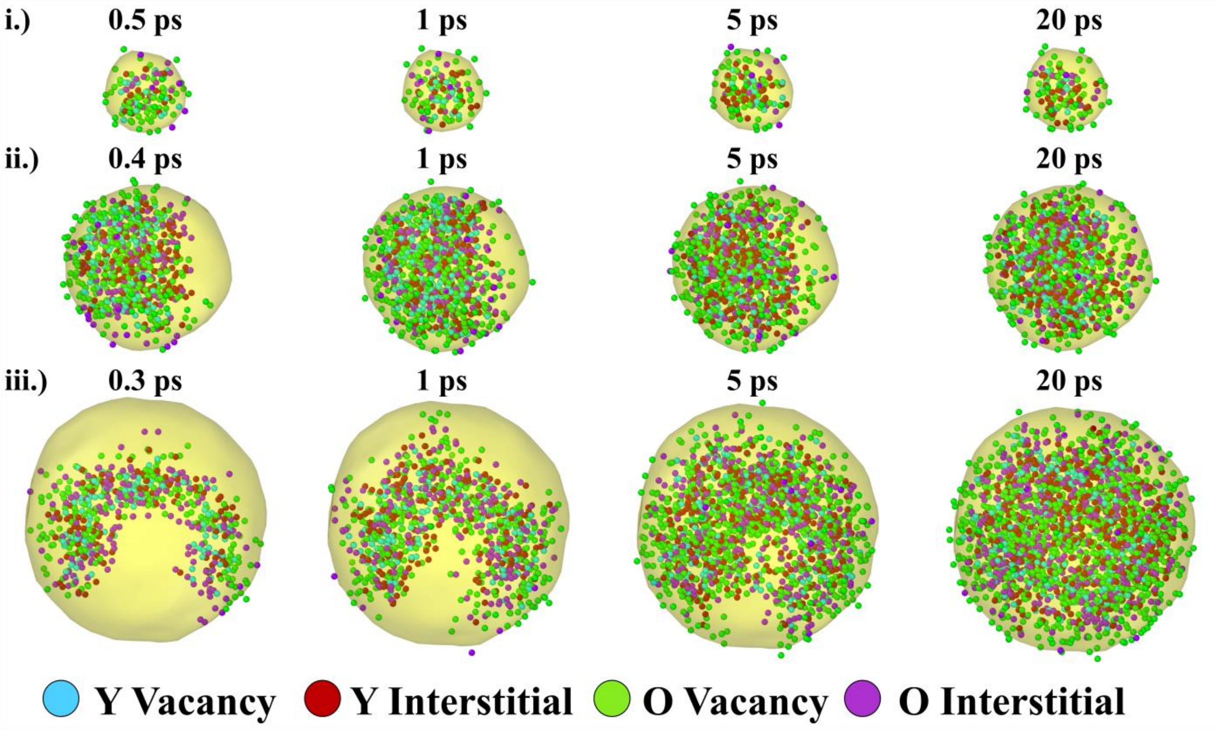

Figure 5.11. The evolution of a typical, 10 keV displacement cascade within the Y2O3 NC is shown at various times in the simulation. i.) 2 nm NC, ii.) 4 nm NC, and iii.) 6 nm NC[127].

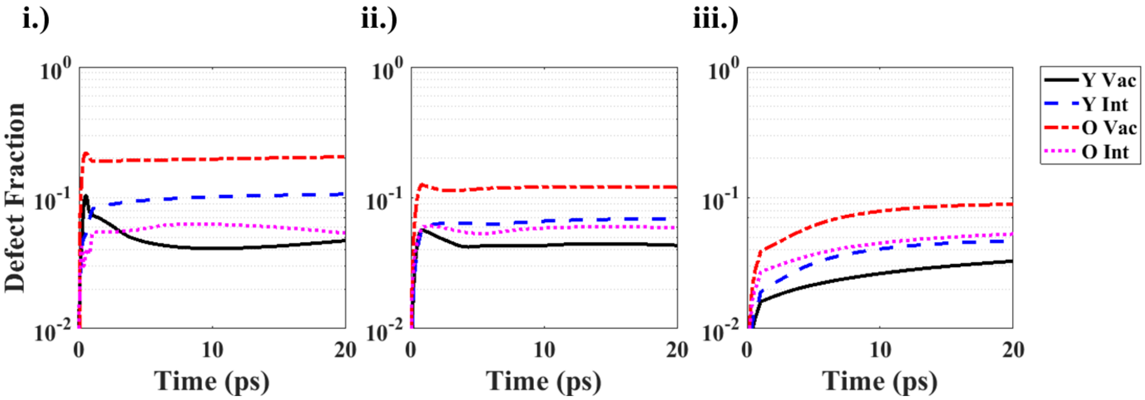

Figure 5.12. Illustrations of the defect fraction evolution over the course of the simulation for 3 typical cases; i.) 2 nm, ii.) 4 nm, and iii.) 6 nm NCs[127].

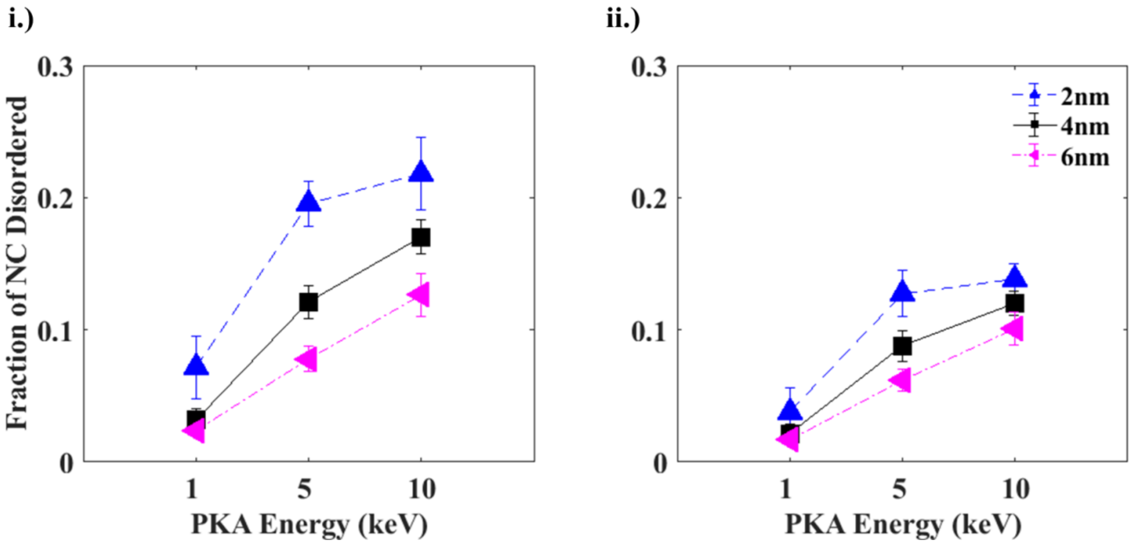

Figure 5.13. The fraction of the defects in the NC at 20 ps as a function of PKA energy and diameter; i.) vacancies and ii.) Interstitials[127].

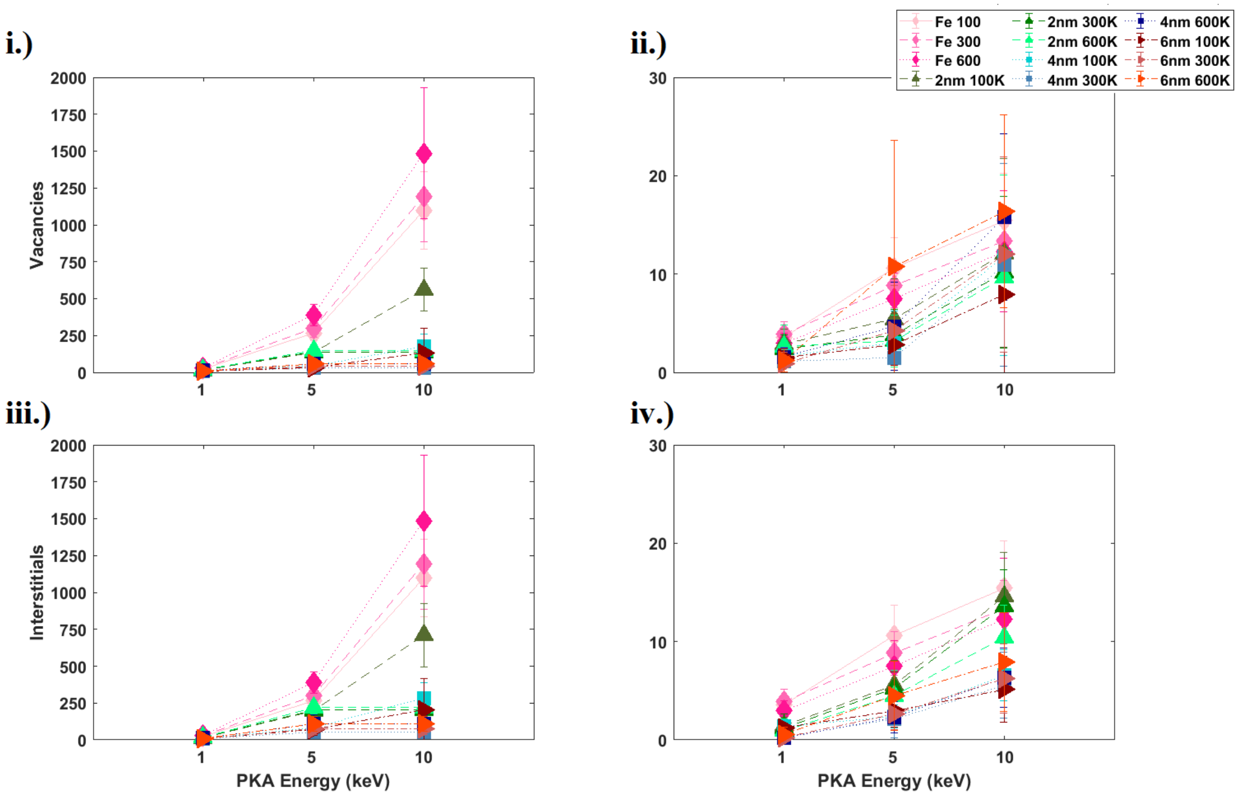

Figure 5.14. The affect temperature has on the number of point defects created during the peak damage state of a cascade and the number of point defects at the end of the relaxation state based on NC radii and PKA energy. i.) peak number of vacancies, ii.) final number of vacancies, iii.) peak number of interstitials, iv.) final number of interstitials.

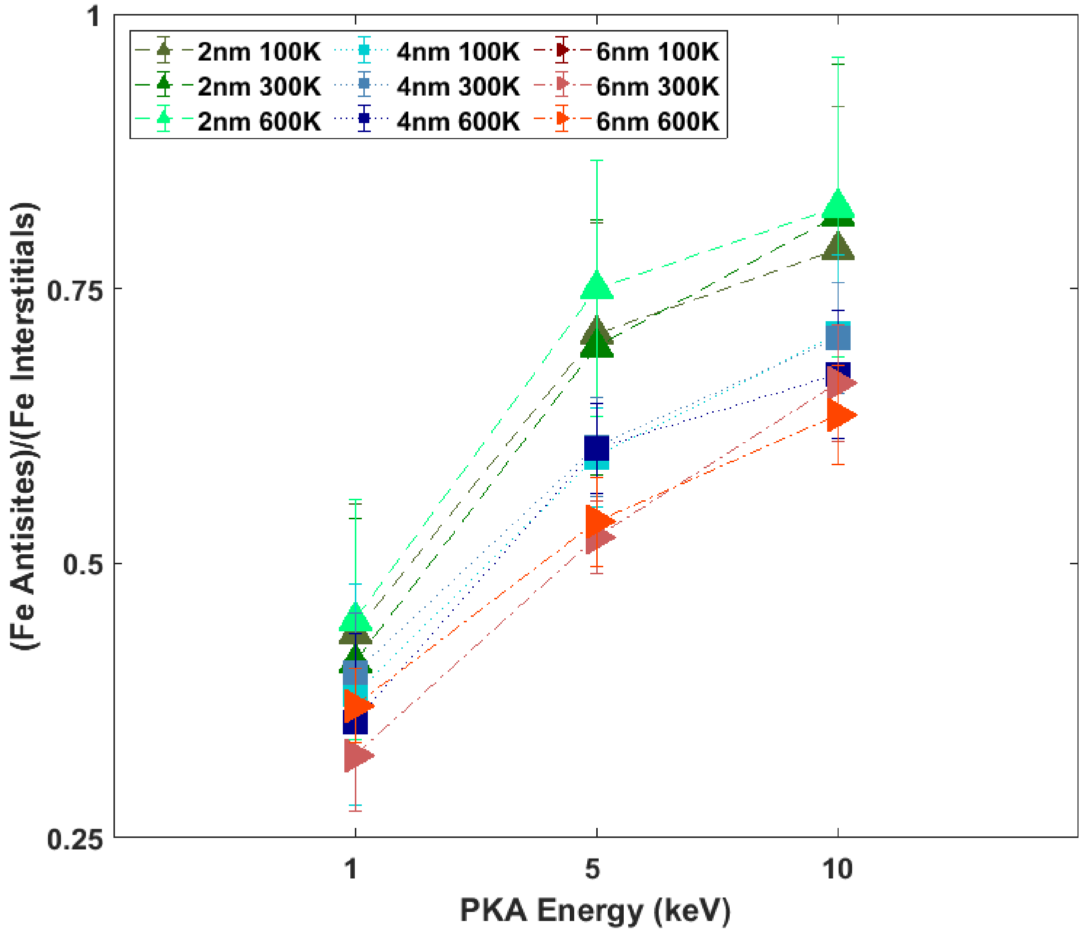

Figure 5.15. A look at the affect temperature has on the fraction of antisites to total interstitials for the Fe-NC interface region.

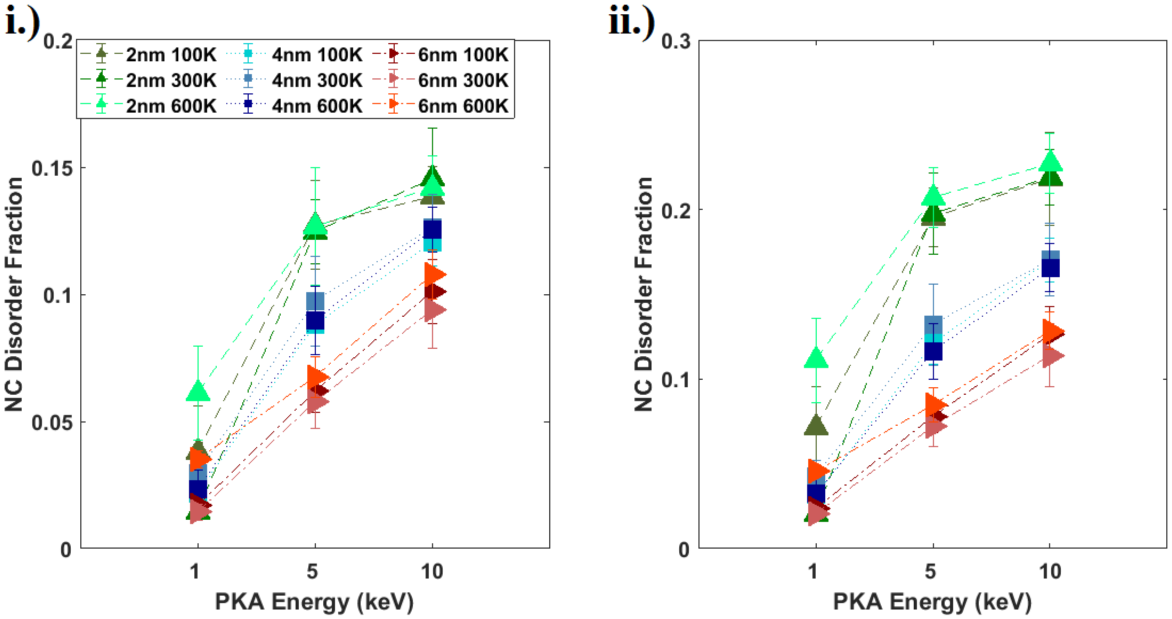

Figure 5.16. The affect temperature has on the NC disordered fraction. i.) vacancies ii.) interstitials

Chapter 6 - Dislocation Interactions with Nanoclusters

Next generation nuclear reactors require materials that are able to withstand higher strengths for the new corrosive environments and higher temperatures. Oxide dispersion-strengthened (ODS) steel is one of the key materials being considered for next generation reactors. Specifically, ODS steels have been proposed for duct, cladding, and structural materials for next generation fission reactors and as a material for the first wall and a blanket material in fusion reactors[11,20,102,118]. As radiation damage produces defects within structural materials; these point defects, over time, grow into large defect structures, such as dislocations and voids. Atomic modelling of these structures plays a paramount part of understanding the mechanism of evolution of these defects and an insight into the added strength of ODS steels[31].

ODS steels are considered to be the material of the future when it comes to nuclear reactors. As ODS steels are able to take the generally positive attributes of the base ferritic-martensitic (F/M) and improve on some of the key properties[20]. ODS steels by the addition of a YO powder during the manufacturing process, creates a metal with high thermal stability, high temperature creep, and corrosion resistance[11,20,128]. The major difference between the ODS steels and the base F/M steel is the introduction of the large, stable population of nanoclusters (NCs) during the ball milling and heat consolidation techniques. The population of NCs is controlled by the heat treatment technique and temperature. The key strength addition of ODS steel is in the dislocation treatment technique and temperature. The key strength addition of ODS steel is in the dislocation pinning occurring at these NCs, hence the size and density of NCs is key in the improved strength[44,47,94,129].

Stress-driven dynamics of dislocations has been a key area of growth, as simulations have improved in modelling dislocations[49,130,131]. Properly modelling of the dislocation structure using molecular dynamics (MD) has been a major area of focus in recent years[46,47,51,94,132]. Two major mechanisms have been shown to control the depinning mechanism of an obstacle and a dislocation. The first is the Orowan mechanism, as the dislocation overcomes the obstacle by bowing around the structure[133,134]. The second mechanism is climb, as the dislocation is able to climb over the obstacle[49].

In general, the increased strength from the introduction of obstacles into a metal matrix is based on a few key features: size, orientation, temperature, and composition of the obstacle[135]. ODS steel gains some of its strength from the population of NCs within the base α-Fe matrix. Experimental studies have looked at the effects of single dislocation with precipitates[134,136]. However, as a single dislocation is much harder to control in an experiment, many MD and dislocation dynamics (DD) studies have been used to better understand the affect precipitates have on the depinning mechanism and strength of the obstacles[30,49,137–142].

Many studies have looked at the effect precipitates have on a dislocation's mobility and the depinning mechanism, not including the standard NC seen in ODS steels: voids, carbides, and dislocation loops[49,51,148,130,135,139,143–147]. Only one study has been published on the depinning mechanism between an edge dislocation and an embedded Y_2O_3 NC with edge dislocations[142]. However, up to this point the depinning mechanism of screw dislocations on NCs has not been investigated.

In this present study, MD simulations have been used to study the interaction between a single edge dislocation and a Y_2O_3 NC in an α-Fe matrix, and a single screw dislocation and a Y_2O_3 NC in an α-Fe matrix. This study looked at the difference dislocation type has with the depinning mechanism for the NCs based on dislocation type. Along with the core study of difference in dislocation type; temperature and diameter of the NC are also investigated in the affect these have on the critical resolved shear stress of the NCs. The effect NC diameter has on the obstacle strength is also investigated. The computational details are described in the next section, followed by the results and discussion.

6.1 Dislocation-Nanocluster Simulation Setup

The MD simulations are carried out using large-scale atomic/molecular massively parallel simulator (LAMMPS) code[17]. The visualization tool Ovito, is used to analyze the atomic structure and dislocation mobility; in the Ovito software, the common neighbor analysis tool is the primary tool used as it is able to successful separate the Fe matrix from the NC and the dislocation to analyze the movement and structure of the dislocation[18]. The introduction of the edge dislocation into the simulation box is based on the atomic methodology published by Bacon and Osetsky[44]. The screw dislocation is based on the concepts covered by Hirth[149]. The atomic potentials used to model the NC, Y, O, Fe-Y, and Fe-O, are the potentials developed by Hammond[114]. The Hammond potential is designed to model radiation damage and the structure of NCs; however, this potential is not optimized for the inclusion of a dislocation within the Fe matrix. In order to correctly model the dislocation, structure and mobility, an embedded atom model potential developed by Ackland is used to control the Fe atoms[26]. The Ackland potential has been used in many studies to model both edge and screw dislocations in the bcc Fe matrix[49,94]. Table 1 lists the key characteristics of the simulation cell in this study.

Prior to modelling the mobility and interaction of dislocations, a simulation box without a NC needs to be designed to calculate a few key characteristics of the base Fe material. A simulation box of pure Fe is created with the following coordinate system such that x, y, and z are aligned on the $[111]$, $[1\bar{1}0]$, and $[11\bar{2}]$ directions, respectively. The system is then relaxed using the conjugant gradient method and equilibrated at temperature for 50 000 timesteps (50 ps). From there a shear stress is applied along a fixed layer on the top of the x-y plane, to apply a shear stress. This is used to calculate the shear modulus of the Fe system.

6.1.1 Edge Dislocation - Nanocluster Setup

Figure 6.1 shows a schematic of the edge dislocation setup used in these simulations. The x, y, and z axes of the coordinate system are aligned to $[111]$, $[1\bar{1}0]$, and $[11\bar{2}]$ directions, respectively. In addition, the box lengths of the simulation cell in the x, y, and z directions are L_x, H, and L_z, respectively. Periodic boundary conditions are applied along the x and z directions, whereas the y direction has a fixed boundary such that a shear stress is applied to force the edge dislocation to move in the x direction towards the NC.

The process of creating a simulation cell with both a dislocation and a NC consists of the following primary process. First a dislocation is added to a pure Fe system, and following the inclusion of the dislocation a NC is added afterwards. The edge dislocation is added to the Fe matrix based on the method described by Osetsky[44]. For the edge dislocation a half plane of atoms along the Y-Z plane are removed; following the removal, the atoms along that plane are shifted by the Burgers vector. After relaxation a straight edge dislocation is along the X-Z plane placed at y = H/2, and x = 1/3 L_x. The system is then relaxed using a combination of the conjugant gradient technique, which minimizes the energy of the system, and a box relax command, which minimizes the pressure of the system. This combination creates the ideal system for an edge dislocation to move within the Fe matrix.

After the edge dislocation is formed via energy minimization, the NC is then introduced into the simulation box. The center of the NC is located at x = 2/3 L_x and y = H/2. NCs of diameters 2 nm, 4 nm, 6 nm, 8 nm, and 10 nm are placed at the NC center location. The NC structure and setup is based on the technique used in a paper by Higgins[117]. Following the introduction of the NC the system is again relaxed with the conjugant gradient technique combined with pressure minimization. A fix is placed on the 3 atom layers on the top and bottom of the $[1\bar{1}0]$ direction. The system is then equilibrated at the desired temperature: 300 K or 600 K for 50 000 timesteps (50 ps). Following the relaxation and equilibration, the system is sheared, such that the fixed layers of atoms are given a velocity of 0.008 Å/ps in opposite directions along the top and bottom fixed layers in the X direction, causing the edge dislocation to move along the X direction towards the NC. The shear stress is applied via a velocity to better understand the critical depinning stress for the dislocation around the NC.

6.1.2 Screw Dislocation - Nanocluster Setup

Figure 6.2 shows the schematic setup of the screw dislocation. The x, y, and z axes of the coordination system are aligned to $[1\bar{1}0]$, $[11\bar{2}]$, and $[\frac{1}{2}\frac{1}{2}\frac{1}{2}]$ directions, respectively. The simulation box is displaced such that a screw dislocation forms along the y=H/2 and x = 1/3 L_x plane. Based on the equations by Hirth[149], equation 1, a perfect Fe simulation box is modified to have a screw dislocation.

$$w = b/(2\pi)\tan^{-1}(y/x) \qquad \text{(Eq. 1)}$$

Where w is the component of the screw dislocation along the z axis, b is an arbitrary constant determining the strength of the screw dislocation, and the arctangent describes the plane on which the screw dislocation sits. The x and z directions have periodic boundary conditions, with the y direction having a fixed boundary, such that a shear stress can be applied along the y boundary. Following a box relaxation using the conjugant gradient technique combined with pressure minimization, the screw dislocation is formed.

After the screw dislocation forms in the Fe matrix, an Y_2O_3 NC is placed along the y=H/2 and x = 2/3 L_x plane. NC diameters of 2 nm, 4 nm, 6 nm, 8 nm, and 10 nm are placed at the NC origin location. A similar relaxation technique is used with the inclusion of the NC, with the energy of the system being minimized in both energy and pressure. After the system is in the energy and pressure minimized state, the system is equilibrated at the ideal temperature: 300 K or 600 K over 50 000 timesteps (50 ps). Following the relaxation and the equilibration, the system is then sheared. The fixed layers on the top and bottom of the y axis are given a velocity of 0.004 Å/ps in opposite Z directions on the top and bottom fixed layers.

6.2 Dislocation-Nanocluster Simulation Results

The key benefit of ODS steels over the base F/M steels is the increased yield strength and creep rupture strength at higher temperatures[71]. The key difference between a base F/M steel and a ODS steel is the increased population of precipitates, tiny yttrium based nanoclusters (NCs), added to the base metal matrix. These NCs are able to strengthen the yield strength of the material without having a major consequence on the ductility of the material.

Along with understanding how a dislocation moves within a matrix, the interaction between microstructural features and dislocations are key in understanding the strengthening mechanism NCs have in ODS steel. The depinning mechanism between a dislocation and a NC plays a key role in understanding the benefit NCs have on increasing the strength of base F/M steels in ODS steels. For both edge dislocations and screw dislocations, the interaction a dislocation has with the NCs is associated with a primary pinning and depinning mechanism. The NC is able to pin the dislocation hindering the dislocations movement. However the added strength of NCs to the ODS alloy is based on the type of dislocation, diameter of the NC, and the temperature of the simulation cell. A key aspect of figures 6.3 and 6.6 is that the red sphere contains both the NC and the surrounding Fe atoms displaced from the bcc Fe lattice sites due to the inclusion of the NC.

6.2.1 Edge Dislocation Interactions with a Nanocluster

Figure 6.3 shows the standard interaction between an edge dislocation and a NC. All NCs investigated in this study show the same basic interaction with the edge dislocation. As shown in figure 6.3i.), the standard dislocation is perfect along the z

($[11\bar{2}]$) direction after temperature equilibration. Prior to interacting with the NC, the dislocation moves with a constant velocity over the entire dislocation segment. As the dislocation approaches the NC, the segment of the dislocation that is in the path of the NC becomes pinned along the NC outer diameter. However, the dislocation segments, near the periodic boundary condition, away from the NC, continue to move at the same velocity, i.e. the dislocation begins to bow. As the dislocation segment closer to the periodic boundary moves, this causes more of the dislocation segment to interact with the NC. As the edge dislocation becomes more elongated away from the NC, cross-slip along the NC outer diameter starts to occur for the dislocation segment pinned. The depinning mechanism consists of the bowing of the edge dislocation around the NC and climbing via cross-slip over the NC. Figure 6.3iii.) shows the structure of the dislocation following depinning, and the structure of the dislocation now sits along two different X-Z planes.

Figure 6.4 shows how the NC diameter affects the evolution of the climbing mechanism as a function of NC diameter. Figure 6.4 shows the case for all the NCs examined in this study at 300 K. Figure 6.3 shows the initial structure of the edge dislocation immediately following temperature equilibration. Figure 6.3ii.) shows the edge dislocation immediately following the depinning from the NC and Figure 2 iic.) shows the edge dislocation several picoseconds later. Figure 6.4 shows the key aspect of how NC diameter affects the depinning mechanism of the edge dislocation. With increasing radii the amount of elongation of the dislocation along the direction of motion, X direction, increases as the non-pinned edge dislocation is required to move further from the center of the NC to overcome the obstacle. Figure 6.4iii.) shows the end results of the NC interaction. Immediately following the release from the NC, the pinned part of the dislocation shoots forward and the segment returns to a similar x location. As the edge dislocation recovers from the interaction with the NC, the end structure is most affected by NC radii, as the amount of climb increases with radii.

A key aspect in the evolution of the depinning mechanism with temperature is based on Figure 6.4. By maintaining a constant applied velocity to the fixed layers, the temperature of the simulation box directly controls the glide velocity of the edge dislocation. At higher temperatures the velocity of the dislocation decreases, as the dislocation requires less force to move within the Fe matrix. In comparing the depinning mechanism of the edge dislocation in the two temperature cases investigated in this study, the velocity of the dislocation plays the biggest role. As the velocity to move within the Fe matrix is decreased in the 600 K cases, the dislocation is able to more quickly reach the velocity needed to move in the un-impacted regions allowing the dislocation to become freed at lower applied stresses. Figure 6.5 shows the impact temperature and NC diameter have on the depinning stress of the edge dislocation. In the lower temperature cases, the NC diameter plays a larger role in increasing the strength of the material, whereas at higher temperatures the size of a NC has a smaller effect, seen in comparing the change in stress from 300 K to 600 K.

6.2.2 Screw Dislocation Interactions with a Nanocluster

Figure 6.6 shows the standard interaction between a screw dislocation and a NC, with the screw dislocation sits on the z ($[\frac{1}{2}\frac{1}{2}\frac{1}{2}]$) plane. In comparison to an edge dislocation, the motion is very different. As a shear stress is applied to the simulation cell, kinks along the dislocation line begin to form. The movement of the screw dislocation is based on the movement of the single or multiple kinks that form, as the kinks drag the whole dislocation segment along the x direction, [110] plane. As the screw dislocation moves towards the NC, the velocity along the entire dislocation begins to stall and the dislocation becomes pinned along the NC, shown in the first part of figure 6.6ii.). As the stress continues to build along the pinned dislocation, a kink soon forms along the dislocation segment.

In comparison to a kink in the α-Fe matrix, the kinks formed as part of the NC required a significant increase in the amount of applied stress to move through the NC. The evolution of the kink within the NC is shown in figure 6.6ii.). As the stress increased, the dislocation away from the NC starts to bow in the x direction, around the NC. As the dislocation near the periodic boundary bows further into the matrix, the kink becomes more and more prominent within the NC and the kink starts to evolve in a way that it thins in the z direction and increases in length along the x direction. Once a critical stress is reached, the screw dislocation is able to break from the NC; however, as the dislocation is able to break from the NC a dislocation loop originating from the kink forms between the NC and the Fe matrix. Several picoseconds after the screw dislocation has overcome the NC, the screw dislocation is able to return to its original structure in the α-Fe matrix.

Figure 6.7 shows how the size of the NC affected the formation of a dislocation loop within the NC. In figure 6.7, the NCs are rotated to more easily show how the size of a NC impacts the size of the dislocation loop within the NC, whereas in the simulations the loop formation is possible to happen on both sides of the NC. With increasing NC diameter the size of the loop within the NC increases. Temperature played a smaller role in changing the screw dislocation's structure as it is pinned within the NC. Overall the temperature allowed the dislocation to move easier within the NC, but the loop still formed of nearly identical size. Along with an increasing loop size, another key aspect in the effect NC diameter has on the depinning mechanism of the screw from the NC is in the required stress.

Unlike the edge dislocation, the affect temperature has on the mechanism of depinning is significantly less compared to the edge dislocation interacting with the NC. Figure 6.8 shows the effect NC diameter and temperature have on the depinning stress. The affect temperature has on the depinning mechanism of a screw dislocation is visible at lower NC diameters, 2 nm and 4 nm. However, for the larger diameter cases, 6 nm, 8 nm, and 10 nm, the stress required to break through the NC is nearly identical.

Table 6.1. The key parameters for the simulation boxes are displayed for both the edge and screw dislocation set ups.

Y_2O_3 diameter (nm)	**Atoms in NC**	**Dimensions in lattice spacing**	**L_x (Å)**	**L_y(Å)**	**L_z(Å)**	**Total Number of Fe Atoms**	**Temperature (K)**	**Type of Dislocation (E/S)**
2	391	324 x 99 x 43	801.2	397.9	300.8	8 262 344	300/600	**E**
4	3 141	324 x 99 x 43	801.2	397.9	300.8	8 259 814	300/600	**E**
6	10 581	324 x 99 x 43	801.2	397.9	300.8	8 252 970	300/600	**E**
8	25 198	324 x 99 x 43	801.2	397.9	300.8	8 239 642	300/600	**E**
10	49 237	324 x 99 x 43	801.2	397.9	300.8	8 217 672	300/600	**E**
2	391	200 x 50 x 140	807.4	349.2	346.2	7 923 654	300/600	**S**
4	3 141	200 x 50 x 140	807.4	349.2	346.2	7 921 161	300/600	**S**
6	10 581	200 x 50 x 140	807.4	349.2	346.2	7 914 317	300/600	**S**
8	25 198	200 x 50 x 140	807.4	349.2	346.2	7 900 973	300/600	**S**
10	49 237	200 x 50 x 140	807.4	349.2	346.2	7 879 028	300/600	**S**

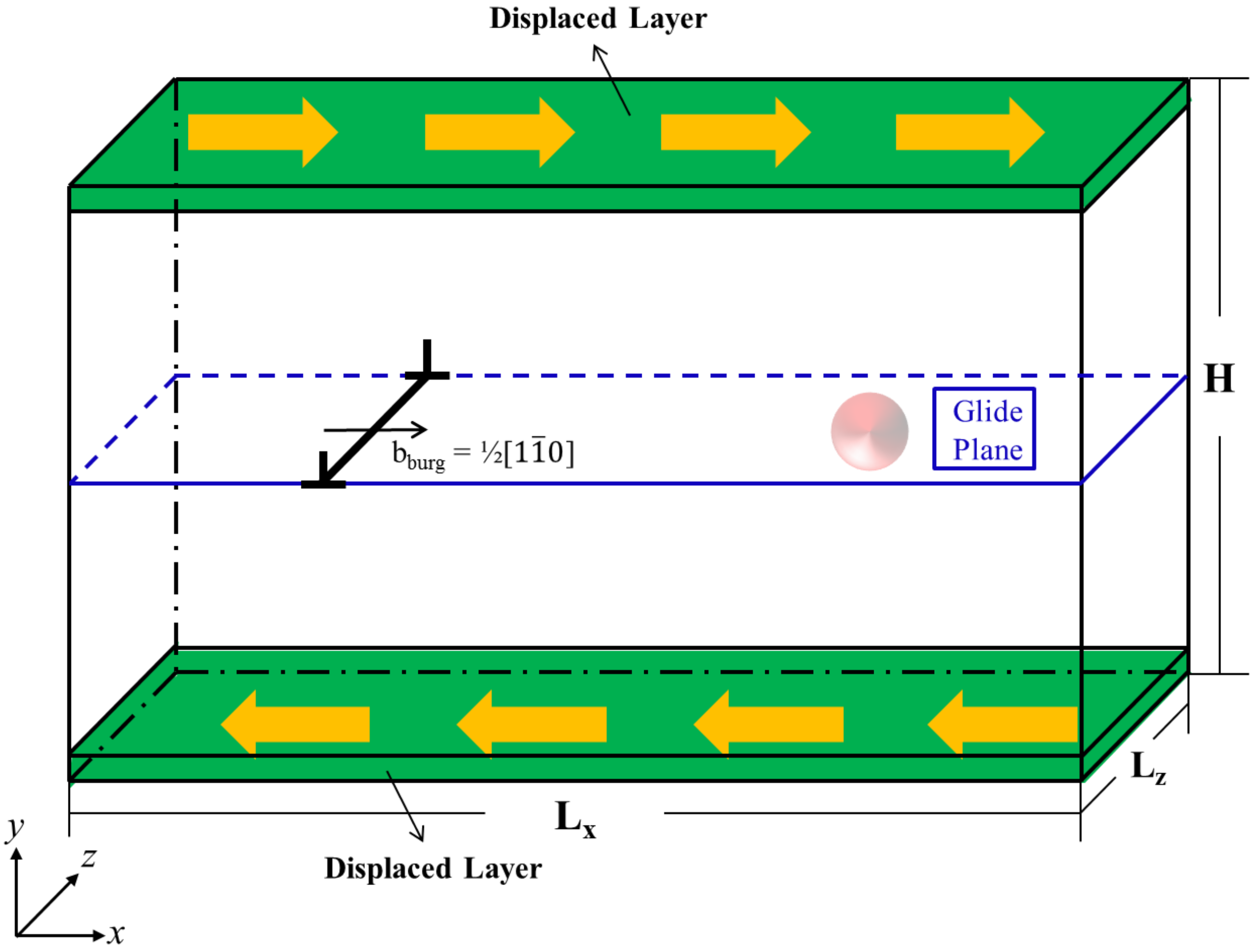

Figure 6.1. The schematic of the $\frac{1}{2}\langle 110\rangle\{112\}$ edge dislocation. The red sphere indicates the location of the NC, the yellow arrows indicate the applied velocity direction, and the blue rectangle indicates the glide plane.

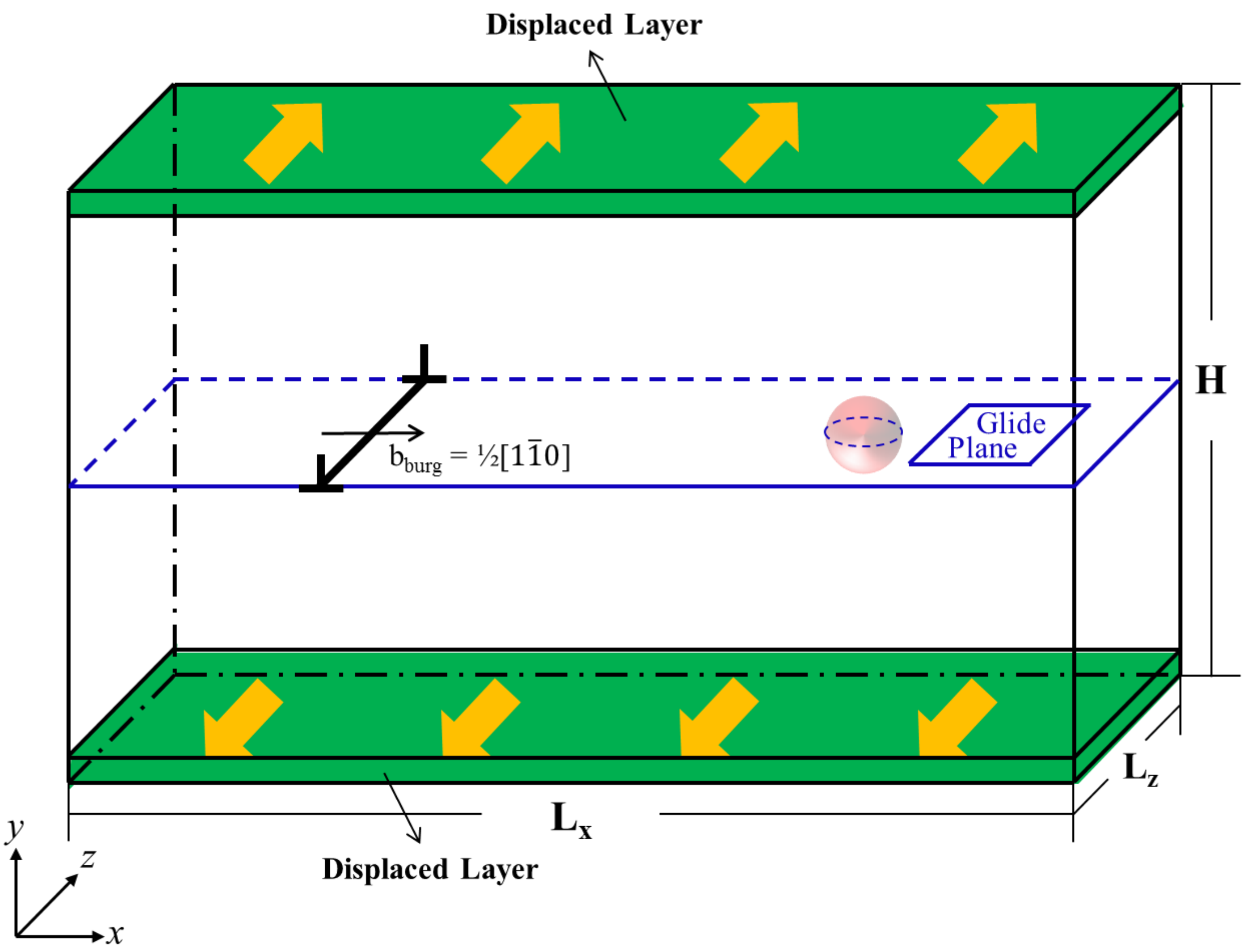

Figure 6.2. The schematic of the screw dislocation. The red sphere indicates the location of the NC, the yellow arrows indicate the direction of the applied velocity direction, and the blue rectangle indicates the glide plane.

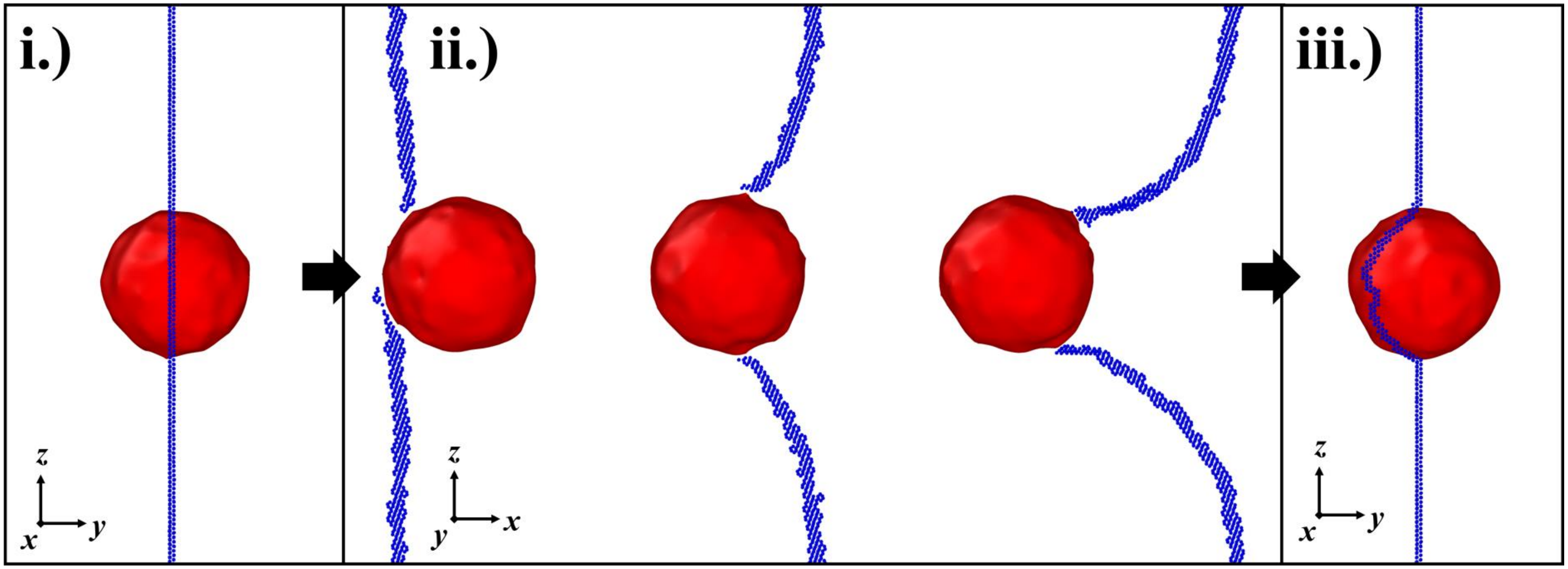

Figure 6.3. The standard evolution of an edge dislocation interacting with the NC is shown. As the evolution of the edge dislocation is similar in all diameters examined, the 6 nm NC is shown. i.) shows the starting structure and position of the edge dislocation, ii.) as the edge dislocation approaches and interacts with the NC over a few picoseconds, the velocity of the dislocation is hindered by the NC and at full speed away from the NC, and iii.) the effect of difference in speed of the edge dislocation is shown as the dislocation has climbed over the NC.

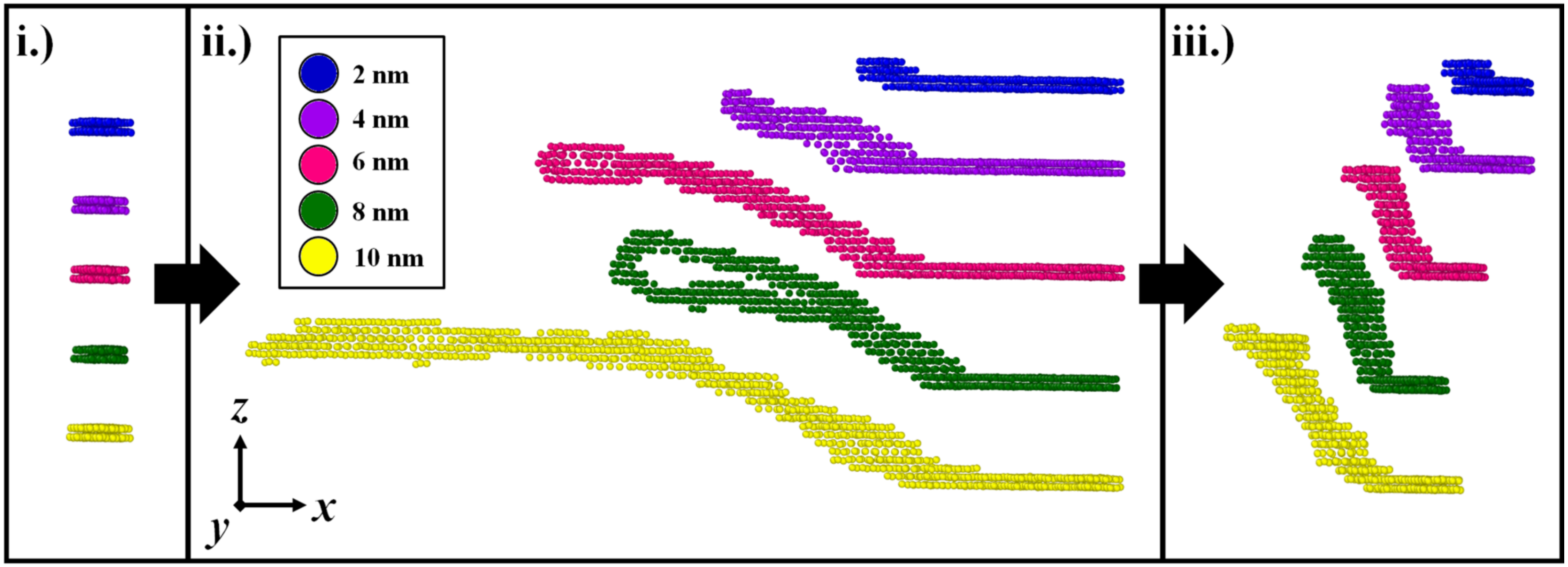

Figure 6.4. The evolution of the edge dislocation pre and post interaction with the NC based on diameter is shown. i.) shows the initial structure of the edge dislocation, ii.) shows the edge dislocation immediately after the dislocation has overcome the NC and the entire dislocation is within the NC, and iii.) shows the edge dislocation a few femtoseconds later as the edge dislocation has recovered.

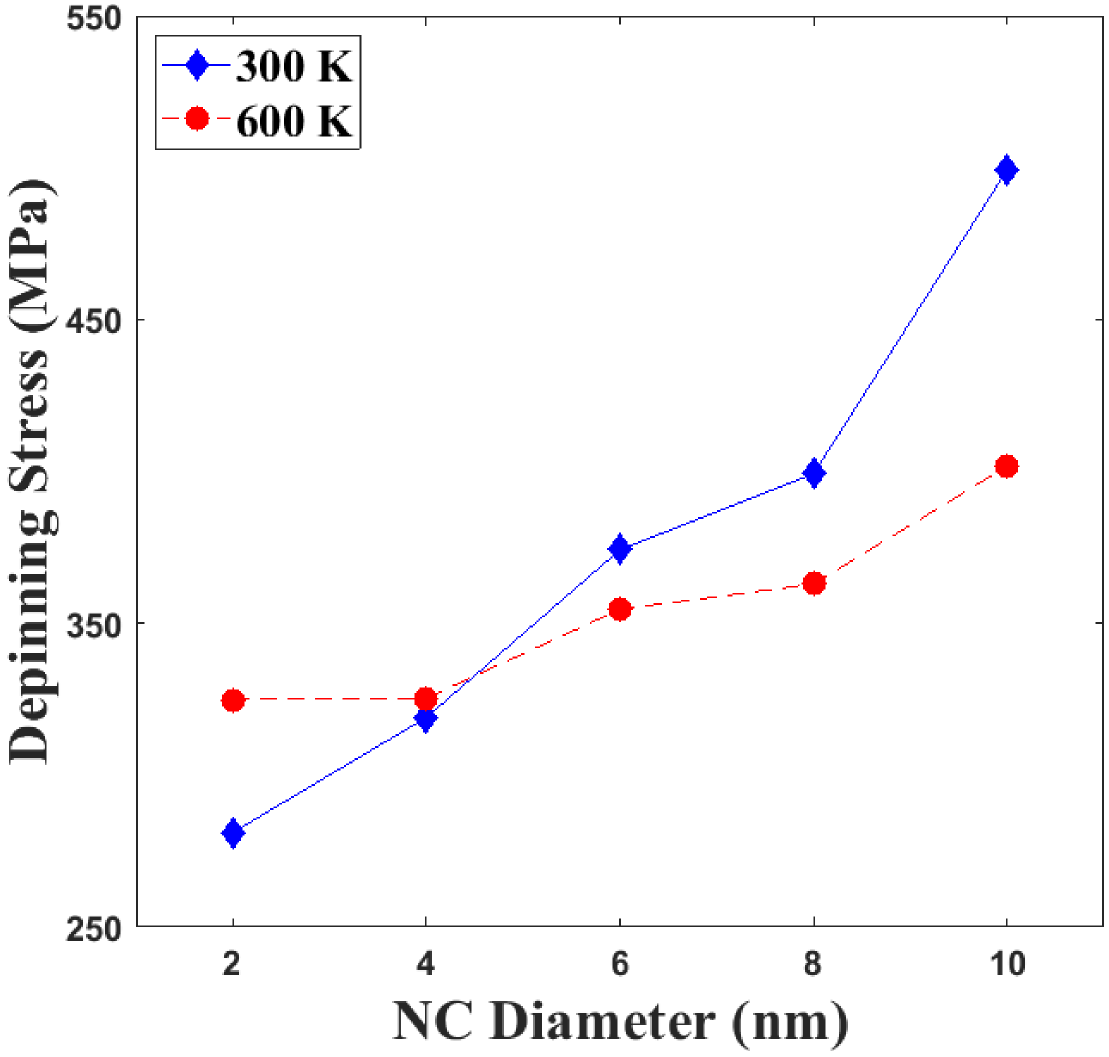

Figure 6.5. A plot showing the peak stress as the edge dislocation overcomes the NC as a function of temperature and NC diameter. (Solid Line) 300 K, (Dotted Line) 600 K.

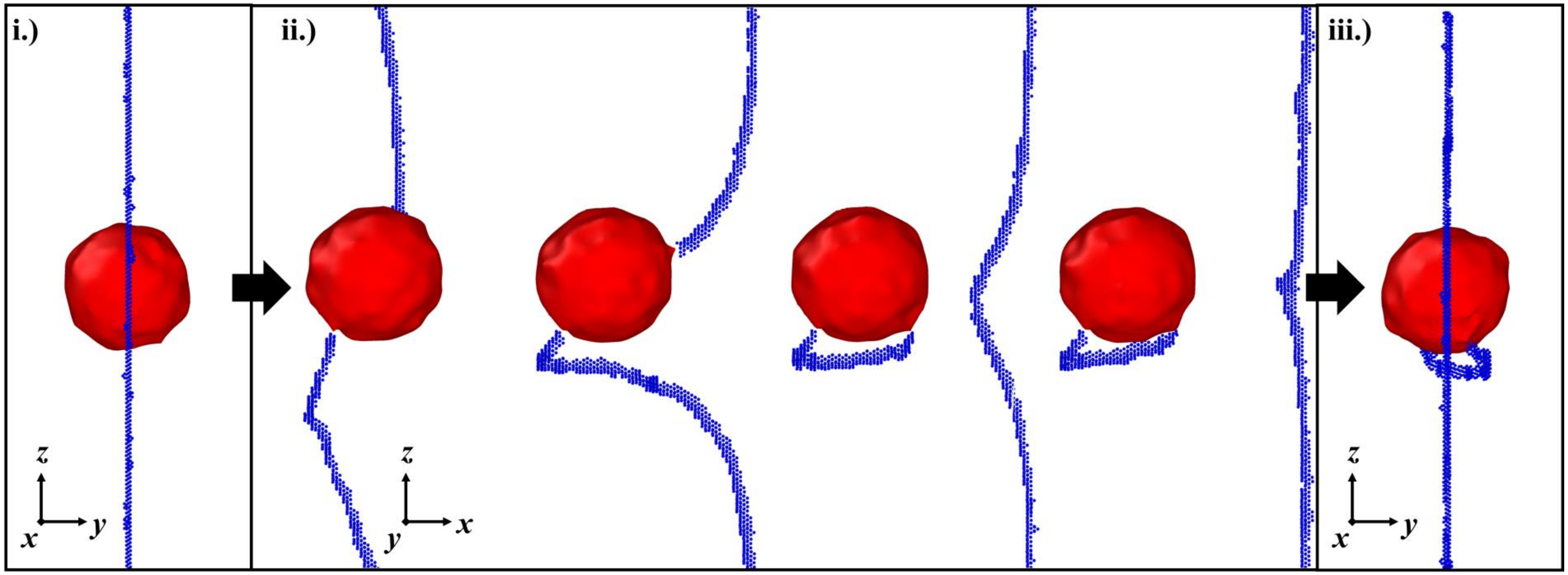

Figure 6.6. The evolution of the screw dislocation interacting with a NC is shown. All diameters examined in this study showed a similar response interacting with a NC, the 6 nm NC case is shown. i.) shows the starting position of the screw dislocation, ii.) shows the interaction of the screw dislocation with the NC, from left to right, the initial interaction with the NC, showing the formation of a kink, and to the evolution of the kink in the screw dislocation, and the formation of a dislocation loop within the NC as the screw dislocation is able to overcome the NC, and iii.) the screw dislocation after it is through the NC and has recovered its structure.

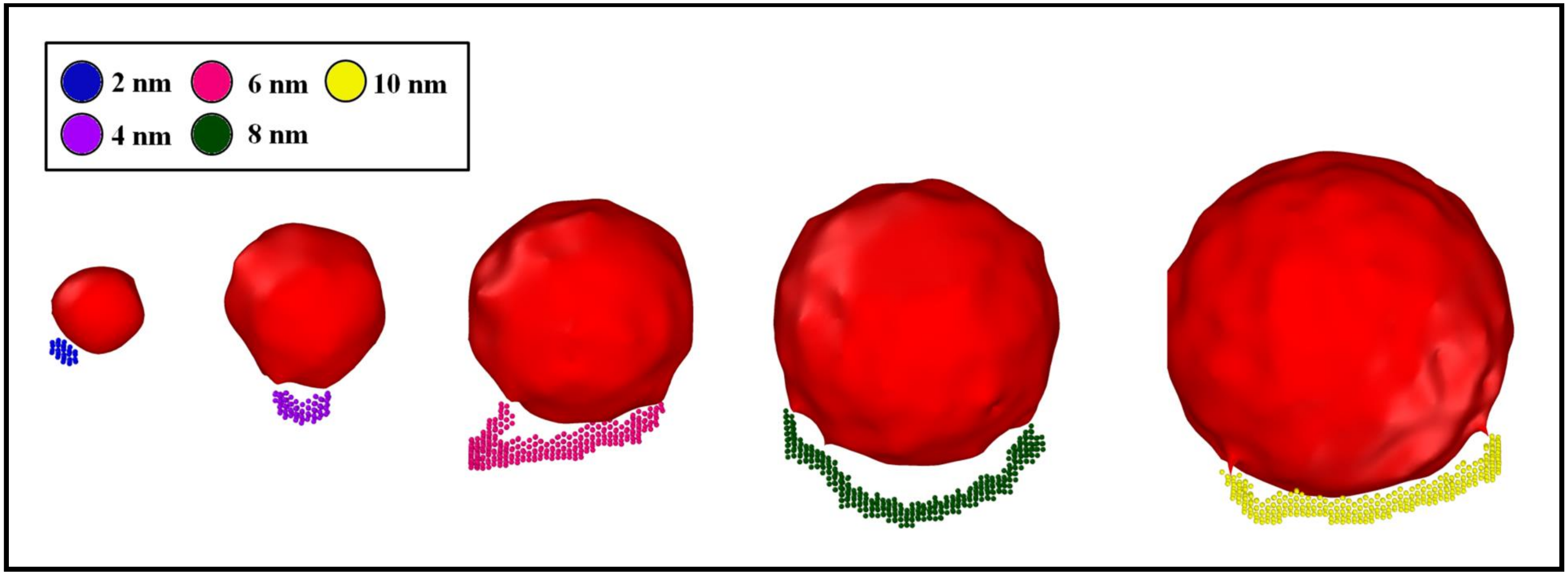

Figure 6.7. The effect of the screw dislocation with the NC is shown based on NC diameter size. As shown in these plots, unaffected by NC size, in the screw dislocation overcoming the NC, a section of atoms is trapped within the NC region. The size of the trapped atoms increases with increasing radii.

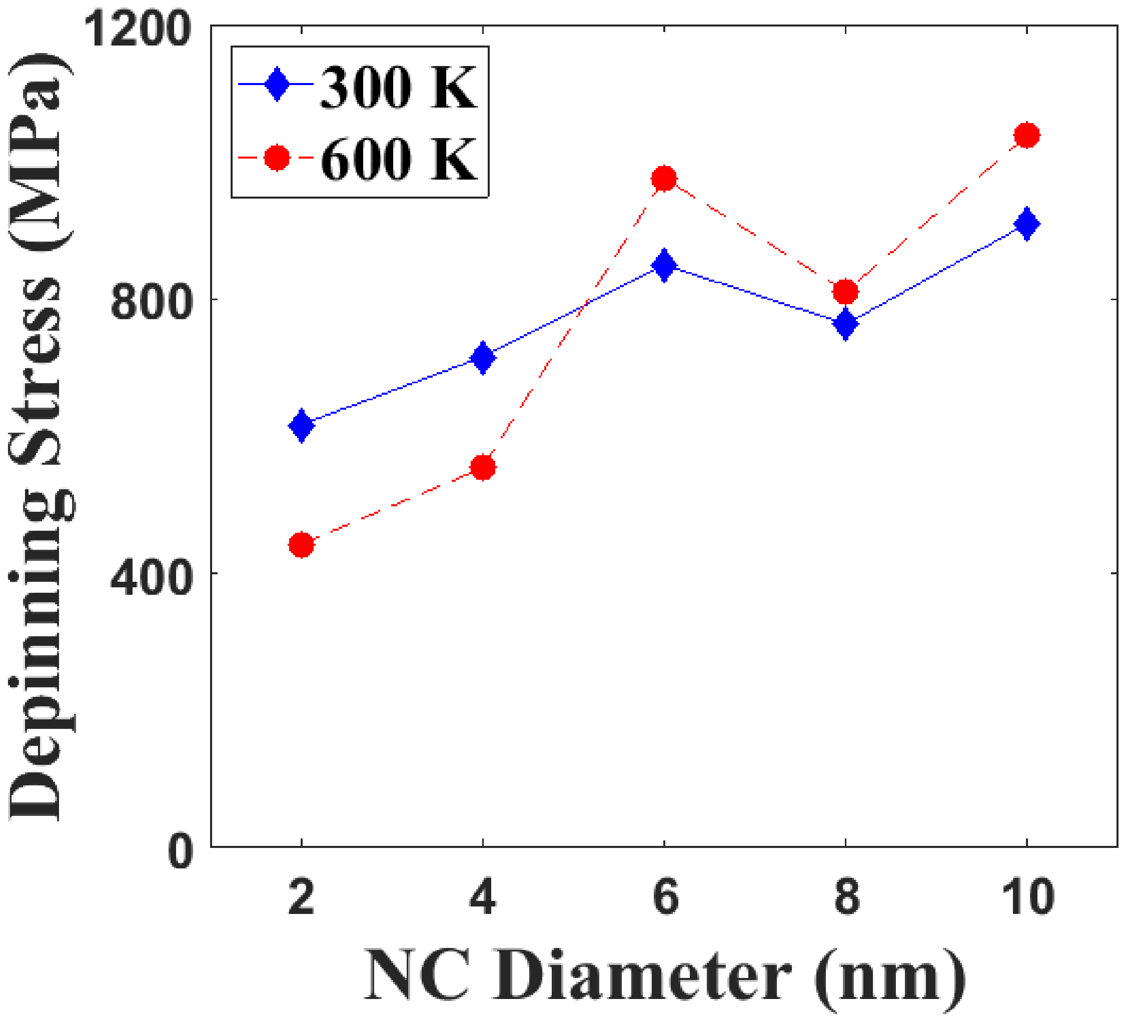

Figure 6.8. The depinning stress as the screw dislocation dislodges from the NC. (Solid Line) 300 K, (Dotted Line) 600 K.

Chapter 7 - Discussion

In this section, results obtained from the molecular dynamics (MD) and dislocation dynamics (DD) are going to be discussed. The first section will look at the structure of Y_2O_3 nanoclusters (NCs) in a bcc-Fe matrix, from MD. From there the affect these NCs have on the primary damage state of a cascade will be discussed. The affect the primary damage state has on the NC, along with the ability of the NC to change the development of damage within the Fe matrix. The next section will look at the depinning mechanism of NCs via edge and screw dislocations. As the NCs are able to pin the dislocations, having a system for defining the strength of the obstacles is the next step in understanding the strength of the NCs. From there the mobility of the edge and screw dislocation is inputted into DD to understand how NCs impact the strength of the material.

7.1 Structure of a Nanocluster

In chapter 4 of this dissertation, the structure of the NC is investigated using MD. These results showed that the NCs formed via a quench from 600 K to 0 K which created a NC structure that has a core-shell feature. However, for small NCs the entire NC is disordered, whereas at higher NC diameters the core-shell structure started to form. In figure 7.1, the disorder fraction of atoms, which is defined as a ratio of number of atoms in the disordered region to that of the structured core, is plotted on the left y-axis versus the diameter of the Y_2O_3 NCs. In figure 7.1 it shows that the NCs smaller than 2 nm are completely disordered. Along with showing the fraction of disordered atoms, figure 7.1 also shows the thickness of the disordered region for the 600 K annealing imposed on the NC on the right y-axis. The disordered thickness does not change significantly with increasing the size of NCs, and remains almost constant (roughly 0.5-0.7 nm).

The stress on the atoms in the NCs is independent of NC size, peaking in the shell and then quickly decreasing to a stable value in the α-Fe matrix. The similar stress profile for all diameters investigated seems to explain the constant shell thickness throughout the various sizes. In the high temperature annealing cases, 900 K, the thickness ranged from 0.7-0.9 nm, a slight increase from the 600 K annealing temperature, showing that with increasing annealing temperatures there is a growth in the shell thickness. Temperature does seem to have an effect on the shell thickness, but the time scale differences between a 15 ps MD simulation and a 2 hour real-time annealing make a 1 to 1 comparison very difficult to compare.

High-resolution high angle annular dark field (HAADF) characterization has been conducted to understand the atomic structures of the NCs, and to compare to the results obtained through MD simulations. HAADF is particularly used for NCs smaller than 5 nm in 9Cr-ODS. The contrast of HAADF imaging is sensitive to the atomic number and mass density[150]. NCs generally show darker contrast compared to the surrounding ferritic matrix because of the enrichment of the O elements. Figure 7.2 shows a typical Y_2O_3 NC with a diameter of 2 nm. High-resolution HAADF image is taken with the electron incidence parallel to the bcc $[111]_{matrix}$ direction. From figure 7.2, there is no distinct lattice structure has been observed in the NC, indicating that atomic species are randomly distributed within the cluster without forming a typical crystal structure, particularly at the core. According to previous studies, in an ODS alloy without Ti addition, the oxides generally tend to form larger Y_2O_3 NC, as compared with Y-Ti-O ODS. However, this study demonstrates that very small Y_2O_3 NCs can also be formed in 9Cr-ODS alloy without adding titanium to the matrix.

The Y_2O_3 NC in figure 7.2 displays faceted interfaces along low-index planes of the matrix. Similar faceting has been reported by Brandes in a Y-Ti-O ODS steel [150]. Brandes also found small nano-sized Y-Ti-O clusters which are amorphous as revealed from high-resolution TEM images [150]. Based on these observations, it is believed that the small Y-O NC in the present study probably appear to be amorphous, which is consistent with the simulation results. Figure 7.1 also shows that the disorder fraction decreases with increasing size of Y_2O_3 NCs. Since the thickness of the disordered region remains roughly the same, the number of ordered atoms increases with increasing size of Y_2O_3 NCs, causing a decrease in the disordered fraction. Figure 7.1 clearly shows that the core, the structured region, rapidly increases with increasing size when the diameter is larger than 2 nm. There exists a crossover from completely disordered NCs to a core-shell structure.

All of the particles, with a structured core, are surrounded by a disordered shell with a thickness between 0.5-0.7 nm, whereas the experiments have shown a shell thickness between 1-1.5 nm. The difference in thickness may stem from the fact that our current model does not include Cr and V, major elements, commonly found in the shell [103]. Without these elements in the simulations, there are less interactions for the O atoms and instead can only interact with the Y and Fe atoms. Although the shell of NCs is thinner compared to the experimental data, our data shows that the strain introduced on the NCs due to the mismatch between the Fe matrix and the NCs may lead to the formation of the shell, which is an energy preferred structure. At the boundary between the Y_2O_3 NC and the Fe matrix, the Fe atoms are slightly disturbed and off their lattice locations. These off-lattice atoms may increase the irradiation strength of these particles, by attracting the number of interstitial atoms, thus creating a protective sink. This phenomena is similar to grain boundaries and dislocations that act as a sink for defects [34], though the operating mechanisms are slightly different.

A TEM image of a 20 nm Y_2O_3 characterized by HAADF in figure 7.3(a) shows nano-sized oxides distributed in ODS matrix. High-resolution HAADF image in figure 7.3(b) clearly reveals a disordered shell between matrix and large Y_2O_3 particles, as demonstrated by FFT images in figure 7.3(c) for Y_2O_3, figure 7.3(d) for the disordered layer and figure 4.6(e) for the ferritic matrix. TEM observation is qualitatively consistent with the MD simulation, i.e. the Y_2O_3 NCs consist of a structured core of cubic Y_2O_3 surrounded by a disordered region, which cannot be identified as a particular crystalline structure. It should be noted that the thickness of the core shell of the 20 nm ODS particle is roughly 5 times as thick as calculated, which may be due to the segregation of impurities at the interface between the particle and matrix, leading to the increase of the core shell. The further study of impurity effect on the thickness of the core shell could clarify this issue.

In summary, MD simulations, backed by an experimental study showed that the structure of Y_2O_3 NCs in α-Fe showed a critical radius where the NC structure transitioned from completely disordered to a core-shell structure. The results show that Y_2O_3 NCs are disordered when their size is below 2 nm, while the larger clusters form a core-shell structure, with a thickness of 0.5-0.7 nm that is independent of their size. The structure of the NC has a clear crossover from the completely disordered NCs to core-shell structures. TEM images also demonstrate the crossover from disordered NCs to core-shell structures, and the results are qualitatively consistent with the MD simulations. Although the thickness of the disordered shell is smaller compared to the experimental data available, these results provide the atomistic-level understanding of Y_2O_3 NCs structures in α-Fe. It is expected that a slight disturbances in the Fe atoms surrounding the Y_2O_3 particles may further increase the irradiation strength of these particles, thus increasing irradiation resistance.

7.2 Primary Damage State of a Cascade near a Nanocluster

The radiation stability of NCs in ODS steels has been a major area of research for some time. Many neutron and ion irradiations have been conducted to further understand this phenomenon; however, these results have been inconclusive, due to various material compositions, consolidation techniques, and irradiation conditions[13]. The results obtained in the present simulations may help shape the understanding of how NCs affect irradiation resistance. Our results show that with increasing PKA energy, the energy interacts with the NC in various ways. At low energies, the cascade energy ricochets off the NC and stays on one side. For the 10 keV cases, the energy is able to penetrate through the NC. There are a few key aspects to the inclusion of a NC.

7.2.1 Point Defect Population in the Fe Matrix

MD simulations of cascades in α-Fe with a NC have consistently shown fewer displaced atoms created at the end of a cascade compared to the standard empirical models[15,24,25,93]. In comparing the results of a pure α-Fe system to that of the α-Fe NC system, the number of defects within the Fe matrix is dependent on quite a few characteristics: NC diameter, PKA energy, defect type, and PKA shockwave volume. The Fe matrix with a NC has a small drop in the number of vacancies compared to a pure Fe system. The small drop in vacancies is shown for all PKA energies and NC diameters, the drop increasing with NC diameter. In the case of interstitials, the NC diameter played a larger role. The 2 nm NC sees the interstitial increase with PKA energy and at 10 keV PKA energy there is no difference between the 2 nm NC system and a pure Fe matrix.

The lack of difference between a 2 nm NC and a pure Fe matrix at 10 keV shows the importance of the ratio of the volume of the shockwave to that of the NC. This ratio is an important aspect of a NCs impact on the Fe matrix in ODS steel. Figure 5.3 shows a standard cascade in a Fe matrix. The key aspect of the cascade is that the shockwave consists of an outer layer of interstitials and an inner sphere of vacancies. As the 2 nm NC is smaller than the shockwave, the interstitials created along the boundary of the shockwave are not affected by the inclusion of a NC. As some PKA energy is still transferred to the NC versus the Fe matrix, a drop in the total number of point defects is still visible for the 2 nm NC. The key aspect of the damage reduction in the Fe matrix is based on the ratio of the volume of a standard shockwave in pure Fe to the volume of the NC. In comparing the ratio of the volume of a NC to the average volume of a 10 keV shockwave, respectively for the 2 nm, 4 nm, and 6 nm, the ratios of the volumes are 0.1, 0.7, and 2.3.

In looking at the values of the ratio of the volumes, the 2 nm's defect production efficiency is very interesting. In the case of the interstitials with increasing PKA energy the defect production efficiency becomes identical to the pure Fe system. As the 10 keV PKA shockwave is able to completely encapsulate the 2 nm NC, the shell of interstitials occurs unaffected in the Fe matrix, causing the 2 nm NC to have the same defect production efficiency as the pure Fe matrix for Fe interstitials. For the larger NCs, the 4 nm and 6 nm diameter NCs, the significant difference is seen between the interstitial populations within the Fe matrix. The 6 nm NC has a slight decrease in the number of interstitials defect production efficiency to the 4 nm, but the same defect production efficiency for vacancies. The ratio between the NC and the shockwave is very important in limiting the amount of damage within the Fe matrix.

Defect production efficiency is a common parameter in describing and comparing the primary damage state of a cascade in MD. Defect production efficiency is defined as the ratio of the surviving number of Frenkel pairs to the number of displacements predicted by the Norgett-Robinson-Torrens formula (NRT)[151]. Equation 7.1 is used to calculate the remaining number of Frenkel pairs based on the NRT model. Where E_d is the average threshold displacement energy, a value of 40 eV is used for Fe following the standards introduced by the American Society for Testing and Material (ASTM)[152] and E_{PKA} is the energy of the PKA.

$$\nu_{NRT} = \frac{0.8E_{PKA}}{2E_d} \qquad \text{(Eq. 7.1)}$$

The defect production efficiency is plotted versus PKA energy in Figure 7.4. The introduction of a NC in the Fe system is dependent on NC diameter, PKA energy, and defect type. For vacancies, there is a significant drop at lower energies for all three NCs in this study. However, at PKA energy of 10 keV only the 6 nm NC shows a drop in vacancy point defect production efficiency. In the case of interstitials, however, the 2 nm NC behaves unlike the 4 nm and 6 nm NCs. With increasing PKA energies, from 1 keV to 10 keV, the defect production efficiency increases with increasing PKA energy, at 10 keV the 2 nm NC has the same ratio as a pure Fe matrix. The 4 nm and 6 nm NC significantly decrease the interstitial ratio at all three PKA energies. The difference in interstitial ratio between the 2 nm and the larger NCs is due to the volume ratio of the displacement shockwave to the NC. As the 2 nm NC is similar in size to a 10 keV shockwave, the effect of the NC on the Fe matrix is completely diminished for interstitials.

7.2.2 Fe-Nanocluster Boundary

Four major theories have been proposed as controlling NC evolution due to irradiation: ballistic dissolution and irradiation-enhanced, homogeneous nucleation leading to either Ostwald ripening or inverse Ostwald ripening[13]. Further experimental research has shown that the interfacial energy between the Fe atoms and the NC plays a key role in the evolution of the NC. The results in this study demonstrate that the cascade acts in two major ways dependent on PKA energy:

1) At low energies, the PKA interaction with the NC is a hindrance to the shockwave's growth, with the NC forcing the shockwave to occur earlier than in a NC free system, thus the NC causes less Fe defects within the matrix.

2) At higher energies, 10 keV PKA energy, the cascade energy is able to penetrate and transfer through the NC, causing the standard shockwave to be broken up into two tiny shockwaves on different sides of the NC.

All of the theorized concepts for NC evolution via irradiation occur over a significantly larger time scale than anything that is possible in MD. However, it is possible to understand precursors that could corroborate a potential long-term mechanism. Independent of PKA energy, there is an amorphization of the NC at all PKA energies, with the amount of disorder increasing with increasing PKA energy. Interfacial energy plays a key role in creating efficient point defect sinks[153]. In comparing the amount of disorder caused by a cascade, the fraction of atoms in the NC displaced increases with decreasing radii. The NC disorder, caused by the cascade, reaches a plateau level during the relaxation process of the displacement cascade, with the plateau occurring over longer periods of time for increased NC radii.

The Fe defects surrounding the NC over the course of the simulation show that during the primary damage state of a cascade, the formation of a defect sink is occurring at the Fe matrix-NC boundary. In furthering the understanding of the sink formation along the NC boundary, cluster analysis is used to look at the clustering in this region. Figure 7.5 shows the average number of vacancy and interstitial clusters in relation to the surface area of the NCs. Unlike the Fe matrix, where little to no clustering occurs, the Fe atoms interacting with the NC cause a significant amount of clustering around the NC. The cascade increases the irregularities along the Fe-NC interface, causing a sink to form at the NC boundary. Within the primary damage state, as shown in Figure 7.6 the population of defects at the NC boundary is biased towards the Fe interstitials.

A key mechanism that has been backed by experimental evidence is Ostwald ripening of the NCs[13,154]. Ostwald ripening is the combination of the above phenomena and can either occur with large NCs breaking up into smaller NCs or the dissolution of small NCs leading to an increase in the average size of NCs and a decrease in number density. In the MD results, there are three major factors that suggest the 2 nm NC is more likely to dissolve compared to the larger NC.

1) The 2 nm NC has significantly more amorphization than the 4 or 6 nm NCs. Although no Y and O atoms are able to enter the Fe matrix during the primary damage state of a cascade, it is more likely that, with increased amorphization and over much larger time scales, diffusion and ballistic dissolution of NCs is possible, with the more disordered NCs likely to dissolute.
2) The higher fraction of Fe antisites within the 2 nm NC compared to the 4 and 6 nm NCs suggests that over an extended period of time where many displacement cascades are interacting with NCs, the 2 nm NC will be dissolved at a much faster rate.
3) In comparing the volume of a shockwave to the volume of a NC. The 2 nm NC is the only NC diameter is this study that is completely encapsulated by a shockwave, having a volume one tenth of a 10 keV shockwave. As 10 keV is a common PKA energy in reactors conditions, this suggests that the tiny NCs will experience ballistic dissolution over larger time scales.

The MD results shown here help to corroborate that the smaller NCs are more likely to dissolve via ballistic dissolution in comparison to the larger NCs. Based on the fraction of antisites within the NCs and the fraction of disorder within the NCs, the 2 nm NC has a significant increase in damage compared to the 4 nm and 6 nm NCs, suggesting that over the course of many dpa, the tinier NCs will dissolve at a faster rate. The MD simulations here are unable to see growth in NCs as only one NC is within each simulation and migration of defects would occur over much longer timescales. However, ballistic dissolution is a key part of Ostwald ripening, and the results shown may indicate that over the course of many dpas worth of damage that Ostwald ripening may be a key mechanism in long term evolution of NC number density and average NC radius.

7.2.3 Nanocluster Irradiation Resistance during the Primary Damage State

In comparing the three NCs, all three of the diameters in this study show varying degrees of the same characteristics. In terms of cascade morphology, two common traits are observed, as described above. At low energies, the introduction of a NC causes a single shockwave to occur along the NC boundary, with the peak defect population decreasing with increasing NC diameter. At 10 keV, the cascade is able to transfer energy through the NC, causing two shockwaves to occur on opposite sides of the NC, with a significant decrease in the Fe defect population, which decreases further with increasing NC radii. In looking at the amount of defects remaining in the Fe matrix at the end of the simulation, the 4 nm and 6 nm equally outshines the 2 nm NCs ability to hinder Fe defects in the Fe matrix. The 2 nm NC is too small, such that the PKA energy is easily transferred through the system, causing the NC to absorb very little of the PKA's energy in comparison to the larger NCs. Although only relatively low PKA energies are investigated in this study, a key aspect is shown with the 2 nm NC. When a cascade shockwave is larger in size compared to a NC, the NC's ability to decrease the amount of point defects in the NC and in the Fe matrix is greatly reduced during the primary cascade damage state.

The next similarity is in the formation of a defect sink surrounding the NC. The population of interstitial to vacancy populations is found to be independent of PKA energy and NC diameter with a value of 1.3, preferential towards interstitials. Along with having a similar ratio of defect populations, the NCs also have a very similar distribution of Fe defect clusters surrounding the NC, although the 2 nm and 4 nm NCs have a slightly higher concentration of Fe defects surrounding the NC compared to the 6 nm NC. In further analyzing the Fe interstitials, Fe antisites within the NC play a key role in the structural stability of the NC during a cascade. In a pure population sense, with increasing NC diameter, the amount of antisites significantly increases with increasing radii. In taking into account this fact, a better evaluation method is the fraction of NC lattice sites replaced with Fe atoms. This fraction increases significantly with decreasing radii. In comparing the population of defects surrounding the NCs, the 4 nm NC outshines both the 2 nm and 6 nm NCs, with a similar point defect population to the 2 nm NC and significantly smaller fraction of Fe antisites within the NC.

The next issue of interest between different radii is the evolution of the NC structure. Again, all three cases show a certain level of amorphization within the NCs, which increases with increasing PKA energy. With the severity of the amorphization increasing with decreasing radii, along with high amounts of amorphization, the NCs have an increased population of vacancies compared to interstitials. This increase is vacancy population is due to the inclusion of Fe antisites within the NC, easily pushing the O atoms off of their lattice sites. In taking into account the structural changes of the NC, the major difference is in the fraction of amorphization. As discussed in the previous section, an irregular boundary between atoms creates a strong point defect sink. In combining the information about the surrounding Fe atoms and the structural changes in the NCs, the 4 nm NC again outshines the other two diameter NCs, with the 2 nm NC likely disappearing over longer time periods due to Ostwald Ripening, and the 6 nm NC having a smaller concentration of defects surrounding the NC.

Many features go into choosing an ideal NC diameter for ODS steels, with the goals of increasing the irradiation resistance and overall strength of the base material. In this study, the primary damage state of a cascade for NCs at 100 K is shown. comparing the effect the size of a NC has on the primary damage state of the cascade a few key attributes that are a factor in all three NC diameters in this study: Fe atoms migrating towards the NC over the course of the simulation, the formation of a defect sink at the Fe-NC boundary, and the amorphization of the NC structure. The key trends shown for point defect evolution in the Fe-NC system based on NC diameter:

- The ability for the NCs to significantly decrease the remaining population of Fe defects in the matrix is ultimately a factor in the volume of the shockwave compared to the volume of the NC, with the remaining number of defects decreasing with a decreasing in the ratio of shockwave to NC volume.
- The smaller NCs tended to have a higher concentration of Fe defects surrounding the NC, such that with decreasing radii the population of point defects surrounding the NC is optimized
- Amorphization of the NCs is seen in all three NC diameters, with the disorder increasing with decreasing radii. This phenomenon suggests that over longer time periods Ostwald ripening may be a key factor in the dissolution of smaller NCs

7.2.4 Temperature Effect on Nanocluster Irradiation Resistance

In the case of a pure Fe matrix, the affect temperature has on the evolution of the primary damage state has been heavily investigated[15,16] . The studies have shown that temperature has a small effect on the number of point defects created during the peak damage state of a cascade; however, as the damage from the cascade is transferred, the final number of Frenkel pairs is nearly identical for ranges of temperature from 10 K – 1000 K[15,16]. The introduction of a NC has shown to significantly change the number of point defects surrounding the NC, along with creating a defect sink near the NC interface.

In the case of temperature in many cases the amount of point defects in the system is independent of temperature. However, in a few of the cases simulated in this study, temperature did have an effect on the number of point defects within the system. The Fe matrix itself is largely unaffected with temperature, as expected based on the many studies published looking at the affect temperature has on point defect from a cascade. Along with the Fe matrix, the fraction of antisites that have been shown to play a large role in the creation of the point defect sink created at the NC boundary. Within standard deviation there is no difference to the number of point defects within the Fe-NC interface region, suggesting that at all temperatures investigated the creation of a point defect sink occurs.

The only way temperature seemed to affect the damage state of the surrounding Fe-NC system is in the case of the NC itself. At higher temperatures 1 keV PKA are able to migrate further in the system and have a bigger effect on the disorder within the NC. In the 600 K case both the 2 nm and 6 nm diameter NCs saw a noticeable increase in the amount of disorder within the NC. This increase in disorder is still smaller than the disorder at higher PKA energies. However, this indicates that in a real situation at higher temperatures it is likely that the NCs will be affected by minor interactions with PKA energies. Ballistic dissolution of NCs is enhanced with increasing temperature.

7.3 Dislocation – Nanocluster Interactions

Two key aspects of dislocation-NC interactions are shown: the first is on the depinning mechanism as a function of temperature, NC diameter, and dislocation type, and the second is looking at the stress required to overcome the NC. The stress required to overcome the obstacle can be used to calculate an obstacle strength parameter to determine the affect temperature and NC diameter have on the obstacle strength. Understanding the depinning mechanism of the dislocation from the NC plays a key role in understanding how these NCs strengthen the base F/M steels.

7.3.1 Edge Dislocation Depinning Mechanism

In computational studies there have been two key methods that control the depinning mechanism of an obstacle: Orowan and climbing[49,133]. In the case of ODS steel experimentalists have believed that both Orowan and climb play a key part in the depinning mechanism of dislocations from NCs[134,155–158]. Experimental studies have shown that the hardness of the NCs force the dislocations to climb over the NC via cross-slip. The depinning mechanism for edge dislocations interaction with Y_2O_3 NCs is controlled by both of these methods: velocity of the edge dislocation near the boundary and the climbing mechanism via cross-slip of the edge dislocation segment around the NC.

The major feature that controls the depinning mechanism is the velocity of the dislocation. As the velocity of the dislocation directly controls the affect the climb mechanism has on the depinning stress of the NC. At the lower temperature case, 300 K, the velocity of the dislocation is 625 m/s in the pure Fe matrix, compared to 500 m/s in the 600 K simulation cell. The effect climb has on the depinning stress noticeable drops at the higher temperature. This change in velocity, i.e. a change in temperature, has profound effects on the stress required to overcome the NCs. A fact, which is evident in figure 6.5, as with increasing diameter the amount of stress required in overcoming the obstacle increases for the edge dislocation simulations in the 300 K case, but in the 600 K case the required stress has a smaller change with increasing diameter.

In the case of the edge dislocation the mechanism that controls the depinning mechanism is a combination of both mechanisms described above: Orowan and climbing. As the edge dislocation becomes pinned along the NC, the edge dislocation becomes to bow around the NC, as the bowing continues to grow and the stress builds up, the edge dislocation pinned along the NC begins to cross-slip along the Fe-NC interface and climb over the NC outer diameter until it is able to free itself over the NC. At this point the edge dislocation is able to free itself from the NC. The change in temperature of the system has a notice effect on the climbing mechanism. At higher temperatures it is easier for the edge dislocation to overcome the NC, as the temperature to glide through the system is noticeable less. Temperature plays a key role in the importance the climb mechanism has on the stress required to overcome the obstacle. The Orowan is standard in both the 300 K and 600 K cases. The ability for edge dislocations to become pinned and the depinning mechanism controlled by a combination of climbing and Orowan mechanisms, explains how NCs impact the base strength of ODS steel, as this depinning mechanisms forces the dislocation to become pinned and significant increases in the stress field to overcome the obstacle.

In both temperature cases, the dislocation structure is changed after interacting with the NCs. As the dislocation becomes free of the NC structure, the immediate response is a whiplash effect as the segment of the dislocation previously lodged behind the NC is now freed and the forces acting on it cause it to quickly, over the course of 3 picoseconds, return the edge dislocation to the new most energy efficient structure. This new energy efficient structure of the dislocation includes the original dislocation structure along the starting plane and now connected to a segment sitting on a new X-Z plane based on the size of the radii of the NC.

7.3.2 Screw Dislocation Depinning Mechanism

In comparing the mobility of the two types of dislocations: edge and screw, there is a noticeable difference. The key difference is in the mobility of the two types of dislocations within the Fe matrix. The edge dislocation once a threshold stress is reached will move continuously throughout the matrix, at lower applied stresses and higher velocities. However, in the case of the screw dislocation, along with requiring a significantly higher stress to start moving, the screw dislocation moves via kinks along the dislocation segment at a velocity an order of magnitude slower in comparison: with the screw dislocation moving at a velocity of 32.7 m/s in the 300 K case and 40.7 m/s in the 600 K case. The difference between the mobility of the dislocations plays a key role in the depinning mechanism.

As the screw dislocation is pinned along the NC, the stress along the system continues to grow. Over the course of being pinned, the screw dislocation starts to bow around the NC. In the case of the screw dislocation however, one key difference occurs when the screw dislocation becomes pinned along the NC. Unlike the edge dislocation which overcomes the NC by a combination of bowing and climbing, the screw dislocation overcomes the NC by bowing and kink motion. As the screw dislocation continues to bow, a kink starts to form along the screw dislocation line. Unlike the kinks in the Fe matrix, this kink is combined with the Orowan mechanism as the screw dislocation is attempting to move through the NC.

The screw dislocation has no climb mechanism and is completely controlled via the Orowan mechanism. However, the process is conflated by the kink movement in the screw dislocation. In the case of the depinning mechanism for screw dislocations, the Orowan mechanism in this case needs to overcome both the dislocation and the kink. As the bow continues to grow, it is able to become unpinned from the NC. As the screw dislocation escapes the NC, the kink formed during the interaction remains as a dislocation loop in the NC, and the screw dislocation exits the NC and after leaving the

NC returns to the original structure of the dislocation, the screw dislocation is able to quickly recover to its original structure.

With increasing diameter, the dislocation loop formed within the NC increases in size. The temperature of the simulation box has a smaller effect compared to edge dislocations. As the speed of the screw dislocation is less affected by the change in temperature of the simulation box. The lower change in velocity is based on the increased stress required to move the screw dislocation. As the 300 K has a velocity of 40.2 m/s and the 600 K case had a velocity of 32.7 m/s. For the smaller NCs, 2 nm and 4 nm diameters, the strength to overcome does decrease with increasing temperature. However, for the larger NCs, 6 nm, 8 nm, and 10 nm the applied stress required overcoming the NC is nearly identical.

7.3.3 Obstacle Strength

The NCs act as pinning sites for dislocations moving in the α-Fe matrix. By pinning dislocations within the matrix, NCs are able to strengthen the base metal alloy. In relating the yield strength of a material to discrete microstructural features the dispersed barrier hardening model uses the following expression[159]:

$$\Delta\sigma_{y,i} = \alpha_i M \mu b \sqrt{N_i d_i} \quad \text{(Eq. 7.2)}$$

In this equation, the yield strength is based on two key aspects: the geometry of the metal and the microstructural feature's qualities. The geometry features include M, the Taylor factor, μ, the shear modulus, and b, the Burger's vector. The microstructural features consists of its N_i (number density of feature type i), d_i (average diameter of microstructural feature i) and $\alpha_{i,}$ barrier strength of the microstructural feature, which is a coefficient between 0 and 1. A feature that has a low α coefficient is considered a weak obstacle and dislocations are able to more easily bypass these obstacles. On the other hand, microstructure features that have α coefficient close to 1 are strong obstacles and significantly hinder dislocation motion.

A major issue experimentally is measuring the unique α of individual microstructure features in a complex metal or rather separating α of the different microstructural features. In order to solve this problem, mathematical equations have been developed to model α coefficient for various microstructural features within a material. These equations are based on geometric features of the base material and the number density and average size of the microstructural feature. Although these equations exist for the individual microstructure types, for each material it is a very difficult task in correctly weighting each microstructure features' α value to one another as α is influenced by many sample-specific characteristic in the case of a NC: composition, coherency and size are key parameters to take into account.

Many studies have used the dispersed barrier hardening model due to its ease. However, the model has problems in determining the effect individual defect structures have on the strength of a base alloy. Equation 7.2 is derived from the following classical equation based on the critical shear stress required for a dislocation to overcome the cross-section of an obstacle:

$$\Delta\tau = \mu b\, cos\, (\emptyset_c/2)/(L - d) \tag{Eq. 7.3}$$

In this equation, the critical shear stress, $\Delta\tau$, is a function of the critical breaking angle, Φ_c, the burger's vector, b, the shear modulus μ, and the effective obstacle spacing, (L-d), which can be compared to $(N_x d_x)^{-1/2}$ in a three-dimensional array.

In calculating the obstacle strength for the NCs based on the MD results, a modified version of equation 3 is used:

$$\alpha = \frac{\Delta\tau(L - d)}{\mu b} \tag{Eq. 7.4}$$

In this equation, α is the cosine of the critical angle, seen in equation 7.3, hence a unit-less value that describes how strong an obstacle is. $\Delta\tau$ is the increase in shear stress from the obstacle. $\Delta\tau$ is obtained via taking the difference of the stress as the dislocation overcomes the NC and the friction stress, as the dislocation moves in an obstacle free simulation cell. L is the length of the dislocation and d is the diameter of the NC. μ is the shear modulus of the material and b is the Burger's vector. The shear modulus calculated using the pure Fe system is 70.75 GPa. Key characteristics required for equation 7.4 are shown in table 7.1.

7.3.3.1 Obstacle Strength for Edge Dislocations

The key parameters in calculating α are shown here. In the case of the edge dislocation the Burger's vector is 2.47 nm. The glide stress is dependent on the temperature as the glide stress increases with increasing temperature; at 300 K the glide stress is 129 MPa and the glide stress at 600 K is 148 MPa. Figure 7.7 displays α calculated for the NCs as a function of temperature, and dislocation type based on equation 4. The large blue box is the region of α values experimentally measured via a TEM straining[134]. The TEM straining measured α values between 0.3 and 0.8 for NC diameters between 4 nm and 10 nm. In looking at the 300 K edge dislocation α values, in the lower temperature case, 300 K, NC diameter plays a larger, more important role compared to higher temperatures. As at 300 K, with increasing diameters, the calculated α shows a large fairly linear increase. At the higher temperature case, 600 K, the diameter played a much smaller role, as α is fairly equal for all NC diameters in this study.

The change in α with increasing temperature is related to two key aspects of the edge dislocation. The aspects that affect α are the base speed of the dislocation and the climbing mechanism. The key difference in the 300 K and 600 K cases for the dislocation is the base speed of the dislocation. With increasing temperature the average speed of the NC decreases, hence at higher temperatures the affect climb has on the dislocation decreases, as the speed required for the edge dislocation to move within the Fe matrix decreases the Orowan mechanism controls the depinning process more at higher temperature. This shows that at higher temperatures α becomes independent of NC diameter and suggests that the smaller NCs have a greater effect on the overall strength of the material in response to edge dislocation mobility.

In comparing α measured in the TEM straining to that of the α calculated for the edge dislocation, the α of the edge dislocation is closer to the lower limit measured in the experimental study. As the edge dislocation has a much higher mobility, logically the α of edge dislocations would be lower as compared to the screw dislocation; however the TEM results help to corroborate the results in this study. Several of the cases in this study are allowed to have multiple interactions with the NC. Although the edge dislocation had the climbed structure from its first run with the NC, the new structure still had the same required stress to overcome the NC. In the case of the climb structure, it is unaffected by multiple runs with a NC, as the climb from the first run is maintained with multiple interactions with a NC.

In taking into account actual conditions of a reactor and the benefit of ODS steels over F/M steels has been that at higher temperatures these materials tend to outperform the base alloys due to the inclusion of NCs. The results obtained for edge dislocations indicate that at higher temperatures, NC diameter no longer plays a key role in the strengthening of the material, but rather the strength of the material is based on the inclusion of NC of any size. This indicates that having a population of small NCs is ideal as smaller NCs would take up a smaller volume of your material and still give the same amount of strength to the base material.

7.3.3.2 Obstacle Strength for Screw Dislocations

The key parameters of the screw dislocation for inputting into equation 6.4 are as follows: the Burger’s vector is 2.47 nm, and the shear modulus is 70.7 GPa. The glide stress of the screw dislocation is based on temperature; in the 300 K simulation box the glide stress is 133 MPa and in the 600 K simulation box the glide stress is 151 MPa. In comparing the glide stresses of the two types of dislocations, the results are very similar, with the glide stress of the screw being slightly higher than those of the edge dislocation. As the movement of the screw requires more force via the movement of kinks, the slight increase makes sense.

In the case of the screw dislocation, figure 7.7 shows that α is more independent of temperature, as the basic trend of increasing with increasing radii is shown to occur for both the 300 K and 600 K cases. For the smaller NCs, 2 nm and 4 nm diameters, α decrease with temperature, as the temperature of the simulation box increased the stress required to overcome the obstacle decreased. However, for the larger NCs, 6 nm and above, α is unaffected with temperature. A key difference between the screw dislocation and an edge dislocation is in the velocity of the dislocations at the applied stresses.

In comparing the TEM measured α to that of the calculated α for the screw dislocation, α of the screw dislocation is near the upper limit of the measured α from the TEM study. This indicates that the key strengthening mechanism of the NCs is in their ability to hinder the movement of screw dislocations within the bcc-Fe matrix. Along with the TEM study indicating that they saw no climbing of the dislocations around the NCs, this is also an indication that it is likely that screw dislocations are the major type of dislocation investigated for this study and a key aspect for the strengthening of the base bcc Fe matrix.

Although the glide stresses of the two systems as shown in Table 2 are very similar; the velocities of the two types of dislocations are very different within the Fe matrix. As the velocities of the screw dislocation is 40.2 m/s at 300 K and 32.7 m/s at 600K in comparison to the edge dislocations velocities of 625 m/s at 300 K and 500 m/s at 600K. The velocities of the screw dislocation are an order of magnitude smaller than the edge dislocation. Based on the lower velocity of the dislocation, the velocity of the screw dislocation being so similar as compared to the edge dislocation explains how α is more similar at the various temperatures for the screw dislocation in comparison to the edge dislocation’s α. The Orowan mechanism is in control of the movement of the NC.

7.4 Closing Remarks

In this discussion section three key areas have been discussed separately, the structure of the NC, the change in structure due to the interaction with a cascade, and the interactions a NC has with edge and screw dislocations. In the case of the interactions with the primary damage state of a cascade, the key characteristic to take into account is the volume of the cascade during the shockwave stage and the volume of the NC. In the case of the 2 nm NC when the shockwave is larger in volume, the effect this NC has on the amount of damage within the Fe matrix is decreased. With the cascade simulations, it came to a point where the key characteristic to be taken into account is the ratio of the volume of the shockwave to that of the NC.

Over the course of the primary damage state the number of interstitials increased along the boundary, leaving the NCs surrounded by a point defect sink primarily comprised of interstitials. This suggests that over further interactions with point defects and just the general trend of defect migration, which NCs act as point defect sinks during the radiation damage sequence. Along with this change to the boundary region, another key aspect is the disordering or amorphization of the NCs. The NCs are unable to retain their structure during the primary damage state of the cascade. This fact suggests that ballistic dissolution plays a key role in the change in number density and average radii of NCs seen during radiation experiments on actual ODS steels. The amorphization however, did not lead to any atoms dislodging from the NC, suggesting that multiple interactions would have to occur for the NCs to become fully dissolved.

The overall trend is that the 4 nm NC outperforms both the 2 nm and 6 nm NC in the case of the cascade study.

In terms of the dislocation depinning mechanism, the type of dislocation played a large role in the depinning action. In the case of the edge dislocation, temperature played a larger role in the strength of the NCs. As the dislocation is able to move with less force at higher temperatures, the key difference is the amount of stress needed to overcome the climbing mechanism decreases with temperature. At 600 K the obstacle strength of the NCs is fairly equal and independent with NC diameter. In the case of the edge dislocation the obstacle strength suggests any size would do as good a job as any, suggesting having a smaller average radii would greatly improve as it would allow for a higher number density.

In the case of the screw dislocation however, temperature had a much smaller effect on the obstacle strength of the NCs. As the screw dislocation moved slower in general, the effect of temperature did not show up. Along with being independent of temperature, the depinning mechanism of a screw dislocation is completely controlled via the Orowan mechanism, as the screw dislocation bows around the NC until it is able to break free. When the NC breaks free, a dislocation loop is formed within the NC in the screw dislocations wake. The size of the dislocation loop is dependent on NC diameter, with the larger NCs having larger loops. The screw dislocation is able to retain its structure following the depinning with the NC. The results suggest that a medium sized NC is key for peak obstacle strengths, i.e. around 4 to 6 nm diameter.

Table 7.1. Table listing out the key parameters in calculating the α values for edge and screw dislocations for Y2O3 NCs.

Key Parameter	**Value**	
μ	70.7 GPa	
b	2.47 Å	
$\tau_{fr,300K,s} \mid L_{z,s}$	133 MPa	346.2 Å
$\tau_{fr,600K,s} \mid L_{z,s}$	151 MPa	
$\tau_{fr,300K,e} \mid L_{z,e}$	129 MPa	300.8 Å
$\tau_{fr,600K,e} \mid L_{z,e}$	148 MPa	

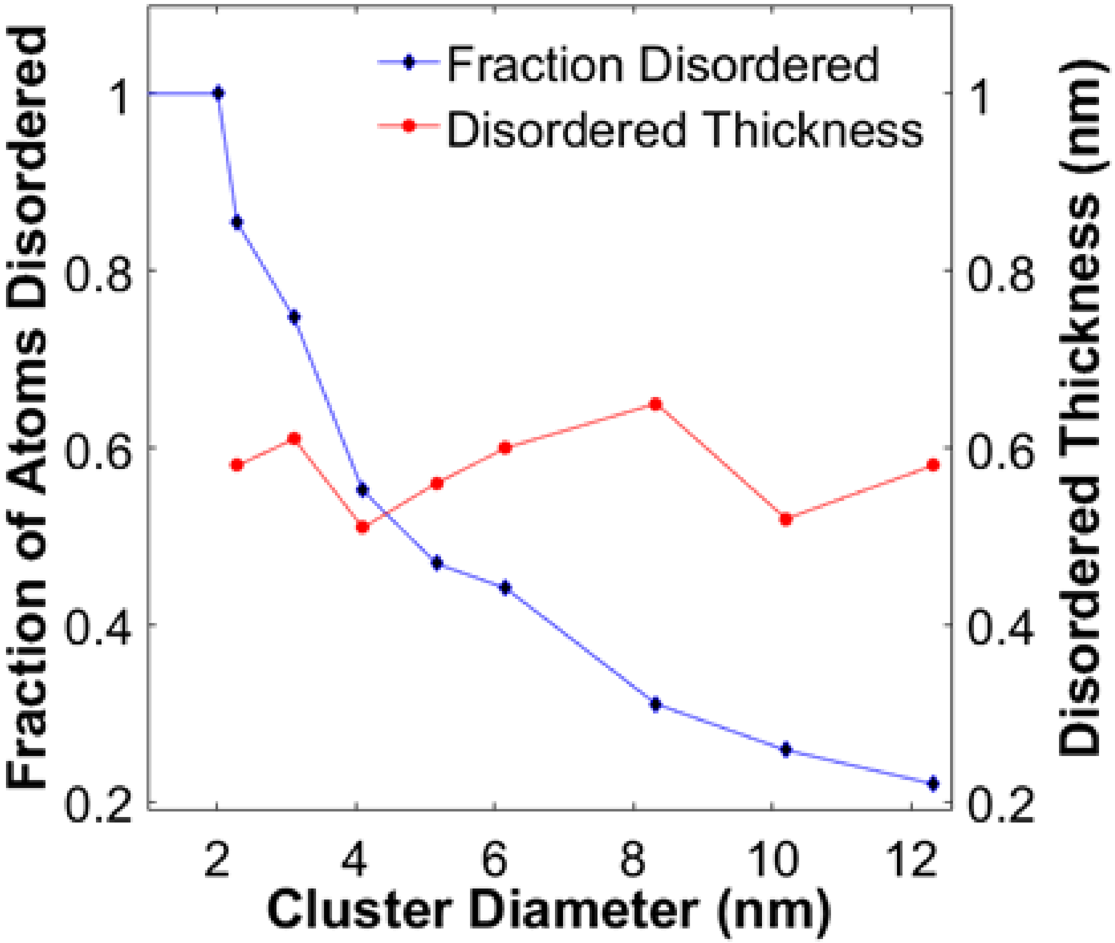

Figure 7.1. The disordered fraction of Y and O atoms in the shell regions as compared to those in the core regions along the left y-axis and the thickness of the disordered region along the right y-axis[117].

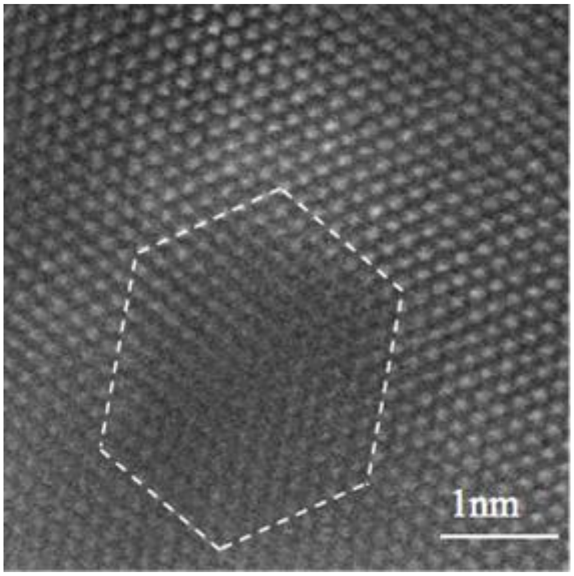

Figure 7.2. High-resolution HAADF image of a 2 nm Y2O3 cluster[117]

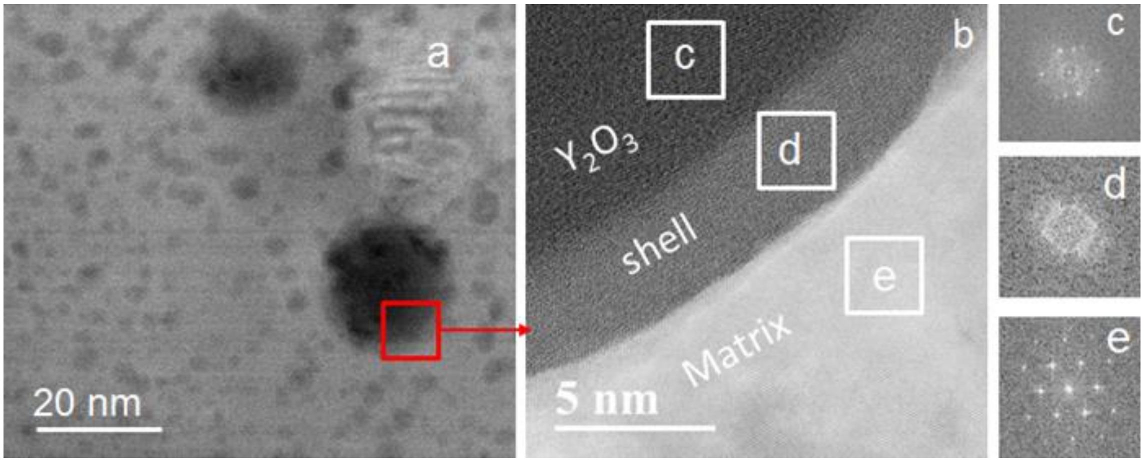

Figure 7.3. (a) HAADF image shows nano-sized oxides distributed in ODS matrix. (b) High-resolution HAADF image shows a disordered shell between matrix and a large yttria particle (c) FFT image from yttrium. (d) FFT image from disordered layer. (e) FFT image from ferritic matrix[117].

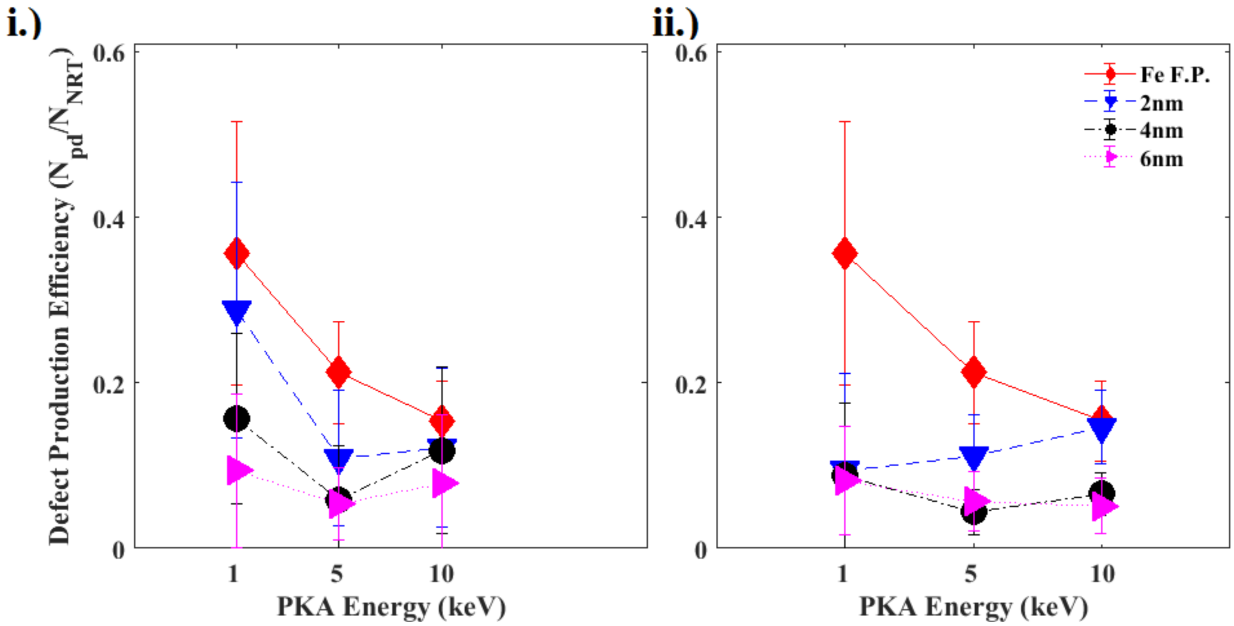

Figure 7.4. A ratio of the number of surviving defects to the predicted value using the NRT model for pure Fe versus the Fe matrix with the inclusion of a NC; i.) Fe vacancies and ii.) Fe interstitials[127].

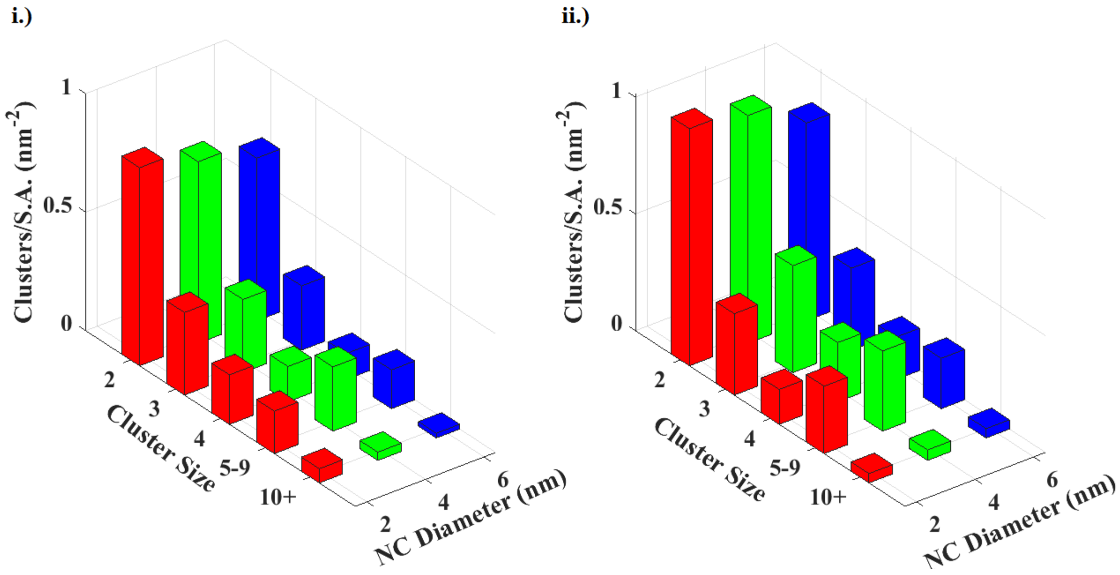

Figure 7.5.Distribution of the clusters surrounding the NC based on NC diameter for a 10 keV cascades; i.) vacancy clusters and ii.) interstitial clusters[127].

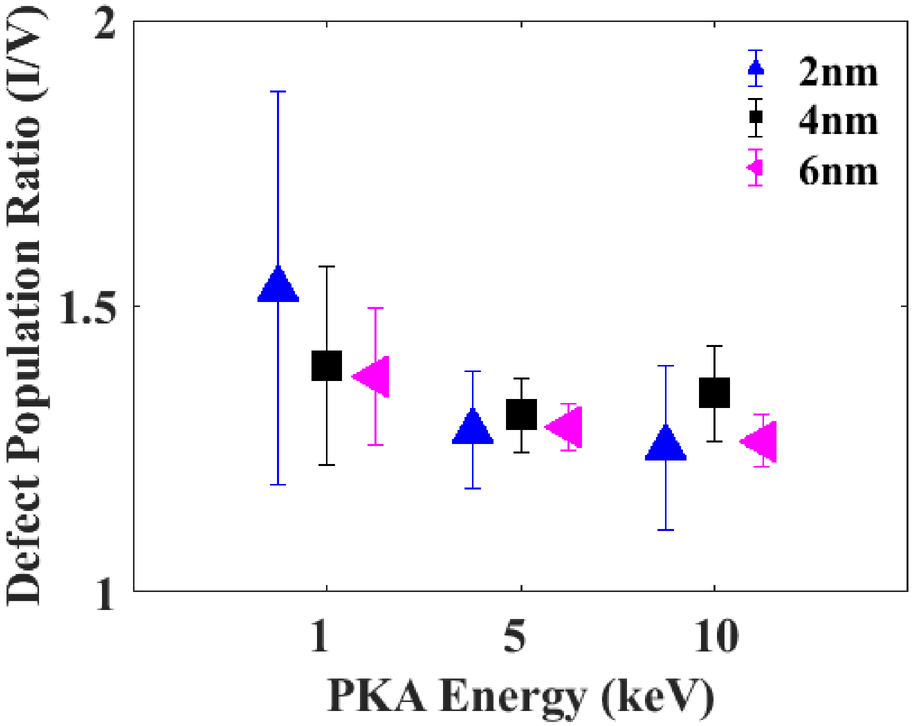

Figure 7.6. The ratio of the number of interstitials to vacancies surrounding the NC, as a function of diameters and PKA energies[127].

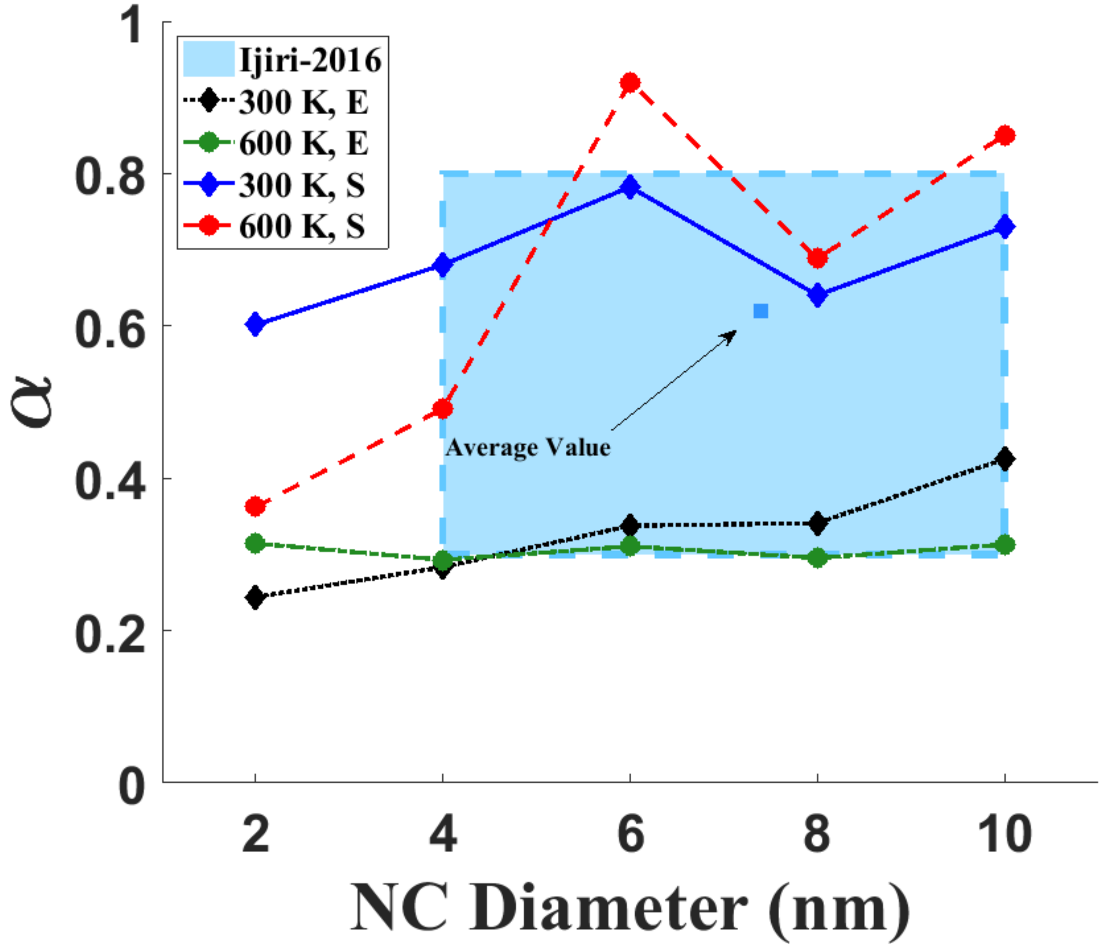

Figure 7.7. The α values calculated based on the depinning stress for the dislocations around the NC as a function of diameter, temperature, and dislocation type compared to an experimental study that calculated α for NCs using the TEM[134].

Chapter 8 - Conclusions

The work in this thesis can be broken into three major sections: the structure of Y_2O_3 nanoclusters (NCs), the primary damage state of a cascade near an Y_2O_3 NC, and dislocation interactions with Y_2O_3 NCs. Over the course of this dissertation MD has been used to further understand the implication that NCs have on the irradiation resistance and strength of oxide-dispersion strengthened (ODS) steels.

In summarizing the structure of the NCs investigated in this dissertation, computer simulations are corroborated with experimental results to study the structure of Y_2O_3 NCs in α-Fe. The results show that Y_2O_3 NCs are disordered when their size is below 2 nm, while the larger clusters form a core-shell structure, with a thickness of 0.5-0.7 nm that is independent of their size. The structure of the NC has a clear crossover from the completely disordered NCs to core-shell structures. Along with the structure of the NC, the inclusion of the NC also causes a slight disturbance in the Fe atoms directly surrounding the Y_2O_3 particles. The perturbed Fe atoms are also shown to further increase the irradiation strength of these particles, thus increasing irradiation resistance, in the cascade simulations. TEM images helped to validate the MD results showing a crossover from disordered NCs to core-shell structures, and the TEM results are qualitatively consistent with the MD simulations. Although the thickness of the disordered shell is smaller compared to the experimental data available, these results provide the atomistic-level understanding of Y_2O_3 NCs structures in α-Fe.

As stated above, the slight disorder in the iron atoms directly surrounding the NC are put to the test to understand these atoms and the NCs effect this structure has on the primary damage state of a cascade. Displacement cascades have been simulated to interact with NCs of various diameters, primary knock-on atoms (PKA) energies, and simulation temperature. New results help to further understand how cascade damage affects the evolution of defects in the Fe matrix surrounding NCs, the Fe-NC boundary, and the NC itself.

1) There are two major pathways for shockwave growth with the inclusion of a NC. At low energies of 1 and 5 keV PKAs, the shockwave occurs at the initial impact site with the NC. However, at higher energies the cascade energy is able to penetrate through the NC and cause two smaller shockwaves in the Fe matrix on opposite sides of the NC.

2) All the NCs experience amorphization via a displacement cascades, where the amorphization increases with PKA energy and the fraction of NC amorphization increases significantly with decreasing radii. Although there is an increase in amorphization of the NCs, the NC atoms remain together during the primary cascade damage.

3) With decreasing radii, there is a significant increase in the amount of disorder within the NCs, but the 2 nm NC has a higher fraction of disorder compared to the 4 and 6 nm NCs. In combining the disorder with Fe antisites within the NC, the MD results suggest that the tinier NCs are more likely to dissolve via ballistic dissolution.

4) In terms of the effect temperature has on the Fe-NC primary damage state, the results are minimal. As the amount of Frenkel pairs at the temperatures of 100 K, 300 K, and 600 K are all within a standard deviation of one another. The only difference occurs at 1 keV where the PKA is able to more easily transfer energy to the NC and thus a higher fraction of disorder is seen at 1 keV compared to the lower temperature cases.

Along with understanding the effect NCs have on the primary damage state of the cascade. MD is also used to investigate how Y_2O_3 NCs interact with dislocation, with the following parameters controlled: the type of dislocation that is interacting with the NC, the radius of the NC, ranging from 2 nm to 10 nm, and the temperature of the system, ranging from 300 K to 600 K.

In the case of the edge dislocation, when interacting with a NC, the depinning mechanisms are very similar for the two temperatures investigated in this study. As the edge dislocation becomes pinned along the dislocation, the depinning mechanism is a combination of Orowan and climbing. This climbing mechanism results in a change to the structure of the dislocation as the dislocations climb via cross-slip, as the edge dislocation now sits along two X-Z planes following depinning from the NC. The effect the climbing mechanism has on the critical resolved shear stress decreases with increasing temperature. The amount of climb shown within the edge dislocation is based on the size of the NC. Along with understanding the mechanism of depinning, the way α changes with both NC diameter and temperature is shown. As at lower temperatures, α increase with increasing NC diameter; however, at higher temperatures α is fairly independent of NC diameter. Suggesting in the case of edge dislocations at higher temperatures the structure itself affects α, independent of NC radii.

In the case of the screw dislocation, the depinning mechanism is independent of NC radii and temperature. The screw dislocation becomes pinned along the NC, at this point as the stress on the dislocation continues to grow. The depinning mechanism is completely controlled by the Orowan mechanism. However, while pinned a kink starts to form along the dislocation line, during the bowing process. Once a critical stress is met, the screw dislocation is able to break from the NC, leaving a dislocation loop attached to the NC in its wake. In comparison to the edge dislocation, the screw dislocation depinning with the NC has a significantly higher α. α is independent of temperature; NC diameter is the only factor for α for screw dislocations and Y_2O_3 NCs, and α tended to increase with increasing radii. In comparing the α of the screw dislocation to measured values, the simulations in this study are in good agreement and indicate that the key strengthening mechanism of ODS steel is in the NCs ability to hinder screw dislocations.

The key difference between the edge dislocation and the screw dislocation is the velocity of the dislocation at the applied stresses. As shown in table 7.1, the applied stresses within the Fe matrix are very similar for the edge and screw dislocation. However, although the applied stresses are the same the velocity of the two types of dislocations is very different, with the screw dislocation being an order of magnitude smaller than that of the edge dislocation. The higher velocity of the edge dislocation forces the NC to want to become free of the obstacle quicker, allowing the edge dislocation to use the climb mechanism to overcome the obstacle, whereas the screw dislocation is completely controlled via Orowan mechanism.

In comparing the results from both the primary damage state cascade simulations the dislocation interaction simulations, it is obvious that NCs play a key role in strengthening the base F/M steel matrix in two key ways: the first being in increasing the pure strength of the material and second in increasing the irradiation resistance of the material. As in the case of the primary damage state of the cascade, the key parameter is the ratio of the volume of the shockwave of the cascade to that of the NC. If the shockwave is able to overcome the NC volume then the amount of damage reduction greatly decreases in the Fe matrix. Whereas in terms of the NC atoms and the Fe-NC interface region, the number of point defects tended to be independent of NC radii. This suggests the key parameter is in the size of the NC such that the NC is larger than the shockwave. In the case of the dislocation interactions, for edge dislocations the NC diameter is independent of obstacle strength and the screw dislocation obstacle strength increases with increasing radii. However, for the screw dislocation there is a plateauing effect for larger NCs around 4 to 6 nm diameters. These results in this dissertation suggest that the optimal size for NC diameter is around 4 nm, as at this diameter the shockwave volume will be smaller in comparison to a 4 nm NC and the α for screw dislocations at this diameter are already very high.

Chapter 9 - Future Work

The future work section is broken into two major sections: the first section looks at the development of new interatomic potentials for a more modern look at the structure of nanoclusters (NCs) in α-Fe and the second section looks at key simulations that should be run to better understand the implication of NCs in oxide dispersion strengthened (ODS) steels. Modern ODS steels have been further improved by the inclusion of titanium during the ball milling process. The inclusion of titanium decreases the average size of NCs and changes the structure to consist of Y-Ti-O NCs. Current interatomic potentials have looked at Y-Ti-O[160,161] in its two structures and Fe-Y-O systems[114], no quaternary potentials have been developed for ODS steels. Molecular dynamics (MD) still has quite a few important places to improve the understanding of the evolution of radiation damage in ODS steels. A key area that needs to be further understood is in the interactions NCs have with dislocations.

9.1 New Potentials for Modelling ODS Steels: Fe-Y-Ti-O

A major limiting factor for ODS steel computational material research is the limited amount of potentials currently in existence. When ODS steels first became an option for next generation nuclear reactors in the late 90s, the powders for ball milling were still being optimized. During that time Y_2O_3 NCs were the NCs of choice for addition to the α-Fe matrix[10,67,119]. In modern ODS steels, the introduction of titanium powder to the ball milling process along with further fine tuning of the base Fe powder has led to ODS steel being more commonly known as nanostructured ferritic alloys (NFAs)[20,71,97,162]. Based on the Fe powder this consists of a ferritic or ferritic martensitic base alloy with the introduction of Y-Ti-O NCs.

In current NFAs, the inclusion of titanium in the powder has led to a decrease in the average radius of NCs[71,162–164]. These NCs have been shown to no longer have the cubic Y_2O_3 structure, but rather the structure of NCs now is either orthorhombic Y_2TiO_5 or pyrochlore $Y_2Ti_2O_7$[71,83,112,160]. As current ODS research is looking into steels with these NC structures. A major step in MD studies for ODS steels is the development of new potentials that are able to model these more complex Y-Ti-O structures in a α-Fe matrix. Quaternary interatomic potentials are very difficult to create. However, with time more and more quaternary potentials are being developed, along with breakthroughs using machine learning techniques in interatomic potential fitting[165–168]. A Fe-Y-Ti-O potential is required if computer simulations are to better understand the current generation of ODS steels.

9.2 Primary Radiation Damage State of the Various NC Structures

After the development of these potentials, energy comparisons of the three structure types: cubic Y_2O_3, orthorhombic Y_2TiO_5 and pyrochlore $Y_2Ti_2O_7$ need to be compared. Along with standard MD simulations of these structures, Monte Carlo simulations would be a nice touch to see which structures are more stable and in what conditions are certain structures favored over others. As the titanium oxides have been shown to be significantly more stable at smaller diameters, an investigation into the structure of pyrochlore and orthorhombic needs to be simulated. A look at various sizes of the three types of NCs and comparing the energy of the systems as a function of NC radius, may give key insight into why the NC structures appear at various diameter. Understanding the scenarios where each structure is more stable, is an important step in ODS steel research. MD and Monte Carlo would be very useful in this investigation.

After analyzing the structure and energy preferred stability of the three NC types a study looking at the lowest energy of the nearby Fe vacancy and interstitials of the three NC types would be very useful. In comparing the formation energy of defects surrounding the three NCs, by comparing the nearby formation energy of defects the general effect of adding NCs to the Fe matrix would be further understood. Studies have examined the effect different structures have on the formation energy of defects surrounding them[169–171]. By comparing the nearby Fe defect formation energy to the calculated formation energy of nearby Fe atoms to NCs, the sink strength of various defects could be compared to each other.

After understanding the affect NC structure has on the formation energy of point defects, a look at the affect NC structure has on the primary cascade simulations for the three NC types would be paramount. Most likely, the Y-Ti-O NCs would have a similar effect on the defect production within the Fe matrix; however, the interest is in how the NC structure affects the evolution of point defects during the primary damage state of a cascade. In this dissertation, MD is used to understand two key areas for NC interactions; the effects primary radiation has on the NCs and nearby Fe lattice and the effect NCs have on dislocations moving within the bcc matrix. One key area is absent that needs to be further understood; how the NC itself interacts and affects grain boundaries.

9.3 Grain Boundary NC interactions

NCs significantly improve both the strength of ODS steels by acting as an impediment to dislocation’s movement and irradiation resistance by adding another site for recombination. However, although that does effect the strength of these steels, overall NCs are just a tiny volume fraction in ODS steels, 4%, as currently small fractions of NCs improve the overall strength, but do not take away from the ductility of the steel[71,154,172]. Another key benefit of implementing NCs is that during the consolidation and the heat treatment is the creation of very small equiaxed grains [76,97,162]. Pinning of grain boundaries due to NCs is known to cause these small equiaxed grains to exist. These tiny grains are a major factor in the increased overall strength and improvements to the irradiation resistance of ODS steel[76].

NCs interaction with grain boundaries needs to be further understood; many studies have been done and there is now a systematic method to create grain boundaries of various misorientation angles in α-Fe[34,35,173,174]. The next step for ODS steels is combining this systematic approach to grain boundary creation with NCs. Simulations looking at the effects placing NCs nearby or within grain boundaries is an important simulation to understand how NCs help create tiny, equiaxed grain boundaries. The first part of this study would look at the preferred energy structure of NCs with grain boundaries and see if low angle or high angle grain boundaries are the preferred and most energy efficient structure. After learning the effects NCs have with grain boundaries. A study on the formation energy of defects surrounding the grain boundaries interacting with a NC, comparing these results to those of a grain boundary by itself would show further evidence on the impact of NCs in ODS steels.

After understanding how NCs affect the structure and formation energy of the surrounding lattice sites, a new area of research is cascade simulations of NCs pinned at grain boundaries. A low PKA energy could be very interesting to see the effects and migration of defects to and around the combined grain boundary – NC site. As many studies have shown that grain boundaries within the primary radiation damage have a major bias towards interstitials and in this dissertation the primary damage state of cascades at NCs has a shown a similar bias towards interstitials. A combined look at the effects of grain boundary – NC is the next step, and to see how interstitials migrate in that scenario. At this point, MD would have given significant information on the effects of NCs on the surrounding α-Fe matrix. From there, higher order simulations would be the required next step.

Along with understanding the affect NCs have on grain boundaries, another key area that needs to be understood is how grain boundaries affect the mobility of edge and screw dislocations. In order to properly model an ODS steel in dislocation dynamics (DD), along with NCs, the inclusion of different defect structures is paramount in properly modelling this material and understanding which structure in ODS steels has a greater effect on the strength of the material, the tiny NCs or the creation of tiny grain boundaries

References

[1] World Nucl. Assoc. (2019).

[2] G.H. Marcus, Prog. Nucl. Energy (2000).

[3] P.H. Rebut, Fusion Eng. Des. (1995).

[4] G.S. Was, (2015).

[5] S.J. Zinkle, 058101 (2009).

[6] S.J. Zinkle, L.L. Snead, Annu. Rev. Mater. Res. 44 (2014) 241–267.

[7] F.A. Garner, M.B. Toloczko, B.H. Sencer, J. Nucl. Mater. (2000).

[8] A.A.F. Tavassoli, E. Diegele, R. Lindau, N. Luzginova, H. Tanigawa, J. Nucl. Mater. 455 (2014) 269–276.

[9] H. Tanigawa, K. Shiba, A. Möslang, R.E. Stoller, R. Lindau, M.A. Sokolov, G.R. Odette, R.J. Kurtz, S. Jitsukawa, J. Nucl. Mater. 417 (2011) 9–15.

[10] H. Tanigawa, E. Gaganidze, T. Hirose, M. Ando, S.J. Zinkle, R. Lindau, E. Diegele, Nucl. Fusion 57 (2017).

[11] G.R. Odette, M.J. Alinger, B.D. Wirth, Annu. Rev. Mater. Res. 38 (2008) 471–503.

[12] C. Hin, B.D. Wirth, Mater. Sci. Eng. A 528 (2011) 2056–2061.

[13] J.P. Wharry, M.J. Swenson, K.H. Yano, J. Nucl. Mater. 486 (2017) 11–20.

[14] D.J. Bacon, F. Gao, Y.N. Osetsky, J. Nucl. Mater. 276 (2000) 1–12.

[15] Q.U.A. Sahi, Y.S. Kim, Mater. Res. Express 5 (2018) 1–12.

[16] F. Gao, D.J. Bacon, P.E.J. Flewitt, T.A. Lewis, J. Nucl. Mater. 249 (1997) 77–86.

[17] S. Plimpton, 117 (1995) 1–42.

[18] A. Stukowski, Model. Simul. Mater. Sci. Eng. 18 (2010) 1–7.

[19] A. Arsenlis, W. Cai, M. Tang, M. Rhee, T. Oppelstrup, G. Hommes, T.G. Pierce, V. V Bulatov, Model. Simul. Mater. Sci. Eng. (2007).

[20] S.J. Zinkle, L.L. Snead, Annu. Rev. Mater. Res. 44 (2014) 241–267.

[21] R.E. Stoller, G.R. Odette, B.D. Wirth, J. Nucl. Mater. 251 (1997) 49–60.

[22] S. Edition, Fundamentals of Radiation Materials Science, n.d.

[23] D.J. Bacon, A.F. Calder, F. Gao, J. Nucl. Mater. 251 (1997) 1–12.

[24] F. Gao, D.J. Bacon, P.E.J. Flewitt, T.A. Lewis, J. Nucl. Mater. 249 (1997) 77–86.

[25] D.J. Bacon, a. F. Calder, F. Gao, J. Nucl. Mater. 251 (1997) 1–12.

[26] M.I. Mendelev, S. Han, D.J. Srolovitz, G.J. Ackland, D.Y. Sun, M. Asta, Philos. Mag. 83 (2003) 3977–3994.

[27] M. Marinica, F. Willaime, J. Crocombette, 025501 (2012) 1–5.

[28] P. Jung, 117 (1983) 70–77.

[29] R.S. Averback, R. Benedek, K.L. Merkle, Phys. Rev. B - Condens. Matter Mater. Phys. 18 (1978) 4156–4171.

[30] A. Hosseini, M.N. Nasrabadi, A. Esfandiarpour, S.A.H. Feghhi, A. Arjhangmehr, Nucl. Instruments Methods Phys. Res. Sect. B Beam Interact. with Mater. Atoms 439 (2016) 43–50.

[31] K. Nordlund, S.J. Zinkle, A.E. Sand, F. Granberg, R.S. Averback, R.E. Stoller, T. Suzudo, L. Malerba, F. Banhart, W.J. Weber, F. Willaime, S.L. Dudarev, D. Simeone, J. Nucl. Mater. (2018).

[32] P.E. Kapustin, M.Y. Tikhonchev, R.T. Sibatov, V. V. Svetukhin, Results Phys. 12 (2019) 175–177.

[33] F. Gao, D.J. Bacon, P.E.J. Flewitt, T.A. Lewis, J. Nucl. Mater. 249 (1997) 77–86.

[34] M.A. Tschopp, M.F. Horstemeyer, F. Gao, X. Sun, M. Khaleel, Scr. Mater. 64 (2011) 908–911.

[35] A. Esfandiarpour, S.A.H. Feghhi, A.A. Shokri, Nucl. Instruments Methods Phys. Res. Sect. B Beam Interact. with Mater. Atoms 362 (2015) 1–8.

[36] A. Kedharnath, R. Kapoor, A. Sarkar, J. Nucl. Mater. (2019).

[37] J.E. Ludy, T.J. Rupert, Scr. Mater. 110 (2016) 37–40.

[38] A. Hosseini, M.N. Nasrabadi, A. Esfandiarpour, Nucl. Instruments Methods Phys. Res. Sect. B Beam Interact. with Mater. Atoms 439 (2019) 43–50.

[39] Y.N. Osetsky, D.J. Bacon, A. Serra, B.N. Singh, S.I. Golubov, 276 (2000).

[40] P. Franciosi, 31 (1983) 1331–1342.

[41] W.A. Spitzig, A.S. Keh, 18 (1970) 611–622.

[42] J.P. Chang, V. V. Bulatov, S. Yip, J. Comput. Mater. Des. 6 (1999) 165–173.

[43] J. Chang, W. Cai, V. V. Bulatov, S. Yip, Comput. Mater. Sci. 23 (2002) 111–115.

[44] Y.N. Osetsky, D.J. Bacon, Model. Simul. Mater. Sci. Eng. 11 (2003) 427–446.

[45] C. Li-Qun, W. Chong-Yu, Y. Tao, Chinese Phys. B 17 (2008) 662–668.

[46] T.D. Swinburne, S.L. Dudarev, S.P. Fitzgerald, M.R. Gilbert, A.P. Sutton, Phys. Rev. B - Condens. Matter Mater. Phys. 87 (2013) 1–15.

[47] J. Chaussidon, M. Fivel, D. Rodney, Acta Mater. 54 (2006) 3407–3416.

[48] M. Itakura, H. Kaburaki, M. Yamaguchi, Acta Mater. 60 (2012) 3698–3710.

[49] A. Lehtinen, F. Granberg, L. Laurson, K. Nordlund, M.J. Alava, Phys. Rev. E 93 (2016) 1–9.

[50] S.M. Hafez Haghighat, M.C. Fivel, J. Fikar, R. Schaeublin, J. Nucl. Mater. 386–388 (2009) 102–105.

[51] B. Zhu, M. Huang, Z. Li, Nucl. Instruments Methods Phys. Res. Sect. B Beam Interact. with Mater. Atoms 397 (2017) 51–61.

[52] A. Dutta, M. Bhattacharya, N. Gayathri, G.C. Das, P. Barat, Acta Mater. 60 (2012) 3789–3798.

[53] K. Asari, O.S. Hetland, S. Fujita, M. Itakura, T. Okita, J. Nucl. Mater. 442 (2013)

360–364.

[54] R.L. Klueh, D.R. Harries, High-Chromium Ferritic and Martensitic Steels for Nuclear Applications, 2001.

[55] R.L. Klueh, J.P. Shingledecker, R.W. Swindeman, D.T. Hoelzer, J. Nucl. Mater. (2005).

[56] H. Zhang, Y. Huang, H. Ning, C.A. Williams, A.J. London, K. Dawson, Z. Hong, M.J. Gorley, C.R.M. Grovenor, G.J. Tatlock, S.G. Roberts, M.J. Reece, H. Yan, P.S. Grant, J. Nucl. Mater. (2015).

[57] R. Lindau, A. Möslang, M. Rieth, M. Klimiankou, E. Materna-Morris, A. Alamo, A.-A.F. Tavassoli, C. Cayron, A.-M. Lancha, P. Fernandez, N. Baluc, R. Schäublin, E. Diegele, G. Filacchioni, J.W. Rensman, B.V.D. Schaaf, E. Lucon, W. Dietz, (2005).

[58] D.T. Hoelzer, J. Bentley, M.A. Sokolov, M.K. Miller, G.R. Odette, M.J. Alinger, J. Nucl. Mater. (2007).

[59] R.S. Nelson, J.A. Hudson, D.J. Mazey, J. Nucl. Mater. (1972).

[60] M.L. Lescoat, J. Ribis, Y. Chen, E.A. Marquis, E. Bordas, P. Trocellier, Y. Serruys, A. Gentils, O. Kaïtasov, Y. De Carlan, A. Legris, Acta Mater. (2014).

[61] G. Martin, Phys. Rev. B (1984).

[62] W.D. Callister, J.G. David Rethwisch, MATERIALS SCIENCE and ENGINEERING, n.d.

[63] J. Li, C. Guo, Y. Ma, Z. Wang, J. Wang, Acta Mater. (2015).

[64] R.D. Vengrenovich, A. V. Moskalyuk, S. V. Yarema, Phys. Solid State (2007).

[65] S.G. Kim, Acta Mater. (2007).

[66] V.M. Burlakov, L. Kantorovich, J. Chem. Phys. (2011).

[67] S. V. Rogozhkin, A.A. Aleev, A.G. Zaluzhnyi, A.A. Nikitin, N.A. Iskandarov, P. Vladimirov, R. Lindau, A. Möslang, J. Nucl. Mater. 409 (2011) 94–99.

[68] S. V. Rogozhkin, A.A. Aleev, A.G. Zaluzhnyi, R.P. Kuibida, T. V. Kulevoi, A.A. Nikitin, N.N. Orlov, B.B. Chalykh, V.B. Shishmarev, Phys. Met. Metallogr. (2012).

[69] D. Menut, J.-L. Béchade, S. Cammelli, S. Schlutig, B. Sitaud, P.L. Solari, J. Mater. Res. (2015).

[70] I. Monnet, T. Van Den Berghe, P. Dubuisson, J. Nucl. Mater. (2012).

[71] J.P. Wharry, M.J. Swenson, K.H. Yano, J. Nucl. Mater. 486 (2017) 11–20.

[72] J. He, F. Wan, K. Sridharan, T.R. Allen, A. Certain, V. Shutthanandan, Y.Q. Wu, J. Nucl. Mater. (2014).

[73] J. He, F. Wan, K. Sridharan, T.R. Allen, A. Certain, Y.Q. Wu, J. Nucl. Mater. (2014).

[74] S. V. Rogozhkin, A.A. Aleev, A.G. Zaluzhnyi, N.A. Iskanderov, A.A. Nikitin, P. Vladimirov, R. Lindau, A. Möslang, Phys. Met. Metallogr. (2012).

[75] I. Monnet, P. Dubuisson, Y. Serruys, M.O. Ruault, O. Kaïtasov, B. Jouffrey, J.

Nucl. Mater. 335 (2004) 311–321.

[76] N. Akasaka, S. Yamashita, T. Yoshitake, S. Ukai, A. Kimura, in:, J. Nucl. Mater., 2004, pp. 1053–1056.

[77] P.D. Edmondson, A. London, A. Xu, D.E.J. Armstrong, S.G. Roberts, J. Nucl. Mater. (2015).

[78] M.K. Miller, D.T. Hoelzer, J. Nucl. Mater. (2011).

[79] R. Lindau, J. Hoffmann, A. Möslang, P. Vladimirov, M. Klimenkov, M. Heilmaier, J. Wagner, S. Seils, T. Kulevoy, B. Chalykh, Nucl. Mater. Energy (2016).

[80] S. Yamashita, K. Oka, S. Ohnuki, N. Akasaka, S. Ukai, J. Nucl. Mater. (2002).

[81] S. Pasebani, I. Charit, J. Burns, S. Alsagabi, D.P. Butt, J.I. Cole, L.M. Price, L. Shao, J. Nucl. Mater. (2015).

[82] J. Ribis, E. Bordas, P. Trocellier, Y. Serruys, Y. De Carlan, A. Legris, Nucl. Instruments Methods Phys. Res. Sect. B Beam Interact. with Mater. Atoms (2015).

[83] J. Ribis, S. Lozano-Perez, J. Nucl. Mater. (2014).

[84] J. Ribis, J. Nucl. Mater. (2013).

[85] S. Yamashita, 370 (2007) 202–207.

[86] T. Chen, J.G. Gigax, L. Price, D. Chen, S. Ukai, E. Aydogan, S.A. Maloy, F.A. Garner, L. Shao, Acta Mater. 116 (2016) 29–42.

[87] M.L. Lescoat, J. Ribis, A. Gentils, O. Kaïtasov, Y. De Carlan, A. Legris, J. Nucl. Mater. 428 (2012) 176–182.

[88] Y. Zhanbing, H. Benfu, H. Kinoshita, H. Takahashi, S. Watanabe, J. Nucl. Mater. 398 (2010) 81–86.

[89] M. Lescoat, I. Monnet, J. Ribis, P. Dubuisson, Y. De Carlan, J. Costantini, J. Malaplate, J. Nucl. Mater. 417 (2011) 266–269.

[90] A. Ramar, N. Baluc, R. Schäublin, J. Nucl. Mater. (2007).

[91] I. Monnet, C. Grygiel, M.L. Lescoat, J. Ribis, J. Nucl. Mater. (2012).

[92] F. Li, H. Abe, T. Ishizaki, Y. Li, T. Nagasaka, T. Muroga, T. Nagase, H. Yasuda, J. Nucl. Mater. 455 (2014) 724–727.

[93] R.E. Stoller, G.R. Odette, B.D. Wirth, J. Nucl. Mater. 251 (1997) 49–60.

[94] S. Queyreau, J. Marian, M.R. Gilbert, B.D. Wirth, Phys. Rev. B - Condens. Matter Mater. Phys. 84 (2011) 1–7.

[95] B.H. Sencer, F.A. Garner, D.S. Gelles, G.M. Bond, S.A. Maloy, 311 (2002) 266–271.

[96] K. Mo, Z. Zhou, Y. Miao, D. Yun, H. Tung, G. Zhang, W. Chen, J. Almer, J.F. Stubbins, J. Nucl. Mater. 455 (2014) 376–381.

[97] G.R. Odette, Jom 66 (2014) 2427–2441.

[98] Y. Wu, E.M. Haney, N.J. Cunningham, G.R. Odette, 60 (2012) 3456–3468.

[99] S. Yamashita, 333 (2004) 377–381.

[100] R. Xie, Z. Lu, C. Lu, C. Liu, J. Nucl. Mater. 455 (2014) 554–560.

[101] C. Lu, Z. Lu, R. Xie, C. Liu, L. Wang, J. Nucl. Mater. 455 (2014) 366–370.

[102] M. Klimiankou, R. Lindau, 249 (2003) 381–387.

[103] M. Klimenkov, R. Lindau, A. Möslang, J. Nucl. Mater. 386–388 (2009) 553–556.

[104] M.K. Miller, E.A. Kenik, K.F. Russell, L. Heatherly, D.T. Hoelzer, P.J. Maziasz, Mater. Sci. Eng. A (2003).

[105] a. J. London, S. Santra, S. Amirthapandian, B.K. Panigrahi, R.M. Sarguna, S. Balaji, R. Vijay, C.S. Sundar, S. Lozano-Perez, C.R.M. Grovenor, Acta Mater. 97 (2015) 223–233.

[106] M. Klimiankou, R. Lindau, 333 (2004) 347–351.

[107] E.A. Marquis, 93 (2008) 91–94.

[108] M.K. Miller, D.T. Hoelzer, E.A. Kenik, K.F. Russell, in:, J. Nucl. Mater., 2004.

[109] L. Barnard, G.R. Odette, I. Szlufarska, D. Morgan, Acta Mater. 60 (2012) 935–947.

[110] L. Barnard, N. Cunningham, G.R. Odette, I. Szlufarska, D. Morgan, Acta Mater. 91 (2015) 340–354.

[111] G.D. Samolyuk, Y.N. Osetsky, J. Phys. Condens. Matter (2015).

[112] M.J. Alinger, B.D. Wirth, H.J. Lee, G.R. Odette, J. Nucl. Mater. (2007).

[113] W. Humphrey, A. Dalke, K. Schulten, 7855 (1996) 33–38.

[114] K.D. Hammond, H.-J. Lee Voigt, L.A. Marus, N. Juslin, B.D. Wirth, J. Phys. Condens. Matter 25 (2013) 55402–13.

[115] F. Hanic, M. Hartmanová, G.G. Knab, A.A. Urusovskaya, K.S. Bagdasarov, Acta Crystallogr. Sect. B Struct. Sci. (1984).

[116] R.J. Gaboriaud, F. Paumier, B. Lacroix, Thin Solid Films (2016).

[117] M.P. Higgins, C.Y. Lu, Z. Lu, L. Shao, L.M. Wang, F. Gao, Appl. Phys. Lett. 109 (2016) 1–4.

[118] S. Ukai, M. Fujiwara, 311 (2002) 749–757.

[119] E.A. Marquis, Appl. Phys. Lett. 93 (2008) 1–4.

[120] S. V. Rogozhkin, A.A. Aleev, A.G. Zaluzhnyi, A.A. Nikitin, N.A. Iskandarov, P. Vladimirov, R. Lindau, A. Möslang, J. Nucl. Mater. 409 (2011) 94–99.

[121] Y. Zhanbing, H. Benfu, H. Kinoshita, H. Takahashi, S. Watanabe, J. Nucl. Mater. 398 (2010) 81–86.

[122] D. Murali, B.K. Panigrahi, M.C. Valsakumar, S. Chandra, C.S. Sundar, B. Raj, J. Nucl. Mater. 403 (2010) 113–116.

[123] C. Hin, B.D. Wirth, J. Nucl. Mater. 402 (2010) 30–37.

[124] T. Lazauskas, S.D. Kenny, R. Smith, G. Nagra, M. Dholakia, M.C. Valsakumar, J. Nucl. Mater. 437 (2013) 317–325.

[125] D. Murali, B.K. Panigrahi, M.C. Valsakumar, S. Chandra, C.S. Sundar, B. Raj, J. Nucl. Mater. 403 (2010) 113–116.

[126] K. Nordlund, R.S. Averback, B. Gao, 56 (1997) 2421–2431.

[127] M.P. Higgins, Q. Peng, L. Shao, F. Gao, J. Appl. Phys. 126 (2019) 084302.

[128] U. Shigeharu, M. Shunji, F. Masayuki, O. Takanari, K. Toshimi, J. Nucl. Sci. Technol. 39 (2002) 778–788.

[129] M. Dholakia, S. Chandra, S.M. Jaya, J. Alloys Compd. 739 (2018) 1037–1047.

[130] A. Lehtinen, L. Laurson, F. Granberg, K. Nordlund, M.J. Alava, Sci. Rep. 8 (2018).

[131] S. Kodambaka, S. V. Khare, W. Śwlęch, K. Ohmori, I. Petrov, J.E. Greene, Nature 429 (2004) 49–52.

[132] K. Yashiro, a Yamaguchi, M. Tanaka, Mater. Trans. … 53 (2012) 401–406.

[133] D.J. Srolovitz, R.A. Petkovic-luton, M.J. Litton, Philos. Mag. A Phys. Condens. Matter, Struct. Defects Mech. Prop. 48 (1983) 795–809.

[134] Y. Ijiri, N. Oono, S. Ukai, S. Ohtsuka, T. Kaito, Y. Matsukawa, Nucl. Mater. Energy 9 (2016) 378–382.

[135] D. Terentyev, G. Bonny, C. Domain, G. Monnet, L. Malerba, J. Nucl. Mater. 442 (2013) 470–485.

[136] S. Kondo, T. Mitsuma, N. Shibata, Y. Ikuhara, Sci. Adv. 2 (2016).

[137] Y.N. Osetsky, A.G. Mikhin, A. Serra, J. Nucl. Mater. 212–215 (1994) 236–240.

[138] Y.N. Osetsky, D.J. Bacon, V. Mohles, in:, Philos. Mag., 2003, pp. 3623–3641.

[139] D. Terentyev, P. Grammatikopoulos, D.J. Bacon, Y.N. Osetsky, Acta Mater. 56 (2008) 5034–5046.

[140] A. Takahashi, N.M. Ghoniem, J. Mech. Phys. Solids 56 (2008) 1534–1553.

[141] I. Ringdalen, S. Wenner, J. Friis, J. Marian, MRS Commun. 7 (2017) 626–633.

[142] M.M. Azeem, Q. Wang, Z. Li, Y. Zhang, Nucl. Eng. Technol. (2019).

[143] F. Granberg, D. Terentyev, K. Nordlund, J. Nucl. Mater. 460 (2015) 23–29.

[144] T. Hatano, H. Matsui, Phys. Rev. B - Condens. Matter Mater. Phys. 72 (2005).

[145] D. Terentyev, D.J. Bacon, Y.N. Osetsky, J. Phys. Condens. Matter 20 (2008).

[146] X. Zhang, G. Lu, J. Phys. Condens. Matter 25 (2013).

[147] X. Zhang, H. Deng, S. Xiao, X. Li, W. Hu, Comput. Mater. Sci. 68 (2013) 132–137.

[148] X.H. Long, D. Wang, W. Setyawan, P. Liu, N. Gao, R.J. Kurtz, Z.G. Wang, X.L. Wang, Phys. Status Solidi Appl. Mater. Sci. 215 (2018).

[149] P.M. Anderson, J.P. Hirth, J. Lothe Frontmatter, Theory of Dislocations, 2017.

[150] M.C. Brandes, L. Kovarik, M.K. Miller, M.J. Mills, (2012) 3913–3923.

[151] M.J. Norgett, M.T. Robinson, I.M. Torrens, Nucl. Eng. Des. 33 (1975) 50–54.

[152] B.N. Sources, D.C. Irradiation, 12 (2019) 1–20.

[153] J.E. Ludy, T.J. Rupert, Scr. Mater. 110 (2016) 37–40.

[154] M.J. Swenson, J.P. Wharry, J. Nucl. Mater. 496 (2017) 24–40.

[155] D. Häussler, M. Bartsch, U. Messerschmidt, B. Reppich, Acta Mater. 49 (2001) 3647–3657.

[156] E. Arzt, D.S. Wilkinson, Acta Metall. 34 (1986) 1893–1898.

[157] J. Malaplate, F. Mompiou, J.L. Béchade, T. Van Den Berghe, M. Ratti, in:, J. Nucl. Mater., 2011, pp. 205–208.

[158] D. Häussler, B. Reppich, M. Bartsch, U. Messerschmidt, Mater. Sci. Eng. A 309–310 (2001) 500–504.

[159] A. Seeger, J. Diehl, S. Mader, H. Rebstock, B.A. Sexiqeb, H. Rebetook, (2010).

[160] Y. Jin, Y. Jiang, L. Yang, G. Lan, R.G. Odette, T. Yamamoto, J. Shang, Y. Dang, J. Appl. Phys. (2014).

[161] N.B. Camilli, (2013).

[162] S.J. Zinkle, A. Möslang, T. Muroga, J.L. Boutard, D.T. Hoelzer, A. Kimura, R. Lindau, G.R. Odette, M. Rieth, L. Tan, H. Tanigawa, Nucl. Fusion 57 (2017) 17.

[163] S. Ukai, M. Fujiwara, J. Nucl. Mater. 307–311 (2002) 749–757.

[164] N. Akasaka, S. Yamashita, T. Yoshitake, S. Ukai, A. Kimura, in:, J. Nucl. Mater., 2004.

[165] H. Chan, B. Narayanan, M.J. Cherukara, F.G. Sen, K. Sasikumar, S.K. Gray,

M.K.Y. Chan, S.K.R.S. Sankaranarayanan, J. Phys. Chem. C (2019).

[166] J. Behler, J. Chem. Phys. (2016).

[167] A.P. Bartók, J. Kermode, N. Bernstein, G. Csányi, Phys. Rev. X (2018).

[168] P. Rowe, G. Csányi, D. Alfè, A. Michaelides, Phys. Rev. B (2018).

[169] K.K. Abgaryan, O. V. Volodina, S.I. Uvarov, Mod. Electron. Mater. 1 (2015) 82–87.

[170] K.O.E. Henriksson, AIP Adv. (2016).

[171] C.M. Koller, N. Koutná, J. Ramm, S. Kolozsvári, J. Paulitsch, D. Holec, P.H. Mayrhofer, AIP Adv. (2016).

[172] M.J. Swenson, C.K. Dolph, J.P. Wharry, J. Nucl. Mater. (2016).

[173] S.J. Plimpton, MOLECULAR DYNAMICS SIMULATIONS OF GRAIN-BOUNDARY DIFFUSION FOR VARYING TILT ANGLE GEOMETRIES, n.d.

[174] S. Ratanaphan, D.L. Olmsted, V. V Bulatov, E.A. Holm, A.D. Rollett, G.S. Rohrer, ACTA Mater. 88 (2015) 346–354.